University of Siena

Department of Molecular and Developmental Medicine

Ph.D. in
Molecular Medicine

CYCLE XXXV
COORDINATOR Prof. Vincenzo Sorrentino

Comprehensive optical and data management framework for sympathetic network investigation in large-scale infarct border-zone of pig hearts

Academic Discipline (SSD) BIO/09

Doctoral candidate

Camilla Olianti

Camilla Olianti

Signed on 03/05/2023

Supervisor

Dr. Leonardo Sacconi

Tutor

Prof. Elisabetta Cerbai

Academic Year 2021/2022

In memory of Matthew Amoni

Before presenting the project of this PhD thesis, I want to dedicate a thought to Matthew, without whom this project would not have been possible.

Matthew Amoni was an incredibly talented MD-PhD candidate in Prof. Karin Sipido's group at the University of Leuven, Belgium. He obtained his medical degree, concurrently with a masters' degree, from the University of Cape Town (South Africa) at the age of 25, before moving to Belgium to start a research project focused on the mechanisms of post-infarction arrhythmogenesis.

It was thanks to his discoveries that a very stimulating collaboration started with Prof. Sipido's group and that the project, which is the aim of this thesis, was conceived.

Tragically, Matthew passed away at the beginning of October 2022 at the age of 32, leaving all of us profoundly shocked.

In the project that I am going to present, he was the one who took care of all the *in-vivo* studies in pigs. Due to his remarkable expertise, he has always been an incredible resource in figuring out solutions to the problems I had to face over the years and he has always been extremely supportive to me. He was the kind of person that always has a smile on his face.

For sure Matthew would deserve a much longer section of credits for his work, but I will conclude by acknowledging him for having been a crucial landmark during the course of my PhD.

Contents

1. SUMMARY

Myocardial infarction (MI) affects millions of people every year and those who survive have an increased risk of developing arrhythmias and to experience sudden cardiac death. Indeed, prolonged ischemia leads to cell death and can result in the adverse remodeling of the left ventricular tissue, mainly consisting in the formation of large, non-conductive fibrotic patches that provide a convenient substrate for the development of arrhythmias. However, recently the cardiac sympathetic nervous system (SNS) has also been observed to remodel after an episode of MI, thus potentially taking part in triggering arrhythmias. Among the arrhythmogenic events associated with MI, premature ventricular complexes (PVCs) have shown to be the most common ones and, moreover, to correlate with sympathetic stimulation in pigs. While a lot of evidence has been provided in regards to the fibrotic response that follows a MI, the nature and the extent of the SNS remodeling are still poorly comprehended, mainly due to methodological limitations that, over the years, have restrained previous research to bidimensional investigations or to the study of small animal models. Since the sympathetic network exerts significant effects on the electrophysiological properties of the heart, understanding the structural outcomes of this remodeling could offer important insights to comprehend the pivotal factors involved in determining whether or not arrhythmias would arise after an infarct.

The aim of this PhD project was to develop a comprehensive methodological framework to three-dimensionally reconstruct the infarct border-zone (BZ) in large-scale pig heart slices at high resolution. In this proof of concept conducted on a small population, we wanted to assess whether the differences between arrhythmia-initiating (PVC) and not initiating sites (NO-PVC) detected *in-vivo* could rely on the structural features that the tissue develops during the remodeling process.

To this goal, at first we had to solve the problem of light scattering in large-size biological samples, which has been one of the major limitations that have restrained previous studies. We exploited mouse hearts to test and optimize three of the most successful optical clearing methodologies (uDISCO, CLARITY and SHIELD) aimed at reducing the refractive index mismatch across the sample. We investigated their performances in terms of preservation of the tissue features and compatibility with a homogenous staining of the whole organ. Among the three tested protocols, the CLARITY technique showed to be the most effective one.

Thus, we applied the developed clearing and staining approach to the selected pig heart slices, with a further implementation to avoid out-of-plain distortions of the samples, and we obtained 3D reconstructions of the entire volume of the samples by two-photon fluorescence microscopy. The high resolution of the images allowed us to exploit a machine-learning based software tool developed to map and analyze the detected structural features. We analyzed cellular disarray along with density and alignment coherency of the sympathetic innervation, in both PVC and NO-PVC sites, comparing them to remote sites isolated from the healthy distal myocardium. We found a solid consistency between the remote sites in terms of both cellular organization and neuronal density and coherency, thus validating our high-fidelity analysis approach. Moreover, we found a highly significant reduction ($68 \pm 15\%$) of innervation in the scar regions with respect to the myocardium in all the BZ samples, suggesting a strong denervation process that occurs in the fibrotic patches during the remodeling. An overall reduction of neurofilament alignment was also observed in the BZ samples with respect to the distal healthy myocardium which could benefit from investigating a larger cohort of samples. However, in this preliminary study no differences were found between arrhythmia-initiating and not-initiating sites.

We believe that, due to the high relevance of 3D information achieved on a human-mimicking animal model, we have provided a clearer and more reliable view of the cardiac SNS remodeling that occurs after a MI.

Moreover, the methodological pipeline that we developed has shown the capability of providing accurate three–dimensional reconstructions of massive samples isolated from large, human-resembling animal models, thus paving the way to the possibility of expanding the analysis to investigate different structural features that may be involved in the rise of arrhythmias.

2. INTRODUCTION

2.1 Cardiac anatomy

2.1.1 Cardiac macroscopic anatomy

The heart is a muscle that ensures blood flow in the systemic circulation through regular contractions. It is a muscular-membranous organ protected by the intercostal cartilages and situated in the anterior mediastinum of the thoracic cavity, between the two lungs and above the diaphragm, which divides it from the abdominal viscera.

The heart is shaped like a flattened truncated cone (*Figure 1)*. The base of the organ corresponds to the atrial component and it faces upwards, while the apex faces downward and corresponds to the ventricular component. In the heart, we can also distinguish an anterior face, the sternocostal face, and a posterior face, the diaphragmatic face.

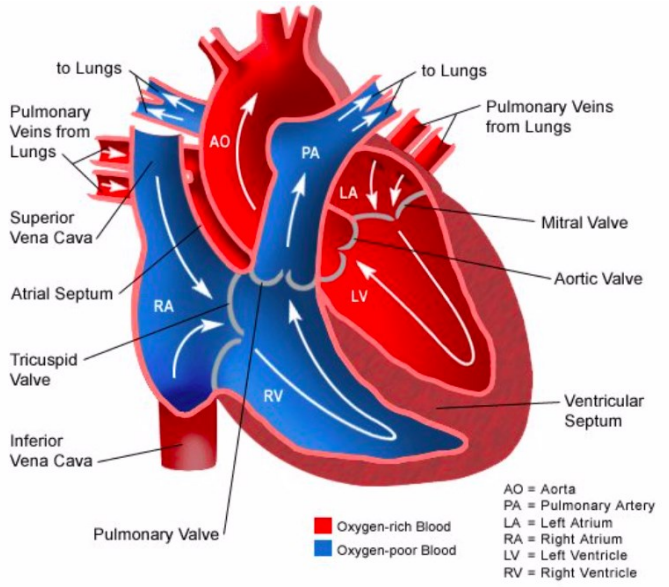

Figure 1: **Anatomy of the heart.** Frontal section of the heart. Arrows indicate the main components. From [1].

The heart is protected by the pericardial sac, which also ensures to keep it in place. The muscle is divided into four cardiac chambers: the right atrium and left atrium are located in the posterior-superior region, while the right and left ventricles in

the antero-inferior one. The right atrium (RA) directly communicates with the right ventricle (RV) through the atrioventricular (AV) orifice, which presents a valve called the tricuspid valve, because it is made up of three cusps which are fibrous and avascular flaps; their free edge is linked to chordae tendineae, cords of fibrous tissue that come from the papillary muscles located on the inner surface of the RV.

Similarly, the left atrium's chamber (LA) and the left ventricle (LV) are connected by a valve known as the bicuspid or mitral valve, which is formed by only two cusps. The two right cavities do not communicate with those on the left since they are separated by a continuous wall; the upper portion is called interatrial septum and separates the two atria, while the lower portion, the interventricular septum, separates the two ventricles.

The pulmonary valve is situated between the RV and the pulmonary artery, while the aortic valve is located between the LV and the aorta. The correct functioning of the four valves is essential to ensure the unidirectionality of the blood flow during the cardiac cycle, which is determined by the pressure gradient, preventing retrograde flows.

The heart can be thought of as two distinct pumps acting in series. The RA and RV pump blood from the systemic veins into the pulmonary circulation, while the LA and LV pump blood from the pulmonary veins into the systemic circulation.

In particular, the right atrium receives non-oxygenated blood from the systemic circulation via the inferior vena cava and the superior vena cava, as well as from the heart itself, through the coronary sinus. Blood flows from the RA to the RV, which then pumps it through the pulmonary arteries into the pulmonary circulation.

The oxygenated blood refluxing from the pulmonary circulation is collected in the LA through the four pulmonary veins, and from there, it enters the LV, which contracts to pump the fluid through the aorta back into the systemic circulation. The branches of the vascular network, which enable the blood to reach the peripheral tissues, all originate from the aorta [2].

2.1.2 Cardiac microscopic anatomy

The three main types of cells that form the heart wall are fibroblasts, endothelial cells, and cardiomyocytes, where the latter constitutes about 75% of the entire cardiac mass. The wall is composed of three overlapping layers in section: the epicardium, myocardium, and endocardium (*Figure 2*).

The outermost layer is the epicardium which consists of a loose layer of connective tissue that adheres to the myocardium beneath and a serous membrane made of a superficial mesothelium sheet.

The main and thickest layer, the myocardium, allows the organ to contract. It is composed of cardiac striated muscle tissue, connective tissue, blood vessels and nerves. The myocardium represents the muscular component of the heart wall.

The endocardium is the innermost layer, it is thin and made of epithelial cells that line the heart's chambers and valves as well as the entire circulatory system.

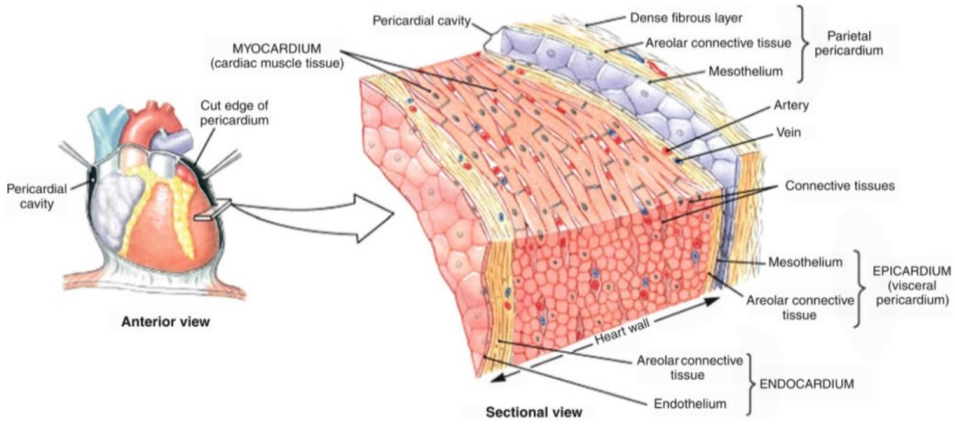

Figure 2: **Layers of the heart.** The epicardium is the outermost layer of the heart and it is made of mesothelial cells; the myocardium is the muscle layer of the organ and it is functionally the main constituent of the organ, made of cardiomyocytes; finally, the endocardium is the innermost layer and it is made of connective tissue and endothelial cells. From [3]**.**

Cardiomyocytes, striated cells with a diameter of around 10-20 μm and a length of about 50-100 μm, are the individual components that compose the myocardium. They have a cylindrical shape and the ends are frequently split into two or more branches that connect to the branches of adjacent cells.

The heart muscle is classified as a functional syncytium, meaning that all cells contract synchronously under the control of the heart's electrical system. It is the proper three-dimensional organization of the cells and their connections that makes the heart a functional syncytium. Indeed, the cardiomyocytes are arranged in a complicated three-dimensional network and are connected through the intercalary discs, which are specialized structures in the contact zones of the individual cardiomyocytes, containing gap junctions that enable nearly free ion flow between adjacent cells.

The plasma membrane of cardiomyocytes, the sarcolemma, forms characteristic invaginations called T-tubules, which penetrate to the center of the cell (*Figure 3*). These structures are crucial for the proper action potential (AP) propagation because they guarantee synchronized depolarizing current propagation. The sarcoplasmic reticulum, a large smooth endoplasmic reticulum found inside the cells, produces a single dilated terminal cisternae that is connected to the T-tubules at the Z-line: this complex is called a dyad. Instead, the structure formed by a T-tubule surrounded on the right and left by the cisternae of the sarcoplasmic reticulum is named a triad; this configuration favors a rapid supply of calcium ions, which are essential for muscle contraction [4].

More in detail, the heart is composed of two syncytia, since an electrically non-conductive fibrous layer surrounding and supporting the valves separates the atria from the ventricles. Therefore, to enable appropriate transmission of electrical excitation from the atria to the ventricles, a particular cardiac conduction system is needed.

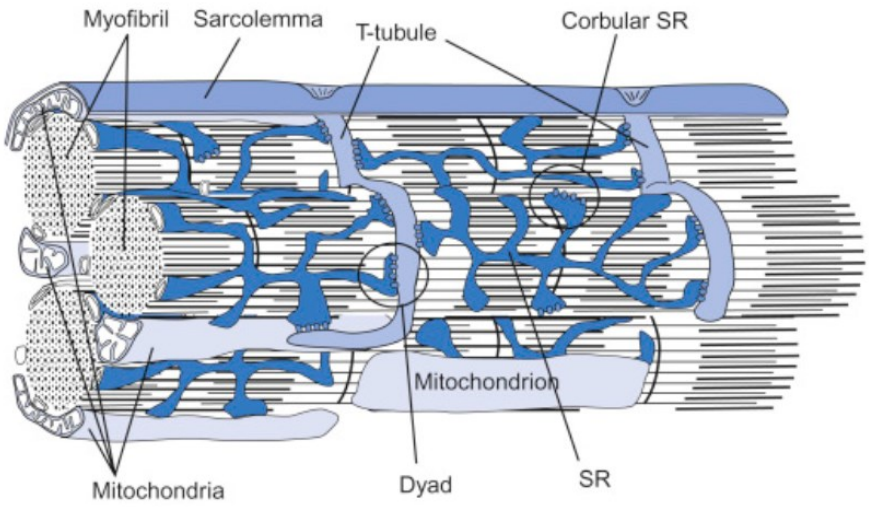

Figure 3: **Schematic illustration of the internal structures of an adult ventricular cardiomyocyte.** T-tubule and sarcoplasmic reticulum organization in ventricular cardiomyocytes[5].

2.1.3 Cardiac conduction system

The contractile activity of the heart muscle is defined as “myogenic” because it is generated by signals that come from the muscle itself.

Cardiomyocytes are specialized cardiac muscle cells that are interconnected in a network and that are able to initiate and propagate a signal named action potential (AP), a wave of cell membrane depolarization that spreads across the tissue, responsible for the synchronized contractions of each cardiac cycle. A small number of modified muscle cells, known as autorhythmic cells and crucial for the pumping action of the heart, are responsible for the heart's capability of producing signals that periodically stimulate its contractions. Two different types of autorhythmic cells compose the cardiac conduction system: pacemaker cells, which induce AP and regulate heart rate, and conduction fibers, which propagate AP throughout the entire heart.

Pacemaker cells are situated in two distinct regions of the heart: the sinoatrial (SA) node, located in the upper part of the RA, and the AV node, localized in proximity of the tricuspid valve. The SA node generates the heartbeat by sending an electrical impulse that depolarizes and contracts the atria.

The electrical signal propagates towards the AV node, spreading the wave to His bundle which consists of conduction fibers situated in the interventricular septum. The His bundle is split into two branches, each of which directs the wave's propagation to one of the ventricles. The AP wave then gradually passes through a vast network of branches known as Purkinje fibers, which, with their thin terminal branches, penetrate the myocardium arriving at the apex of the ventricles. These structures together allow the common depolarisation front to be transmitted to all the cardiomyocytes.

The delay in the propagation of the AP from the atria to the ventricles is in the order of 170-200 ms and enables the separation of the mechanical contraction of the atria from that of the ventricles: as a result, atrial contraction happens before ventricular contraction.

However, if the SA node fails in generating impulses, or if conduction between the nodes is blocked, the AV node starts producing them, in order to guarantee the normal ventricular contraction[6].

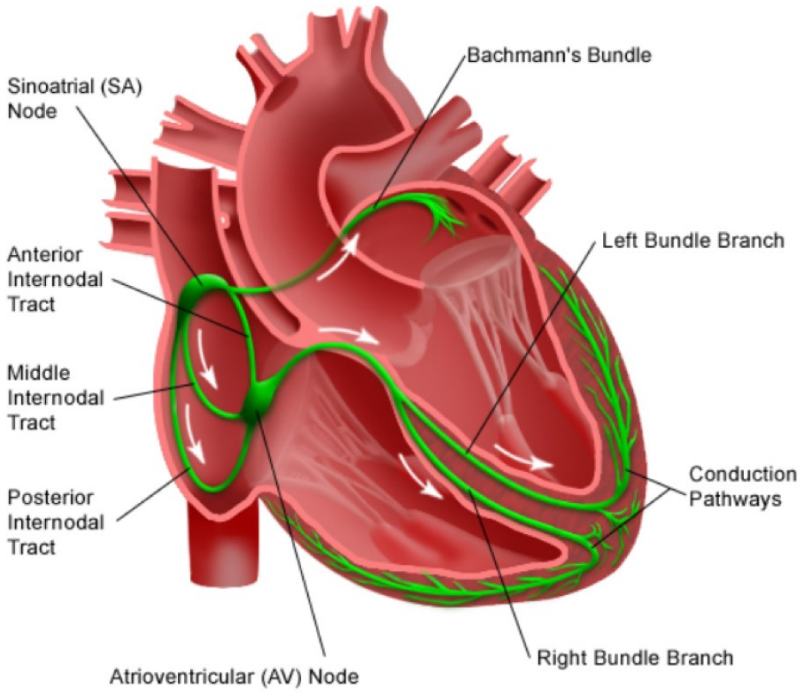

Figure 4: **Electrical conduction system in the heart.** The anatomical pathways of the cardiac conduction system are shown in a four chamber view. From [7].

2.1.4 Cardiac cycle

The cardiac cycle is the period of time that begins with contraction of the two atria and ends with the ventricular relaxation. We refer to the period of contraction, during which the blood is pumped into the circulation, as systole, while the period of relaxation during which the chambers are filled with blood is called diastole. The cycle begins with the diastole phase, during which the AV valve opens and allows blood entering the atria. Because the ventricular pressure is lower than the aortic pressure, the semilunar valves are closed. At the end of the diastole the atria contract (atrial systole), thus the atrial pressure rises above the ventricular pressure, and the AV valves allow blood to flow into the ventricles. At this point the atrial systole ends and the ventricles contract (ventricular systole). The ventricular systole is composed of two phases: isovolumetric ventricular contraction and the ventricular ejection. Although ventricular pressure increases during the isovolumetric ventricular contraction phase, it is not enough to allow the semilunar valves to open and evacuate the blood from the ventricles. The AV valves close as their cusps are pushed upwards by the pressure of the blood mass in the ventricles, and the amount of blood in the ventricles remains constant. The ventricular pressure rises and overcomes the aortic pressure during the ventricular ejection phase, thus opening the semilunar valves as a result. Blood is pushed into the aorta and pulmonary arteries, leading to the drop of the ventricular pressure; as soon as it becomes lower than the aortic one, the semilunar valves close again. The following diastole begins again: when the blood enters the atria, it is not capable of flowing into the ventricles since the AV valves are closed; they open as soon as the ventricular pressure decreases again, thus beginning another cardiac cycle (*Figure 5*).

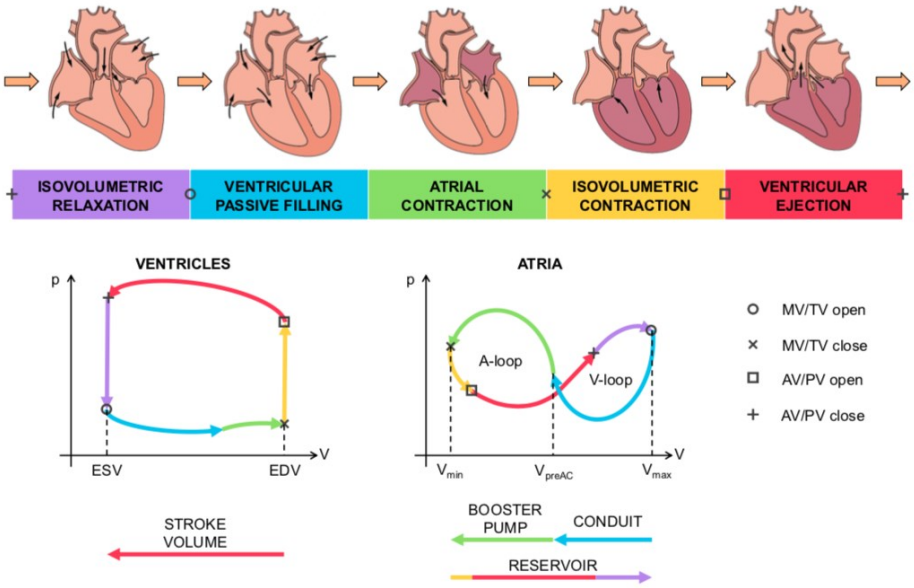

Figure 5: The phases of the cardiac cycle. On the top, a sketch of the direction of the blood flow, the status of the valves and the contraction of the chambers (darker color) during the different phases; on the bottom, schematic ventricular and atrial pressure-volume loops with the opening and closing of the valves and colored with the five phases [8].

2.2 Cardiac electrophysiology

2.2.1 Action potential physiology

A cardiomyocyte has an electrical membrane potential of roughly -90 mV at rest, where membrane potential is defined as the difference in potential between the two sides of the sarcolemma.
The cardiac AP is a momentary alteration in the membrane potential across the plasma membrane of cardiac cells. Indeed, in response to a stimulus, the cardiomyocyte membrane potential becomes less negative: if it falls below the threshold value of -60 mV, an AP is produced. The AP is an all-or-none event, meaning that once the threshold value is reached, the stimulus no longer affects the AP's amplitude [9].

Furthermore, due to the presence of structural proteins called gap junctions, all cardiomyocytes are electrically synchronized, since they permit cell to cell AP propagation. Gap junctions are proteins that belong to the connexins family of proteins; they distribute to form a pore through which ions can pass (including Na^+, $Ca2^+$ and K^+).

The two primary categories of cardiac muscle cells are:

- self-excitable, autorhythmic cells (pacemakers) that can generate and propagate the AP;
- working cells, which generate force and are primarily responsible for cardiac contraction.

These two types of cells have distinct functions and resting membrane potentials. The working cells have a five-phase AP (*Figure 6*):

- Phase 0 consists of a rapid depolarization due to the intense inward Na^+ current. These Na^+ channels are voltage-dependent and their opening is triggered by cell depolarization. The channels are almost immediately closed by a time-dependent closure mechanism that produces a transitory current with rapid kinetics. The result is a depolarization of the membrane potential, which reaches values of +30/+40 mV.

- Phase 1 is characterized by a rapid repolarization, due to the opening of K^+ channels, which then close quickly, permitting a rapid outflow of K^+. This current is named transient outward K^+ current (I_{to}).
- Phase 2 is referred to as the plateau phase. Indeed, due to the balance of repolarizing and depolarizing currents, the resting membrane potential remains nearly constant. In this phase, repolarizing K^+ current activated by slow delayed rectifier K^+(I_{Ks}) channels is contrasted by a slow and inward Ca^{2+} current, activated by the Ca^{2+} L type channels (I_{CaL}), also known as DiHydroPyridine Receptor (DHPR). Moreover, sarcoplasmic reticulum starts to release Ca^{2+} slowly in response to Ca^{2+} entering the cell through L-type channels; this process is referred to as calcium-induced calcium release.
- Phase 3 is the phase of rapid repolarization that restores the resting membrane potential. First, L-type Ca^{2+} channels close whereas I_{Ks} channels are still open. This guarantees a repolarizing current, which permits the opening of more varieties of K^+ channels as the inward rectifying K^+ (I_{K1}) channels and the rapid delayed rectifier K^+ (I_{Kr}) channels.
- Phase 4 is the phase during which membrane potential becomes stable at resting potential. I_{K1} current controls this phase by preventing working cardiomyocytes from depolarizing before the generation of a new AP.

The AP produced by cardiac pacemaker cells, however, is substantially dissimilar from that of working cells. First of all, the resting membrane potential value of pacemaker cells is less negative, approximately -55/-60 mV. Additionally, when the membrane becomes hyperpolarized after a previous AP, Na^+ voltage-dependent channels open and this current is called funny (I_f).
The I_f leads to an inward Na^+ flow, enabling a gradual depolarization over the threshold which triggers the generation of a new AP. Another characteristic of pacemaker cells is the presence of a transient Ca^{2+} current (I_{CaT}), controlled by low voltage calcium channels that open during cell depolarization and deactivate during cell hyperpolarization.
The two currents together (I_f with I_{CaT}) depolarize the cell until the L-type Ca^{2+} channels open and phase 0 begins. The same currents implicated in working cells characterize phase 3 also in pacemaker cells: activation of I_K paired with

inactivation of I_{CaL}. Due to the slow closure of K^+ channels at the end of an AP, the repolarizing effect of I_K is moderate, thus promoting depolarization and the start of a new AP. Indeed, in pacemaker cells the final phase is no longer called the resting phase, but "spontaneous slow depolarization phase", and it is the mechanism allowing cardiac automatism [10].

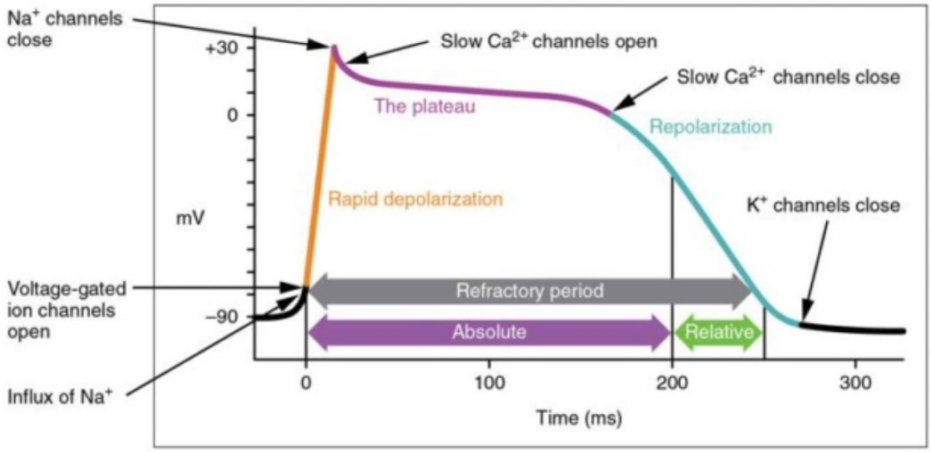

Figure 6: **Action potential of a cardiac cell.** Representation of the membrane action potential phases in a cardiomyocyte. From [11].

2.2.2 Excitation-contraction coupling

The physiological process known as excitation-contraction coupling (ECC) converts an electrical stimulation into a mechanical reaction, which causes the contraction of the heart muscle.

Calcium ions (Ca^{2+}) play an important role as second messengers controlling a variety of biological processes[12]. As an action potential arrives, voltage-gated L-type Ca2+ channels located on the surface membrane (DHPRs) open quickly. The opening of closely spaced intracellular Ca^{2+} release channels, the ryanodine receptors (RyRs), triggered by the inflow of Ca^{2+} via the sarcolemmal Ca^{2+} current (I_{Ca}), releases more Ca^{2+} from the intracellular Ca^{2+} store, the sarcoplasmic reticulum (SR). Ca^{2+} removal mechanisms then transfer Ca^{2+} back into the extracellular space, mainly via the Na^+/Ca^{2+} exchanger (NCX) and into the SR (by the SR Ca^{2+} ATPase, SERCA), which ends the strong contraction that results from the temporary rise in Ca^{2+} [13] (*Figure 7*).

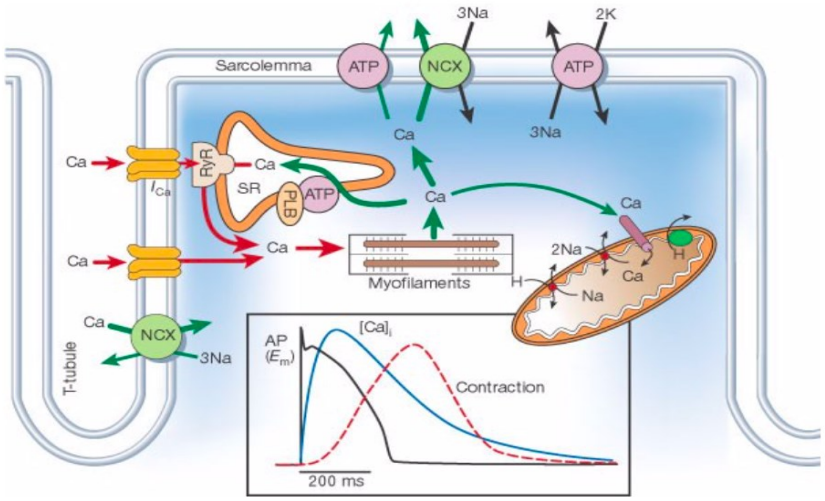

Figure 7: **Ca^{2+} transport in ventricular myocytes.** Inset shows the time course of an action potential, Ca^{2+} transient and contraction [14].

2.2.3 Myofilaments and Ca^{2+}-dependent activation

The smallest contractile unit of muscles, known as a sarcomere, is composed of specialized proteins called myofilaments (*Figure 8*). Within the sarcomere, there are five recognizable bands that give cardiac muscle their striated appearance. The borders of the sarcomere are delimited by two lines called Z-lines, mainly formed by α-Actinin and desmin. On either side there is a clear band called band I (isotropic to polarized light), made up of actin filaments. Going inwards it is possible to notice a dark band called band A (anisotropic to polarized light) made up of interposed actin filaments and myosin filaments. At the center of the A band there is a smaller band called the H band, followed by a thin, darker structure called the M-line. Furthermore, the presence of particular proteins involved in muscle contractile characteristics is responsible for the cardiac striated architecture of sarcomeres. Indeed, the sarcomere is composed of three different types of filaments: titin, thin (actin), and thick (myosin). At the Z-line and extending into the A-band, actin filaments engage with alpha-actinin.

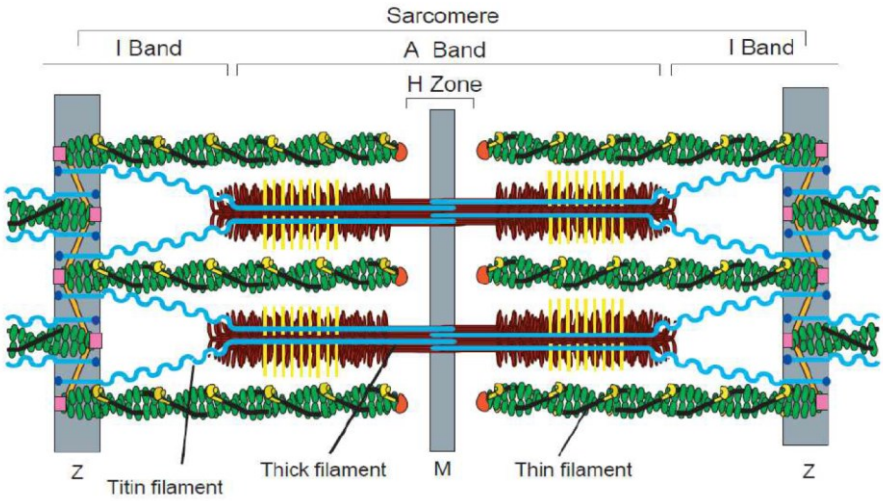

Figure 8: **Sarcomere structure.** Representation of the main sarcomere proteins and of the sarcomere's basic structure[15].

Myosin is made up of thick filaments that extend into the A-band, and their location is secured by their attachment to the titin protein. As previously mentioned, the rise in Ca^{2+} concentration inside the cell causes the contraction.

Indeed, the binding of a protein called troponin C by intracellular Ca^{2+} causes a conformational shift in the troponin complex making accessible the actin-binding site on myosin, thus allowing for actomyosin interaction through cross-bridges formation [16] and a rapid thin filaments activation. When ATP is hydrolyzed, the myosin head changes its binding angle resulting in the motion of thick filaments.

2.2.4 Measurement of cardiac electrical activity

In clinics, the electrical activity of the heart is measured by using the standard 12-lead electrocardiography. The output of the standard 12-lead electrocardiography is called electrocardiogram (ECG)[17] (*Figure 9*). There are three main parts in an ECG:

- P wave is the signal of atria depolarization. By examining its length, amplitude and frequency, atrial anomalies can be found. The PR interval is the space between the start of the P wave's upward slope and the start of the QRS complex. The PR interval lasts between 120 and 200 ms, approximately.

- Repolarization of the atria and depolarization of the ventricles are both reflected in the RS complex. Q, R, and S waves are the three waves that compose the QRS complex. The QRS initial negative deflection is known as the Q wave, its initial positive deflection as the R wave and its initial negative deflection as the S wave. Due to the Purkinje and His cell bundle's rapid conduction velocity, the QRS complex is sharper than the P wave.

- The ventricular repolarization is reflected in the T wave. Absolute refractory period is the amount of time between the start of the QRS complex and the peak of the T wave. Relative refractory period refers to the interval of time between the T wave's peak and its end. A fresh action potential cannot be evoked during the absolute refractory period, although it is possible under specific circumstances during the relative refractory period[18].

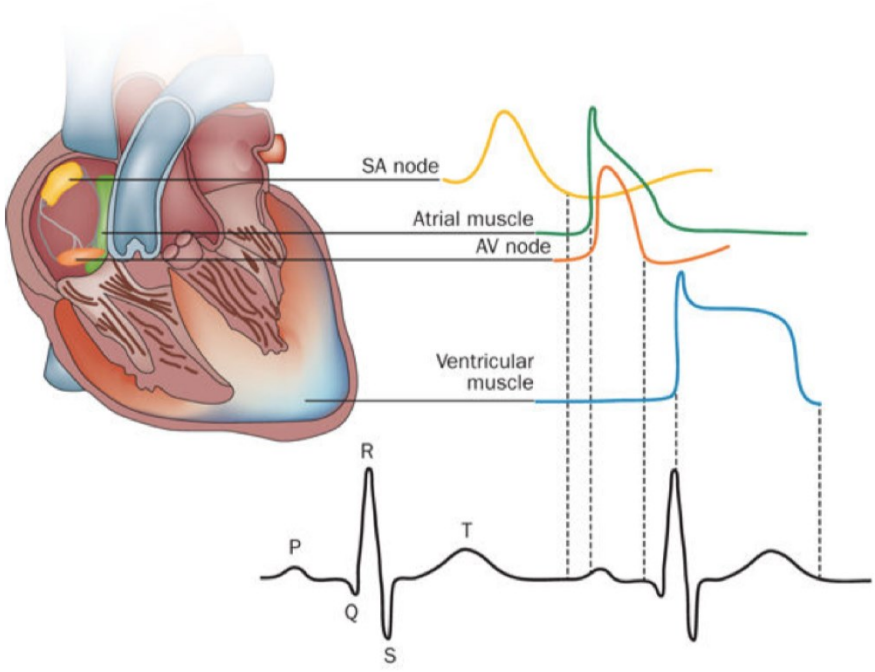

Figure 9: **Schematic representation of the normal cardiac conduction system.** The normal cardiac conduction system is shown together with the correlation between the action potentials of cardiomyocytes in distinct areas of the heart and the surface electrocardiogram [19].

2.3 Cardiac sympathetic innervation

The heart is richly innervated by the autonomic nervous system (ANS)[20] which play a fundamental role in regulating cardiac activity through a combination of receptors, afferent (sensory) and efferent (effector) nerves, and effector systems[21].

The cardiac ANS can be divided into extrinsic and intrinsic components[22]. The intrinsic component consists of primarily autonomic nerve fibers once they enter the pericardial sac, whereas the extrinsic cardiac fibers mediate connections between the heart and the nervous system and may be subdivided into sympathetic and parasympathetic fibers[23]. Sympathetic and parasympathetic neurons exert antagonistic effects on the heart: indeed, the sympathetic component prepares the body for energy expenditure increasing heart rate and myocardial contractility; conversely, the parasympathetic system is most active under restful conditions[24].

Sympathetic nerves innervate the whole mammalian heart, entering the organ from the epicardium and continuing their processes across the myocardial interstitium, running parallel to capillary arteries [25,26]. They come from sympathetic neurons in the superior cervical ganglia, stellate (cervicothoracic) ganglia and thoracic ganglia, which communicate with corresponding cervical or thoracic spinal cord [27] (*Figure 10*).

Sympathetic nerves release norepinephrine (NE) which activates cardiac β-adrenergic receptors, increasing the contraction force (i.e., a favorable inotropic effect)[28] and exerting major effects on electrophysiological properties of the heart [29,30]. Indeed, the activation of β_1 receptors increases heart rate (*via* the SA node) and contractility as a result of increased intracellular Ca^{2+} concentrations and Ca^{2+} release by the sarcoplasmic reticulum, while the activation of β_2 receptors, which are mainly expressed in the coronary circulation, elicits vasodilatation.

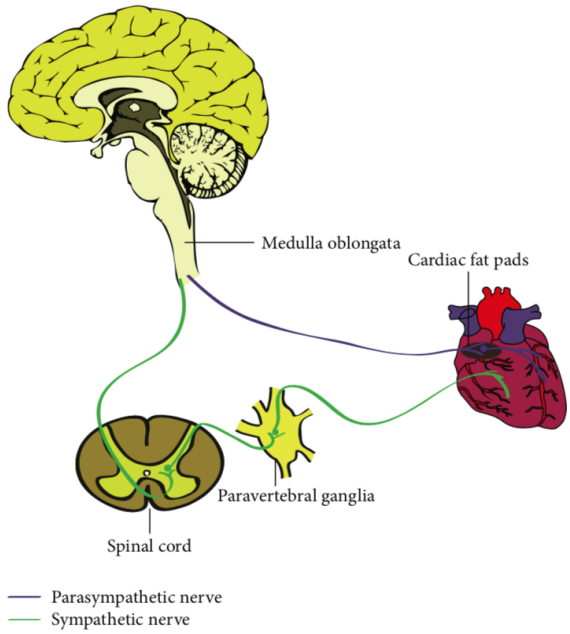

Figure 10: Anatomy and distribution of autonomic innervation of the heart. The cardiac sympathetic nerves come from the paravertebral ganglia and project from the base of the heart into the myocardium, while the parasympathetic neurons in the cardiac fat pads, whose preganglionic fibers are conveyed within the vagus nerve, are the source of the cardiac parasympathetic nerves [31].

2.3.1 Imaging approaches to study cardiac sympathetic nervous system

Despite the key role of the sympathetic nervous system (SNS) in the heart physiology and disease, very little is known about its fine structural organization, which has remained incompletely understood for years, mainly due to technical limitations of the traditional methodologies.

Indeed, the first evidence regarding the presence of nerve processes in the heart was provided employing bright-field microscopy in a study performed in frogs and other vertebrates [32,33] (*Figure 11A*). These unexpected findings prompted studies to explore the physical anatomy of the cardiac SNS in the heart. The following investigations were performed exploiting the Methylene blue coloration, which allowed for the recognition of neurons and their cytoplasmic ramifications in cardiac tissues [34,35]; however, the reagent was non-specific,

binding both to motor, sensory and autonomic nerve fibers, thus preventing the discrimination between the various populations of cardiac neurons.

In order to selectively identify the adrenergic nerve fibers and isolate them from the other neuronal populations in the heart, formaldehyde- and glyoxylic acid-induced fluorescence was then used [36,37], subsequently complemented by the use of the ultrastructural resolution of electron microscopy [38] (*Figure 11B*).

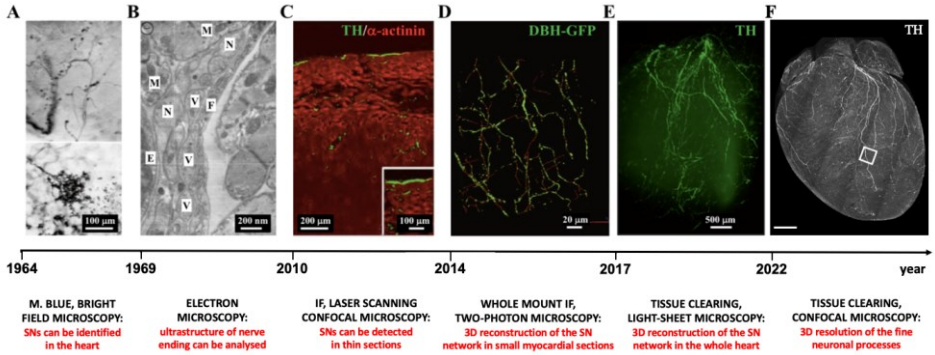

Figure 11: **The evolution of the visualization of the cardiac sympathetic nervous system. A)** Methylene blue coloration was used to stain the nerve terminals in canine left ventricular myocardium. Modified with permission from [32]. **B)** This electron micrograph shows an unmyelinated nerve bundle in a capillary's perivascular area. This bundle includes vesiculated nerve processes that are invested in Schwann cells. The letters N stand for nerve process approaching myocardial cell, V for varicosity of nerve process, M for myocardial cell, F for fibrocystic process, and E for capillary endothelial cell. Modified with permission from [39]. **C)** Double-immunofluorescent staining for TH and a-Actinin in the left ventricle section from a mouse heart. Modified with permission from [40]. **D)** Within a limited volume of the left ventricular sub-epicardium, a 3-D topological skeleton of the sympathetic tree can be seen. Using a semi-automated tracing approach, a complete 3-D skeleton of all green fluorescent axons was created and rendered. Modified with permission from [41]. **E)** Tissue clarification was performed on the sample and the 3D distribution of sympathetic nerves stained with TH-antibody across the mouse heart is visualized through the use of a light-sheet microscope. Modified with permission [42]. **F)** The heart was subjected to a tissue clearing protocol, stained with TH-antibody and imaged with a confocal microscope [43]. Figure modified [38].

These studies, performed on many animal models, provided crucial information, showing that sympathetic and parasympathetic neuronal processes coexist in various heart areas, with sympathetic over parasympathetic neurons predominance in the ventricles [39,44]. However, even though highly relevant, the identification of a number of interconnected neuronal subtypes suggested the existence of complex neuronal circuits within the heart walls, thus highlighting the limitation of studying cardiac innervation in 2D and the need to obtain 3D information. Therefore, most neuro-cardiology studies conducted over the past 50 years have taken advantage of newly developed confocal fluorescence microscopy [25,26], which enables optical sectioning, high spatial resolution and contrast. This method was used to define the 3D topology of heart innervation by analyzing heart sections and identifying neuronal processes through the use of antibodies, specific for NE biosynthesis enzymes like tyrosine hydroxylase. This approach was able to produce the first 3D reconstruction of the cardiac sympathetic neural network, although only in small heart volumes (*Figure 11C*).

Thus, in the past few years, researchers have set a new goal: the 3D reconstruction of the complete heart innervation at subcellular resolution. However, high-resolution optical imaging in large-scale specimens is extremely difficult to perform, since it is limited by the phenomenon of light scattering, related to the refractive index (RI) mismatch of the biomolecules [45,46] (*Figure 12*). This means that light rays that should travel in straight lines are deviated many times as the light is reflected off by molecules, membranes, organelles and cells of the tissues [46].

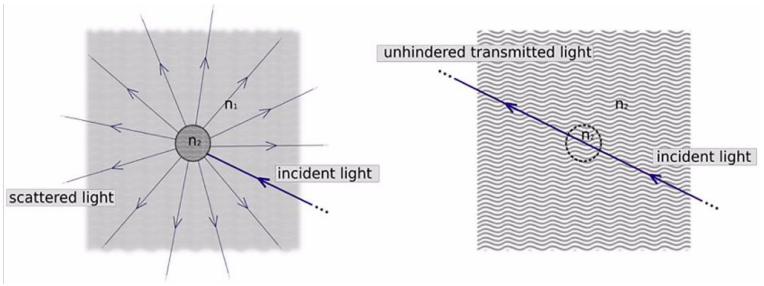

Figure 12: **Schematic representation of light scattering before and after an optical clearing procedure.** On the left, light is scattered due to the different RI (n1 ≠ n2) that it encounters. On the right, light is not deflected since the RI has been matched (n1 = n2). From [47].

Indeed, biological tissues are essentially composed of high-refractive index molecules (such as lipids and proteins) immersed in a low-refractive medium (water) [48]. Therefore, this mismatch leads to the deflection of the light employed for the observation of the samples: the sample appears opaque and penetrating in depth results in a loss of resolution [47].

Recently, the restrictions imposed by the inherent nature of biological tissues have been overcome by the development and the ceaseless optimization of a number of methodologies, called "tissue clearing methodologies". Tissue clearing refers to a collection of techniques that render biological samples transparent, enabling the deep imaging of large tissue volumes using light microscopy approach [49] (*see appendix 6.1*).

In the last few years, several studies have tried to employ these methodologies to obtain 3D reconstructions of the SNS in massive cardiac tissues. The first study, by Yokoyama *et al.*[42], employed the CUBIC technique[50] together with light-sheet microscopy to reconstruct the transmural distribution of sympathetic nerves. However, the resolution achieved in whole volume imaging was unable to resolve the finer details of myocardial neuronal processes, thus still leading to a missing information (*Figure 12E*).

Subsequent studies that took advantage of tissue clearing protocols and two-photon microscopes were carried out[51,52] to increase the image resolution, but they succeeded in the 3D investigation only of small sections of tissue or in the heart of small animal models (*Figure 12D*).

Finally, a study performed by Zhu *et al.*[43] in 2022 exploited the iDISCO protocol[53] to clear entire hearts together with confocal microscopy, in order to achieve a higher resolution of the images (*Figure 12F*). The pipeline allowed the resolution of thin neuronal processes, thus providing a much more comprehensive view of the organization of the sympathetic neuronal network in mouse hearts, ultimately showing the potentialities of combining optical clearing techniques with novel imaging systems to further investigate the SNS fine structural pattern.

2.4 Pathophysiology of myocardial infarction

Despite a decrease in overall cardiovascular mortality over the past decades, ~17 million deaths a year occur worldwide as a result of cardiovascular diseases [54].

Myocardial infarction (MI) is one of them and it is defined as myocardial cell death due to prolonged ischemia [55]. MI affects millions of people every year and those who survive have a higher risk of developing malignant arrhythmias and sudden cardiac death. Adverse left ventricular remodeling following MI constitutes the structural basis for ischemic heart failure (HF), and involves complex short- and long-term changes in LV size, shape, function, cellular and molecular composition [56,57](*Figure 13*).

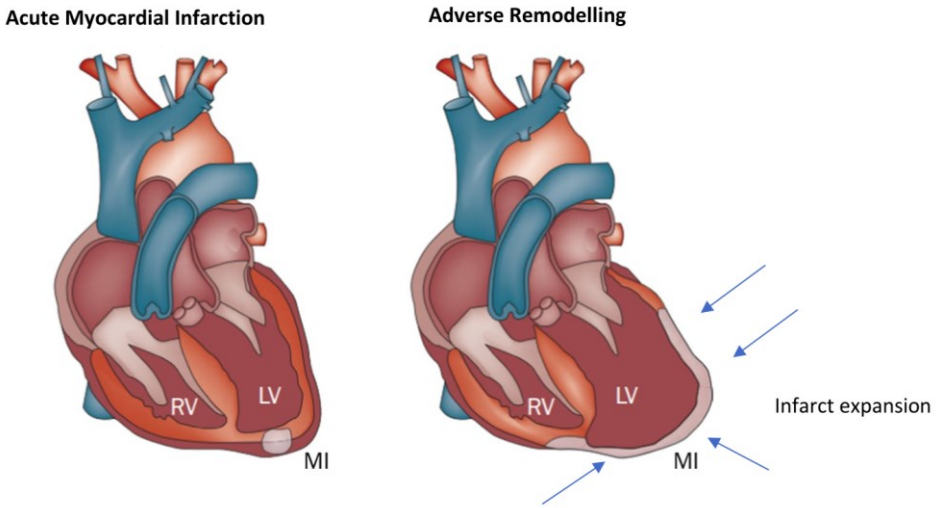

Figure 13: **Adverse ventricular remodeling after MI.** The schematic depicts the overall effects of adverse post-MI cardiac remodeling [58].

2.4.1 Cardiac repair after MI

Multiple pathophysiological factors are responsible for the remodeling of the heart after MI; however, the fundamental determinants of this process (and its progression to clinical HF) are the extent of the initial infarction and the effectiveness of the post-MI reparative process [59].

Cardiac repair after MI is started by intense sterile inflammation and immune cell infiltration (inflammatory phase) that serve to digest and clear damaged cells and extracellular matrix tissue [59]. This initial phase is followed by a reparative phase characterized by the resolution of inflammation, (myo)fibroblast proliferation, scar formation and neovascularization over the following few days [60,61] (*Figure 14*).

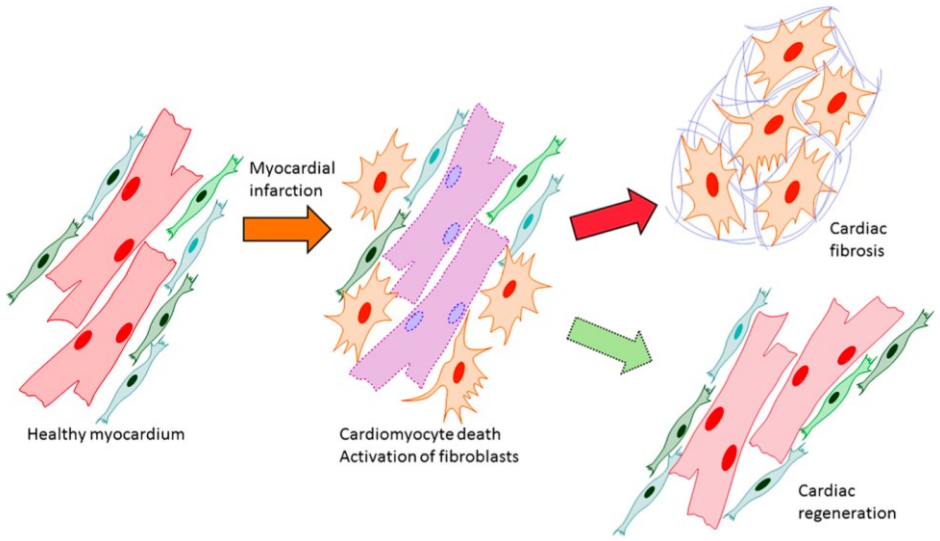

Figure 14: **Reparative response following a myocardial infarction.** Myofibroblasts are activated as a result of hypoxia-induced cardiomyocyte mortality, which causes a reparative fibrotic response in the wounded area [62].

Determining factors of the effectiveness of wound healing include the appropriate and prompt containment and resolution of inflammation: for ideal repair, a suitable physiological balance must be achieved between these two stages [63,64]. An excessively protracted, large, or inadequately suppressed

inflammatory phase can therefore result in sustained tissue injury and poor healing, defective scar formation, increased cell loss and contractile dysfunction, which lead to infarct growth, adverse remodeling and chamber dilatation.

The fibrotic response after a MI can be classified into two types of fibrosis, namely replacement and reactive fibrosis, both of which are mediated by fibroblasts and myofibroblasts [62]. After an ischemic insult, replacement fibrosis (or scar formation), is a crucial step to stop the ventricular wall from rupturing [65,66]). In adult mammals, the fibrotic scar formed at the infarcted area is permanent and promotes reactive fibrosis in the uninjured myocardium [62]. Indeed, the increased mechanical stress following a MI also causes connective tissue to grow in sites far from the infarction. This reactive fibrosis affects chamber compliance and increases ventricular stiffness, which reduces cardiac output in the infarct border zone (BZ) and in the distant, unharmed myocardium.

2.4.2 Myocardial infarction-induced functional defects

The remodeling leads not only to the described long-term structural alterations in the ventricular form (including infarct enlargement, myocardial thinning, ventricular dilatation and hypertrophy of the distant non infarcted myocardium), but also to functional defects [58]. Indeed, both the fibrous scar and interstitial fibrosis have been demonstrated to interfere with the heart normal electrical activity and to predispose to arrhythmias in addition to their impact on cardiac contractility [62,67]. Re-entry, triggered activity and automaticity are three fundamental mechanisms that might contribute to the onset or maintenance of arrhythmias after a MI [68] (*Figure 15*).

- The re-entry mechanism is an aberrant impulse that travels backward rather than through the normal conduction system, around an area of unidirectional block and re-excitement of previously activated cardiomyocytes, leading to circular conduction patterns [54]. Patients who have had a prior MI, scarring or fibrosis with unidirectional conduction block frequently experience re-entrant circuits [69].

- Triggered activity is defined by early or delayed after-depolarizations that may occur in the Purkinje fibers or in ventricular myocardium. Early after-depolarizations (EAD) are caused by the inward L-type calcium channels being reactivated, while it is believed that delayed after-depolarizations (DAD) are caused by increased intracellular calcium, which enhances the inward current produced by the sodium-calcium exchange. This mechanism causes a sodium influx that triggers an AP [70].

- Automaticity is caused by myocardial stretch or short-circuit and injury currents in the BZ, leading to spontaneous depolarizations outside the sinus node. Improved automaticity happens when lower transmembrane voltage diastolic thresholds, most frequently in the Purkinje fibers, cause premature depolarization and impulse propagation. This can be observed in conditions of excess catecholamine, acute ischemia and altered electrolytes [71].

The compact scar may serve as an insulated non-excitable area that anchors re-entrant arrhythmia leading to sustained ventricular tachycardia [72]. On the other hand, the non-conducting fibrillar collagen network between the cardiomyocyte

layers in interstitial fibrosis may encourage re-entrant tachycardia by causing localized ectopic activity and by delaying or blocking conduction [67].

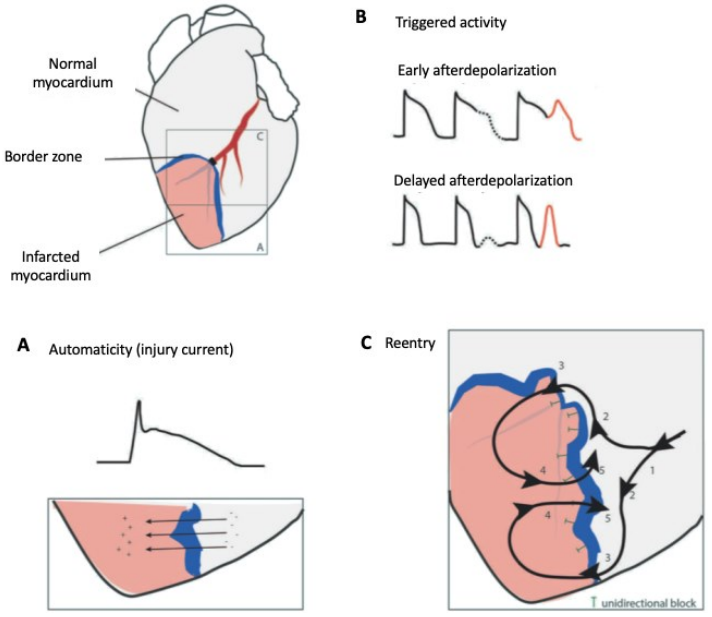

Figure 15: The three mechanisms that can lead to infarcted-related arrhythmias. Automaticity (**A**), triggered activity (**B**), and reentry (**C**) can play a role in arrhythmogenesis during ischemia. (**A**) Injury current across the border zone leading to ST elevation in the electrocardiogram, (**B**) Triggered activity mainly caused by Ca2+ overload in cardiomyocytes or Purkinje fibers. (**C**) Reentry. Electrical activation wavefront (1) is deflected at the border zone due to unidirectional block into two wave fronts (2), eventually passing the border zone (3) and exciting the infarct zone (4) and finally passing the unidirectional block re-exciting the area in front of the block (5). Image modified from Sattler [54].

2.4.3 Premature ventricular complexes

Premature ventricular complexes (PVCs) are ectopic beats that arise from within the ventricles and are indeed the most common ventricular arrhythmia in healthy individuals, frequently observed on ECGs [73] (*Figure 17*) or during rhythm monitoring [74]. Patients present either without symptoms, acutely symptomatic due to PVCs themselves, or with progressive symptoms from the cumulative effects that frequent PVCs can have on myocardial contractility [69]. Incidental PVCs are typically regarded as innocuous, despite the fact that they may cause symptoms like palpitations or dizziness [75]. However, highly frequent PVCs can eventually have a negative impact on the left ventricular function and may result in or worsen heart failure [76,77].

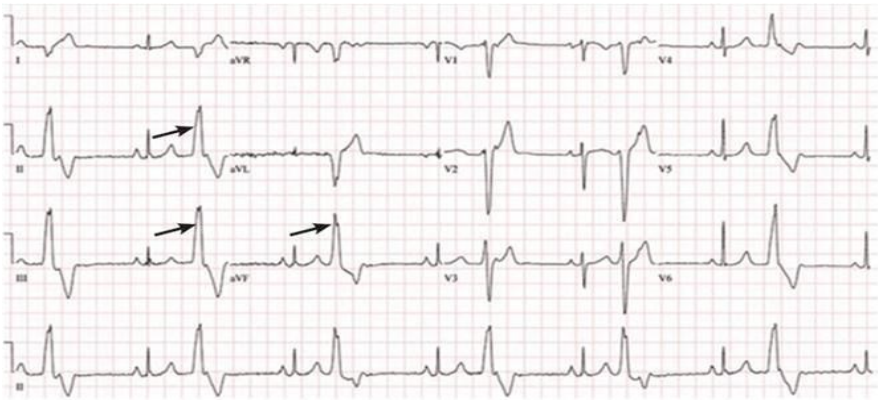

Figure 17: Typical configuration of right outflow tract premature ventricular complexes (PVCs) in the 12-lead electrocardiogram. The PVCs exhibit a tall R wave in the inferior leads (arrows) and a left bundle-branch block pattern [78].

Electrocardiographically, PVCs are defined as a premature QRS complex with an abnormal morphology and duration greater than 120 ms [79]. Individuals with multiple abnormal QRS complexes are classified as having multifocal or polymorphic PVCs and this condition is associated with increased risk of mortality and major cardiovascular events [80].

The three most plausible mechanisms involved in the pathophysiology of PVCs are re-entry, triggered activity and automaticity; however, the most typical mechanism for PVCs is believed to be re-entry.

As described above, the presence of fibrotic patches can lead to these three pathophysiological mechanisms of arrhythmias induction; thus, PVCs are frequently a drawback of post-MI remodeling and they are most frequently the initiating event of post-MI arrhythmias, as seen in recordings from intra-cardiac devices and monitoring investigations [81,82].

Some studies have shown evidence that PVCs are often preceded by sympathetic activation, suggesting a causal relationship [83]. There is, however, a shortage of *in vivo* information about the mechanisms underlying spontaneous adrenergic-driven PVCs and arrhythmias, as well as if PVCs are the result of events initiated at cellular level and whether they occur in specific sites. According to studies performed on isolated cardiomyocytes, post-MI remodeling encourages spontaneous calcium release and delayed afterdepolarizations (DADs), which may cause PVCs in vivo [84,85]. Priori *et al.*[86] showed a connection between sympathetic stimulation, DADs and triggered PVCs in structurally normal hearts using monophasic action potential (MAP) recordings performed *in vivo*. Recently Dries et al.[82] validated this connection by finding an increased occurrence of DADs in MAPs obtained at random locations in the proximity of a MI during adrenergic stimulation.

Clinical observations seem to indicate that, in patients who have suffered a MI, PVCs are confined to sites within the BZ [87,88]. In order to investigate this hypothesis, in 2021 Amoni *et al*.[89] validated a protocol to tag PVC sites *in-vivo* and record simultaneous MAPs in a pig model after a MI induction by using an augmented reality angiography. They indeed identified discrete dominant cluster sites of PVCs close to the infarct BZ (*Figure 18*) by recording spontaneous events and noticed the tendency of PVCs to clusterize in the BZ across animals, even if in different locations, indicating the unique BZ remodeling of each individual that locally creates vulnerable sites.

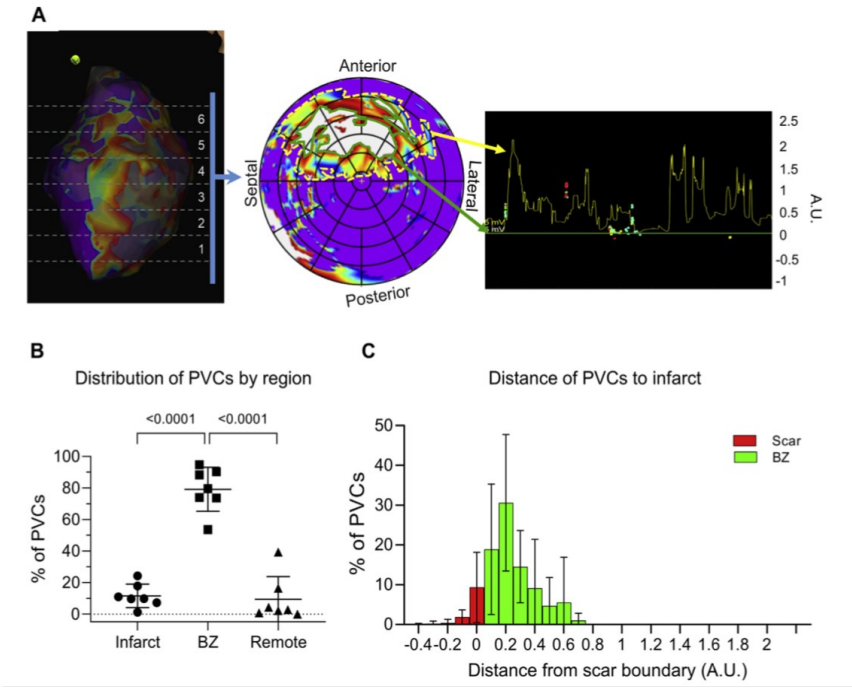

Figure 18: **Spatial distribution of PVCs and distances from the scar boundary. A)** The 3D LV geometry (left) of the contact voltage map is transformed to a 2-dimensional polar map (middle) by segmentation into 6 levels with 12 radial spokes. Right: The scar boundary is set as the zero reference, and PVC distances are calculated in arbitrary units (A.U.). **B)** PVCs by region, per pig. ANOVA with Bonferroni post-test. **C)** Distribution of PVCs for distance to the scar boundary [89].

When testing if there was a direct connection between sympathetic-driven DADs and PVCs in vivo, they noticed a DAD that appeared to cause an AP, with the AP taking off 10 ms before the corresponding PVC on the surface ECG (*Figure 19*). This occurrence predominantly happened in infarcted animals (89%), where APs caused by sympathetic-driven DADs were only observed in PVC sites.

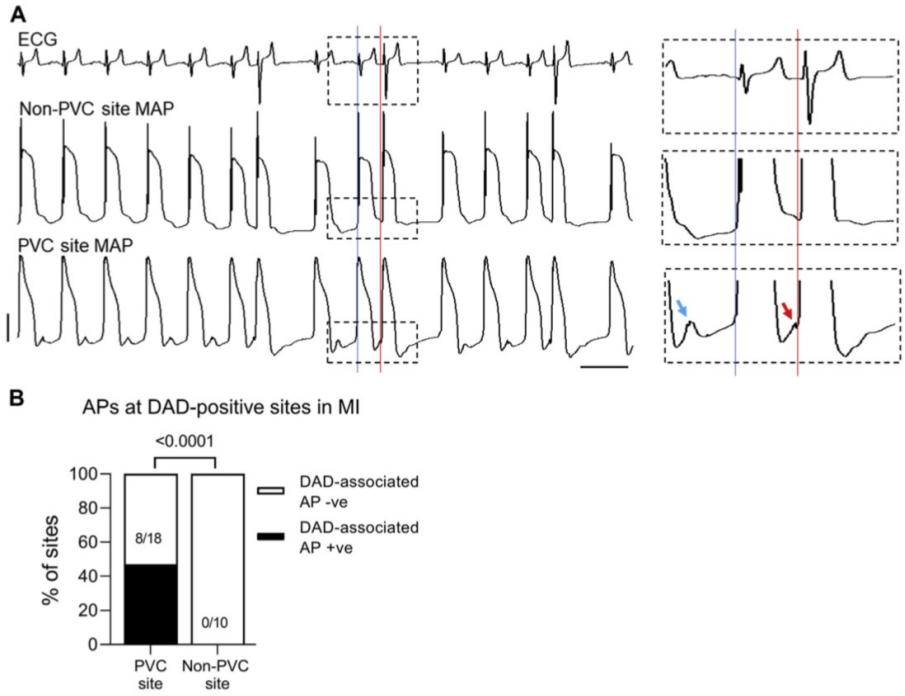

Figure 19: Association of DADs to occurrence of spontaneous action potentials. **A)** Example of frequent DADs (blue arrow) that are associated with spontaneous action potential (AP) (red arrow) that translates to a PVC on the electrocardiogram (ECG). **B)** Sites with observed DAD-associated APs in MI are restricted to PVC sites. Fisher exact test. From [89].

These results suggest that in hearts post-MI, arrhythmias initiate from discrete vulnerable areas within the BZ, where DADs related to increased adrenergic response of BZ cardiomyocytes can generate PVCs [89].

2.4.4 Sympathetic nervous system remodeling following MI

The susceptibility of arrhythmias in MI is not only due to the formation of a large, non-conductive fibrotic scar, but numerous studies have shown that also altered sympathetic neurotransmission in the heart plays a key role in the initiation of post-MI cardiac arrhythmias [90–93].

Indeed, sympathetic activation exerts significant effects on electrophysiological properties such as automaticity, refractoriness, and conduction velocity of myocardial cells [29,30].

Thus, a spatial inhomogeneity in cardiac SNS can result in the spatial inhomogeneity of these electrophysiological properties and therefore facilitate the initiation of ventricular arrhythmia. Indeed, studies show that simply disrupting the normal organization of sympathetic innervation in an otherwise healthy heart is pro-arrhythmogenic [25,94,95].

Cardiac conditions such as MI may result in sympathetic nerves injury [96,97]. Studies focused on post-MI adverse remodeling have demonstrated that MI could result in alteration of the distribution and amount of sympathetic fibers within the tissue. According to three recent investigations in patients with implantable cardioverter defibrillators [98–100], the quantification of sympathetic alterations following a MI may be a good indicator of the likelihood of developing significant ventricular arrhythmias. Moreover, Gardner *et al.*[95], tested whether restoring sympathetic innervation to the infarct and surrounding myocardium affected post-MI arrhythmia susceptibility. Using both genetic and pharmacological approaches, they found that infarcted hearts with restored sympathetic innervation were electrically indistinguishable from control hearts, despite the presence of a scar, thus validating the fundamental role of the SNS alterations in the induction of arrhythmias. Recently, in 2022 Sepe and coworkers[101] validated this result by demonstrating that the use of two therapeutics able to shift the immune response from inflammatory to reparative could stimulate the heart reinnervation and prevent arrhythmias.

Abnormal spatial sympathetic innervation leads to accentuated dispersion of repolarization and increased automaticity and triggers activity, which is underlying the susceptibility to, and initiation of, malignant arrhythmias [31].

However, if the remodeling that occurs after a MI results in a loss or in a gain of sympathetic nervous fibers is still not clear. Previous investigations have shown controversial results in this regard, thus rendering the impact of the sympathetic fibers remodeling in the infarcted tissue difficult to understand.

Zipes *et al.* were among the firsts to show the degeneration and death of sympathetic fibers within the scar [97]; in addition, sites of sympathetic denervation have also been shown to exist outside the infarcted area in the viable myocardium [96,102–104].On the other hand, some studies have reported sympathetic nerve sprouting that occurs in response to nerve injury after infarction [105,106] and that can lead to a sort of compensatory hyperinnervation [107].

This coexisting occurrence of results, showing both denervated and hyper-innervated sites in the myocardium after an infarct [108] suggested the hypothesis that the SNS remodeling that occurs after MI is region-specific, with this derived inhomogeneity being the leading cause to predispose to arrhythmias[107,109–112].

To validate this hypothesis, in a leading study performed on human heart sections, Cao and co-workers tried to spatially localize regions of altered innervation, and they demonstrated that post-MI remodeling seems to be characterized by regional hyperinnervation in the perivascular sites or in the periphery of injured myocardium and regional denervation in the regions with necrosis or dense fibrosis [107]. This study, however, was performed on 2D sections, thus a few years later Yokoyama *et al.* [42] tried to expand the investigation by analyzing the 3D SNS structure in entire infarcted mouse hearts (*Figure 16*). The results of the study showed a trend of sympathetic fibers denervation distal from the site of infarction and nerve sprouting at the ischemic border zone at 2 weeks following MI, even though they did not achieve a proper image resolution to detect thin neuronal processes. More recently, in 2022 Zhu and colleagues further investigated the 3D-SNS remodeling that occurs in mouse hearts after a MI, finding regional patterns of altered electrical conduction aligned directly with altered neuroeffector junction distribution [43].

However, even though highly indicative, the use of a mouse model is not suitable for the investigation of cardiac diseases since they do not resemble the anatomy of the human heart as effectively as large animal models. Up to date, we can state

that a complete view of the structural outcomes of the sympathetic neural network remodeling that follows a MI still remains missing, essentially due to methodological restrictions.

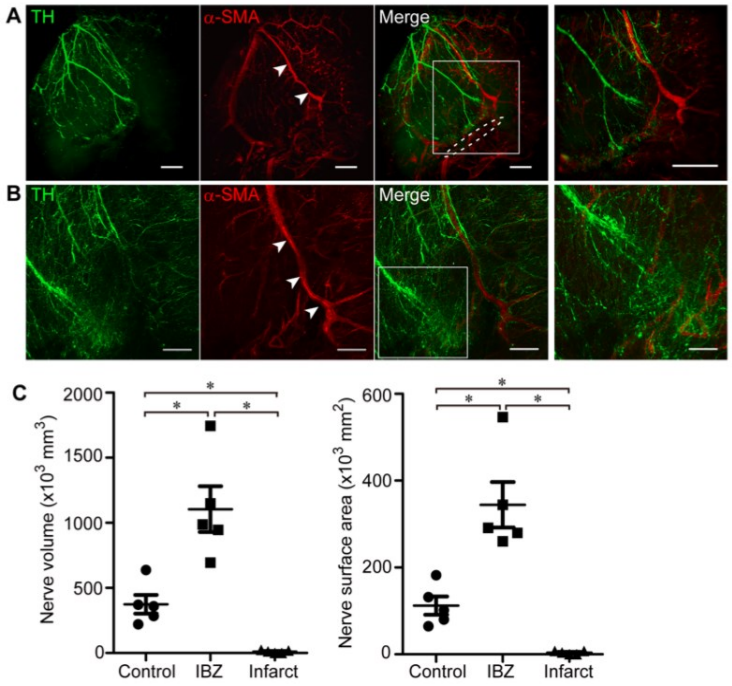

Figure 16: 3D) imaging of sympathetic nerves and coronary vessels in the post-MI mouse heart. A) 3D image of the heart 2 weeks after inducing MI. Tyrosine hydroxylase (green) and α-smooth muscle actin are used to stain heart tissue samples (red). The sympathetic nerves at the location of the ligation are abruptly decreased. The left anterior descending coronary artery is indicated with arrowheads. The ligation location is indicated by the dashed line. The boxed area in the left panel is seen in greater detail in the right panel. **B)** A 3D picture of the post-MI heart's ischemia BZ. The boxed area in the left panel is seen in greater detail in the right panel. Numerous tiny nerve fibers are dispersed widely in the ischemic BZ immediately surrounding the site of ligation. **C)** Sympathetic nerve examinations in post-MI mice. In post-MI hearts, the nerve volume and surface area are considerably higher in the ischemia border zone and lower in the infarct area (n = 5, *p<0.05, Steel-Dwass test). The error bars show the standard deviation from the mean. Image taken from [113].

2.5 Rationale of the study

The structural outcomes of the remodeling process that occurs in the heart after an episode of MI are critical in determining whether the heart will be inclined to experience malignant arrhythmias over the years. In this scenario, recently an increasing interest among the scientific community has been devoted to comprehending the nature of the remodeling that occurs to the cardiac sympathetic network, which has been found to correlate to PVCs.

Nowadays, conflicting information exists regarding the nature and the extent of the SNS remodeling within cardiac scar in post-MI hearts. Some studies [31] showed evidence that the cardiac infarct was not reinnervated after the infarction [104], whereas different studies stated the presence of robust sympathetic regeneration within the infarct after chronic cardiac ischemia [105,111,114]. Additionally, further evidence has been provided that sympathetic hyperinnervation and denervation are likely to coexist in the heart post-infarction in a region-specific manner [94,98,99].

The common hypothesis among all the studies is that understanding the occurrence of the cardiac SNS remodeling after MI is crucial since it is a key factor for the developing of ventricular arrhythmias both in animal models [110] and in humans [115–117].

Nonetheless, up to date methodological issues have restrained the investigation of the SNS in the heart, limiting most of the studies to small-size samples and 2D investigations. The drawback of studying 2D sections is the absence of 3D structural information that is needed to better comprehend disease progression. A further risk of missing or misinterpreting illness queues depends on the limited sample nature of studying sparse 2D sections [118].

Therefore, 3D information is required for reliable analyses and to visualize the structural organization of post-MI scar and BZ regions. Recently, important steps have been done in this direction and some studies have provided 3D reconstructions of the cardiac SNS remodeling that occurs in infarcted mouse models. However, even though highly relevant, studies based on mouse models are less informative since they significantly differ from human conditions.

Based on this gap of information, the aim of this PhD study was to develop a comprehensive methodological framework to permit 3D investigations in massive human-resembling cardiac tissues at high-resolution. We performed a proof of principle investigation to three-dimensionally reconstruct the sympathetic neuronal network remodeling occurring in the infarct BZ in post-MI hearts. Moreover, following the discoveries provided by Amoni *et al.*[89] regarding the presence of discrete vulnerable areas within the BZ from which arrhythmias initiate, together with the capability of identifying these areas *in vivo*, we decided to focus our investigation not only on the study of the structural outcomes of the BZ remodeling, but also to discriminate between arrhythmias initiating and not initiating sites (respectively, PVC and NO-PVC sites).

For the study, we exploited a swine model, which is a pivotal model for clinical research on cardiac conditions. Indeed, swine models are the most accurate animal models to study heart problems due to the structural, electrical, and metabolic similarities of their heart to the human heart in many aspects [119] and they are widely used in cardiovascular research.

However, studying cm-scale biological samples at micrometric resolution in 3D has always been challenging since light absorption and scattering are additional limiting factors in thick samples, due to refractive index mismatch.

For this reason, it has been necessary to optimize a proper methodological protocol to enable the reduction of light scattering in cardiac samples as well as a homogenous labeling of the sympathetic nervous system within the specimen, ultimately allowing massive 3D reconstructions through optical fluorescence microscopy.

3. MATERIALS AND METHODS

3.1 Optimization of the optical clearing and staining protocols in entire mouse hearts

As a first step, to assess the best optical clearing protocol to be performed on the cardiac tissue, we exploited the mouse heart as an animal model.

3.1.1 Mouse model

Adult male C57-BL6J mice were used for the experiments. All animal procedures performed conform to the guide-lines from Directive 2010/63/EU of the European Parliament on the protection of animals used for scientific purposes; experimental protocol was approved by the Italian Ministry of Health on July 6, 2015; Authorization No. 944/2018-PR. All the animals were provided by ENVIGO, Italy.

3.1.2 Heart isolation and perfusion

The animals were deeply anesthetized with 2 mL of 3% Isoflurane and the heart was quickly isolated. To remove the blood from the vessels, the hearts were cannulated through the proximal aorta and perfused with 30 mL of phosphate-buffered saline (PBS) (pH 7.6) at a constant flow rate of 10 mL/minute. Subsequently, the hearts were perfused with 24mL of 4% paraformaldehyde in PBS (PFA 4%; pH 7.6). The specimens were then incubated in 30 mL of PFA 4% in PBS overnight (O/N) and the following day they were washed in PBS 3 times for 1 hour each.

3.1.3 uDISCO protocol

Four hearts were incubated in a total volume of 20 mL in increasing concentrations (30%, 50%, 70%, 80%, 90%, 96% and 100%) of tert-butanol in ddH2O in shaking at 37°C for 12 hours each. The specimens were then incubated at room temperature (RT) in BABB solution (benzyl alcohol: benzyl benzoate 1:2, respectively) and diphenyl ether (DPE) at 15:1 of BABB:DPE, for 3-6 hours.

3.1.4 CLARITY protocol

We performed the CLARITY protocol on fifteen mouse hearts, slightly modified for its application on cardiac tissue. The hearts were incubated in 30 mL of Hydrogel Solution *(4% Acrylamide, 0.05% Bis-acrylamide, 0.25% Initiator AV-*

044 in 0.01 M PBS) for 3 days at 4°C in gentle shaking. After 3 days, the samples were de-gassed using a drier (KNF Neuberger, N86KT.18) and the oxygen was replaced by nitrogen. To favor gel polymerization, the samples were kept at 37°C for 3 hours and then incubated in 30 mL of clearing solution (*200 mM Boric acid, 4% Sodium Dodecyl-Sulfate (SDS) in deionized water; pH 8.6*) at 37°C in shaking up to the complete clearing of the tissue.

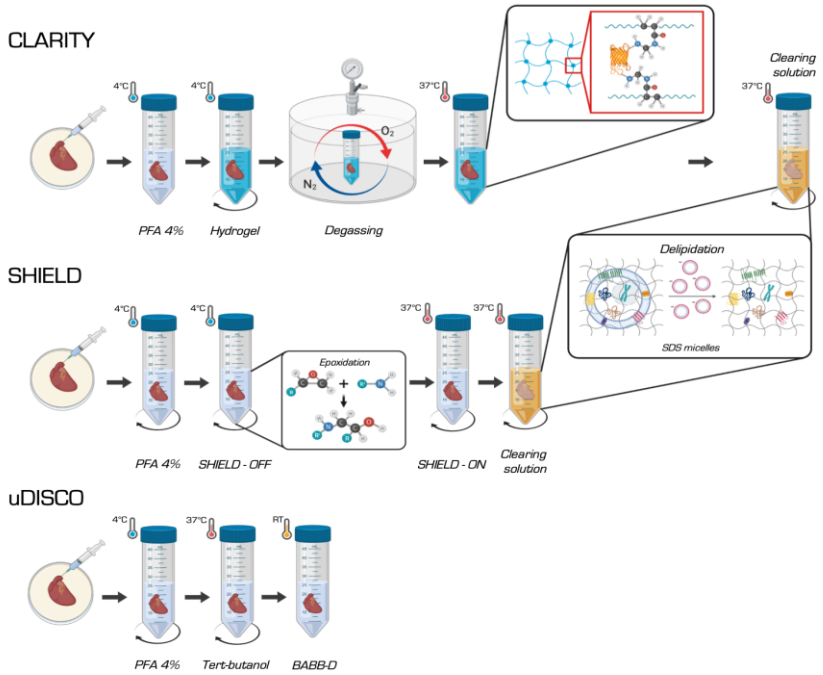

Figure 20: Schematic representation of the three investigated protocols (CLARITY, SHIELD, and uDISCO) for the clearing of entire hearts. Both CLARITY and SHIELD methodologies are based on tissue-transformation approaches and they both require a delipidation step. On the other hand, the uDISCO methodology is based on the simple RI homogeneisation after the removal of water molecules. Image created with Biorender. From [120].

3.1.5 SHIELD protocol

Twelve hearts were subjected to the SHIELD protocol. Similar to the CLARITY protocol, also the SHIELD one required some modifications for its application on the cardiac tissue. Hearts were incubated in 20 mL of SHIELD-OFF solution (*25% of ddH2O, 25% of LifeCanvas Technologies SHIELD Buffer solution, 50% of LifeCanvas Technologies SHIELD Epoxy solution*) at 4°C in shaking for 5

days. The following day the specimens were incubated in 20 mL of LifeCanvas Technologies SHIELD-ON solution at 37°C in shaking for 24 hours. The hearts were finally incubated in the SHIELD clearing solution (*Sodium Dodecyl Sulfate 300 mM, Boric acid 10 mM, Sodium sulfite 100 mM; pH 9*) at 37°C in shaking up to the achievement of a good level of transparency.

3.1.6 Whole mouse heart labeling of cellular membranes

CLARITY- and SHIELD-cleared samples were washed in warmed-up PBS for 24 hours at RT in shaking to remove the residual clearing solution, and then they were permeabilized in warmed-up PBS + 0.1% of Triton-X (PBS-T 0.1x) for 24 hours at RT in shaking. The hearts that had been cleared using the CLARITY protocol were incubated in 1:100 Wheat Germ Agglutinin (WGA) - Alexa Fluor 633 (ThermoFischer, W21404) in PBS-T 0.1x at RT in shaking for 5 days. The hearts were then washed in PBS-T 0.1x for 24 hours at RT in shaking; the specimens were then fixed in PFA 4% for 15 min and washed in PBS three times for 5 minutes each.

The SHIELD-cleared hearts were incubated in 1:100 WGA - Alexa Fluor 633 in PBS-T 1x (Triton-x 1%) at RT in shaking for 5 days. The samples were then washed in PBS-T 1x for 24 hours at RT in shaking, fixed in PFA 4% for 15 minutes and washed in PBS three times for 5 minutes each. To test the optimization of the WGA staining in SHIELD-cleared samples, several tests were performed. One heart was incubated in 1:100 WGA in PBS-T 1x for 10 days instead of 5 days; one heart was incubated in 1:100 WGA in PBS-T 1x for 10 days at 37°C instead of RT; one heart was cannulated again after the clearing and perfused with 1:100 WGA in PBS-T 1x and subsequently incubated in the same solution for 7 days at 37°C; one heart was incubated in 1:100 WGA in Hepes 1x for 7 days at 37°C; finally, one heart was incubated in 1:100 WGA in 500 mM NaCl for 7 days at 37°C.

3.1.7 CLARITY-cleared mouse ventricles labeling of cellular membranes and SNS

For the staining of the sympathetic innervation, we chose to tag the tyrosine hydroxylase, which is an enzyme involved in the biosynthesis of norepinephrine. CLARITY-cleared mouse ventricles were washed in warmed-up PBS for 24 hours in shaking and subsequently in warmed-up PBS-T 0.1x for 24 hours at RT in shaking. Heart tissues were then incubated in 1:200 of anti-Tyrosine

Hydroxylase (anti-TH; Millipore, Billerica, MA, USA, AB152) diluted in PBS-T 0.1x at 4°C for 3 days. The specimens were then incubated in 1:200 of the secondary antibody conjugated with Alexa Fluor 488 (Goat anti-rabbit, AB150077; Abcam) and 1:100 WGA - Alexa Fluor 594 (Thermo Fisher, W11262), diluted in PBS-T 0.1x for 2 days at RT. Finally, the samples were fixed in PFA 4% for 15 minutes and washed in PBS three times for 5 minutes.

3.1.8 Refractive index matching

CLARITY-cleared hearts and mouse ventricles were incubated in increasing concentrations of 2-2' Thiodiethanol [121] (TDE) in PBS: 20% TDE/PBS for 4 hours at RT in shaking, 47% TDE/PBS for 4 hours at RT in shaking and 68% TDE/PBS overnight (O/N) in shaking at RT. SHIELD-cleared hearts were incubated in 20 mL of EasyIndex (LifeCanvas Technologies) at RT for 3 days. Cautions have been taken to avoid hearts floating on the solution. uDISCO-cleared hearts were acquired in 15:1 of BABB:DPE.

3.2 Pig cardiac slices sampling, clearing and staining

3.2.1 Pig model

Three domestic pigs (Strain TN70, Topigs, Norsvin) of both sexes, named H1, H2 and H3 in this study, were used in the investigations. Treatment was in accordance with international guidelines (European Directive 2010/63/EU) and protocols were approved by the KU Leuven ethical committee (ECD137/2018). A myocardial infarction was created by 120 min balloon occlusion of the left anterior descending coronary artery followed by reperfusion. After 4 weeks, the animals were sacrificed and the sampling of specific sites was performed.

All in vivo studies were performed under general anesthesia and artificial ventilation at 6-10 ml/kg with 50% oxygen-air mixture. Sedation was performed with tiletamine/zolazepam 8 mg/kg and xylazine 2.5 mg/kg IM while anesthesia was induced with propofol 3 mg/kg and maintained with 10 mg/kg/h IV combined with remifentanil 0.2-0.4 µg/kg/h IV. Antibiotics (pre-operative cefazolin 22-50 mg/kg, IV and post-operative amoxicillin 15mg/kg or enrofloxacilin 4mg/kg, IM) and anticoagulation (acetylsalicylic acid, 500 mg and periodic heparin 5 000-10 000 IU, IV) were routinely administered.

3.2.2 Identification of discrete arrhythmia vulnerable and not vulnerable areas (PVC and NO-PVC sites)

3.2.2.1 cMRI imaging and personalized heart 3D printing

Cardiac magnetic resonance imaging (cMRI) was performed using a 3 Tesla whole-body scanner (PRISMA, Siemens, Erlangen, Germany) to acquire standard clinical stacks of vertical-, horizontal-, and short axis (SAX) images. The cMRI images were processed using a customized offline Matlab analysis program (RightVol). By contouring with cross-correlation in three imaging planes, the LV endocardium (including infarct), the septum, and the whole heart's epicardial surface were manually segmented (*Figure 21A*). A thresholding technique was used to autonomously segment the aorta from the surrounding tissue, while the papillary muscles were segmented from the SAX pictures (*Figure 21B*). Then, in MeVisLab (Bremen, Germany), these contours were converted into distinct 3D (*Figure 21C*). The planes and integration of these models were manually corrected where necessary after being verified for

anatomical accuracy and angulation faults. An *in vivo* fluoroscopic imaging was used to integrate the cMRI model. The image settings of both fluoroscopes were properly calibrated in accordance with previously established procedures in order to properly incorporate the preoperative CMR-derived 3D models into the intraoperative fluoroscopic configuration [122].

The casts were printed using a standard PLA material on a commercial 3D printer (Builder Extreme 1000 PRO, Noordwijkerhout, Netherlands. Using Ultimaker Cura (Utrecht, Netherlands), prints of the LV were examined for errors and adjusted as appropriate.

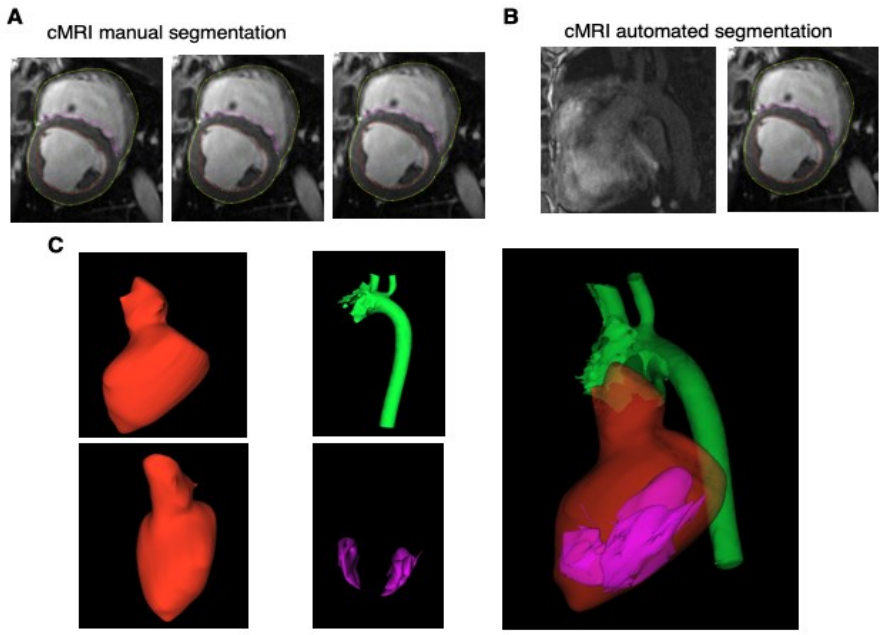

Figure 21: Cardiac magnetic resonance image segmentation and 3D model. **A)** Illustration of representative apical to basal short axis acquisition slices and superimposed manual segmentation of the LV endocardium (red), epicardial surface (yellow) and septum (purple). **B)** Illustration of the sagittal acquisition with a modified 5-chamber view used for automated thresholding to obtain models of the aorta (left); and the SAX slices thresholded to obtain and papillary muscle models. **C)** Left, corresponding models of the LV. Middle: corresponding model of the aorta (top) and papillary muscles (bottom). Right: final integrated models used for study.

3.2.2.2 Sacrifice and heart slices sampling

Animals were sedated before being sacrificed, and anesthesia was induced with pentobarbital (20 mg/kg pentobarbital, IV) while artificial breathing was being used. Heparin (5 000 IU) was supplied, the ascending aorta was cannulated with a cardioplegia needle and sheath, and the aorta was cross-clamped. 1L cold cardioplegia was then infused antegrade to arrest the heart in a relaxed state and prevent contracture. The heart was quickly harvested at the great vessels, and washed in cold cardioplegia. The great vessels were sutured and the heart refilled to volumes matching the MRI used to create the models and then the major vessels were sutured and sealed to preserve these volumes.

The identified sample sites were then taken, washed in PBS for 6 hours and fixed for 8 hours in 4% PFA.

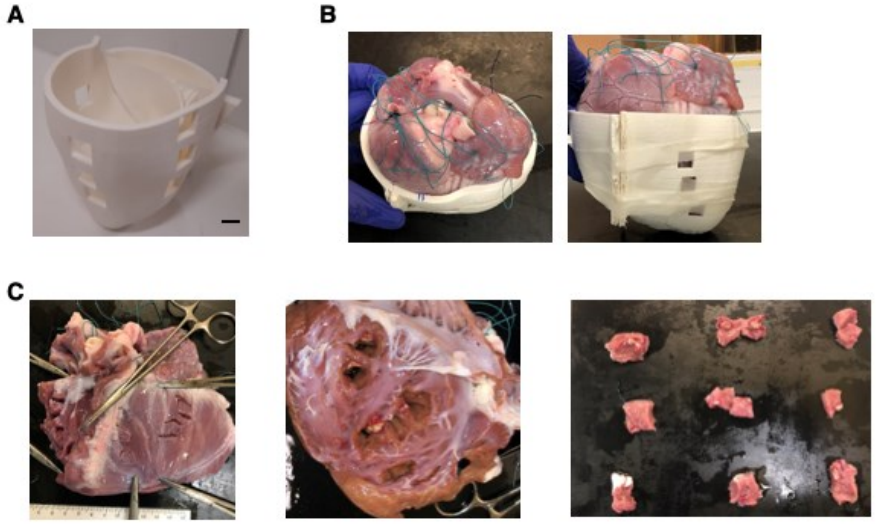

Figure 22: Accuracy of 3D print guided *ex vivo* sampling. A) The final printed 3D cast used for targeted sampling. **B)** Fitting of the LV into the cast. **C)** Epicardial view of the LV demonstrating site-directed sample sites (left), the endocardial side after sample resection (middle) and collection of the individual samples of the ablation lesions *en bloc*.

The cardiac sampled portions corresponding to remote, NO-PVC and PVC sites were then sliced in sections of 500 µm of thickness employing a vibratome. Figure 23 shows a representation of the portions that have been considered as

PVC sites (regions within the BZ where arrhythmias initiating events clusterized), BZ NO-PVC sites (portions isolated from the scar BZ that showed not to give rise to any arrhythmia) and remote sites (regions that are distant from the infarct).

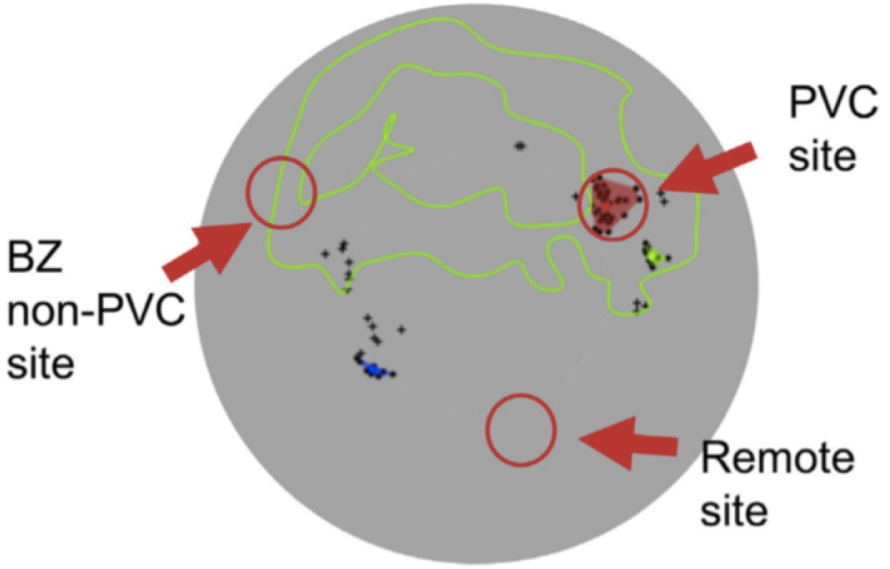

Figure 23: PVC, NO-PVC and remote sites sampling. The schematic represents the sites that have been considered as PVC sites (regions within the BZ where the arrhythmias initiating events clusterize), BZ NO-PVC sites (regions within the scar BZ that do not present arrhythmias initiating events) and remote sites (regions far from the scar). Image taken from [89].

3.2.3 CLARITY protocol on pig heart slices

One PVC and one NO-PVC slice isolated from each heart (H1, H2 and H3) and one remote site isolated from H1 and H2 were subjected to the CLARITY protocol (tot: PVC= 3 slices, NO-PVC= 3 slices, Remote= 2 slices). The selected slices were washed in PBS 0.1x at RT for 24 hours in gentle shaking. Then, the specimens were mounted in a custom-made chamber device using two cover glasses (UQG optics, 60x60 mm, UV fused silica), custom-made 500-µm-thick spacers (56x56 mm, provided by Microlaser, Sesto Fiorentino (FI), Italy) (*Figure 24*) and a bi-component glue (Twinsil speed, Picodent GmbH, Germany). This approach was used to avoid the axial tissue deformation that occurs to CLARITY-cleared samples when the hydrogel-related swelling occurs without any spatial confinement [118].

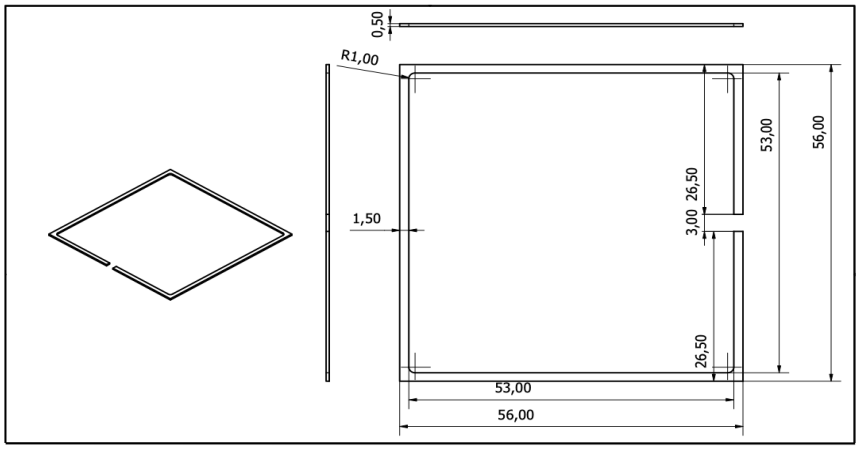

Figure 24: Custom-made 500 µm-thick spacer. The spacers were designed to be slightly smaller than the glasses while the thickness was designed to be the same as the samples. The small hole allowed us to fulfill the sandwich using a syringe.

Each sample was placed on a cover glass together with a spacer, carefully covered with a second glass to avoid the formation of bubbles and the chamber device was sealed with the bi-component glue. The sandwich was then filled with 1.5-2 mL of Hydrogel solution using a 1.0 mL syringe and a 0.45 mm needle, included from the spacer hole (*Figure 25A*). Finally, the device was placed in a vial, filled with Hydrogel solution to be completely covered and incubated for 3 days at 4°C in shaking. After 3 days, the samples were de-gassed using a drier (KNF Neuberger, N86KT.18) and the oxygen was replaced by nitrogen. To favor gel polymerization, the samples were kept at 37° C for 3 hours. Finally, they were carefully removed from the device and incubated in 30 mL of CLARITY clearing solution at 37° C in shaking up to complete clearing of the tissue.

3.2.4 Pig heart slices staining

CLARITY-cleared samples were washed in warmed-up PBS for 24 hours at room temperature (RT) in shaking and then in warmed-up PBS + 0.1% of Triton-X (PBS-T 0.1x) for 24 hours at RT in shaking. They were then incubated in 1:200 anti-tyrosine hydroxylase (anti-TH) (anti-TH; Millipore, Billerica, MA, USA, AB152) in PBS-T 0.1x at 4°C in shaking for 3 days. The samples were then washed in PBS-T 0.1x for 24 hours at RT in shaking and, the following day, incubated in 1:200 anti-rabbit Alexa Fluor 488 (Goat anti-rabbit, AB150077;

Abcam) and 1:100 Wheat Germ Agglutinin (WGA)- Alexa Fluor 594 (Thermo Fisher, W11262) in PBS-T 0.1x for 2 days at RT in shaking. The specimens were washed in PBS-T 0.1x for 24 hours at RT in shaking and, the following day, fixed in PFA 4% in PBS for 15 minutes and washed in PBS for 5 minutes three times. Finally, they were incubated in 5 mL of EasyIndex (Life Canvas Technologies) for 2 hours to favor the homogenization of the RI. We decided to use EasyIndex instead of 68% TDE/PBS in these samples in order to avoid tissue shrinkage during the 3-days long acquisitions.

3.2.5 Cleared pig heart slices mounting

The same chamber device described above was used to mount the samples for the imaging, but, in order to match the refractive index of the cleared-samples incubated in EasyIndex (RI= 1.465), a 500 µm-thick quartz glass (60x60 mm, provided by LaborChimica, Prato, Italy) has been used to replace the cover glass on the top (*Figure 25B*). It was then secured and held stable in a dish filled with a solution of 91% of glycerol in ddH2O, which presents the same RI of 1.465 but that is less expensive.

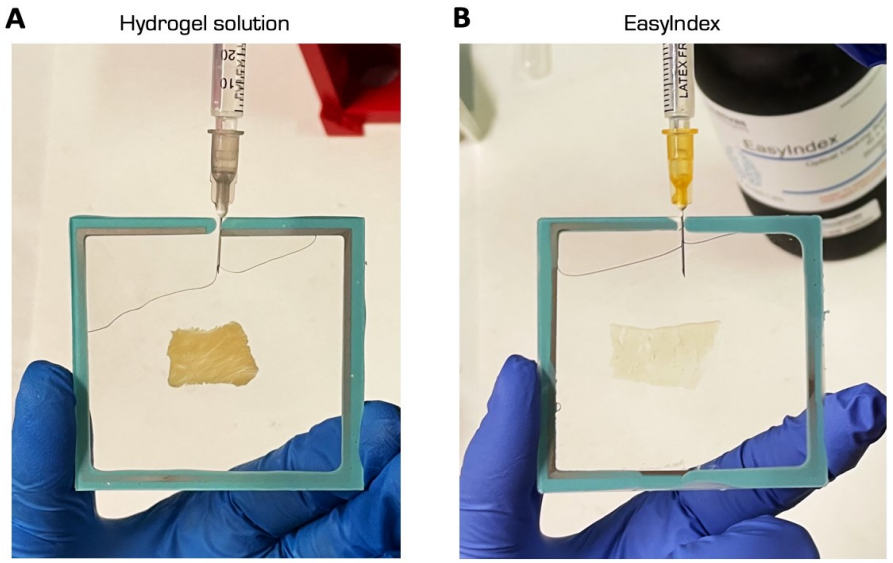

Figure 25: Custom-made chamber device to prevent CLARITY-induced tissue anisotropic deformation. Sample mounting in the custom-made chamber device before (**A**) and after the clearing (**B**), in Hydrogel solution and Easyindex, respectively.

3.3 MesoSPIM setup

For the mesoscopic reconstructions of the entire cleared hearts we used a custom-developed MesoSPIM microscope[123]. All the microscope components are automatically controlled by a dedicated software developed in LabView 2012 (National Instruments, version 12.0f3 at 32 bit). Figure 26 shows the MesoSPIM setup.

The microscope illuminates the cleared sample with an axially-scanned light sheet [124], operating at 638 nm. For the detection, we used a sCMOS camera (Orca Flash V3.0, Hamamatsu) operating at 500 ms of exposure time and a frame rate of 1.92 Hz. A 2x magnification objective (Thorlabs, TL2X-SAP) was used to acquire the entire Field of View (FoV) of 1.04 cm in a single scan. A long-pass filter (Thorlabs, FELH0650) placed after the objective was used to select the fluorescence signal. Tomographic reconstructions were performed using a Z-scan velocity of 6 μm/s, and assuming a frame rate of 1.92 Hz, one frame every 3.12 μm was acquired, oversampling the system Z-PSF by about two times.

During the acquisitions, the heart is placed in a quartz cuvette (Portmann Instruments, UQ-20°), filled with the refractive index medium (68% TDE/PBS for CLARITY-cleared hearts, EasyIndex for SHIELD-cleared hearts and 15:1 BABB-DPE for uDISCO-cleared hearts). The cuvette is mounted using magnets on the support which is equipped with two manual translators (Physik Instrumente) to allow the translation in XY, a motorized translator for movements along the Z-axis (Physik Instrumente, M-122.2DD), and a rotational translator (Physik Instrumente, M-116.DG), useful to rotate the sample around the Y-axis. The entire block can be moved downwards to immerse the quartz cuvette in a second larger quartz cuvette, filled with the proper refractive index matching medium.

3.3.1 Acquisition protocol

We noticed that SHIELD-cleared hearts tend to float once immersed in EasyIndex, due to the different specific weight. To overcome this limitation, the base of the hearts was glued to a metal support using a commercial glue (Super Attak Precision, Loctite), not to damage the ventricular tissue. All the differently cleared hearts were placed in the inner quartz cuvette, previously filled with the refractive index matching medium, which was subsequently immersed in the outer quartz cuvette, filled with the proper refractive index matching medium.

Tomographic reconstructions were obtained by moving the sample along the Z-axis at a constant speed of 6 µm/s thanks to the motorized translator. This mechanism, coupled with an image plane acquisition frequency of 2 Hz, guarantees a Z sampling of about 3.0 µm. The tomographic reconstruction will therefore have voxel sizes of 3.25 µm × 3.25 µm × 3.0 µm in XYZ, respectively. A laser power of 30 mW was routinely employed.

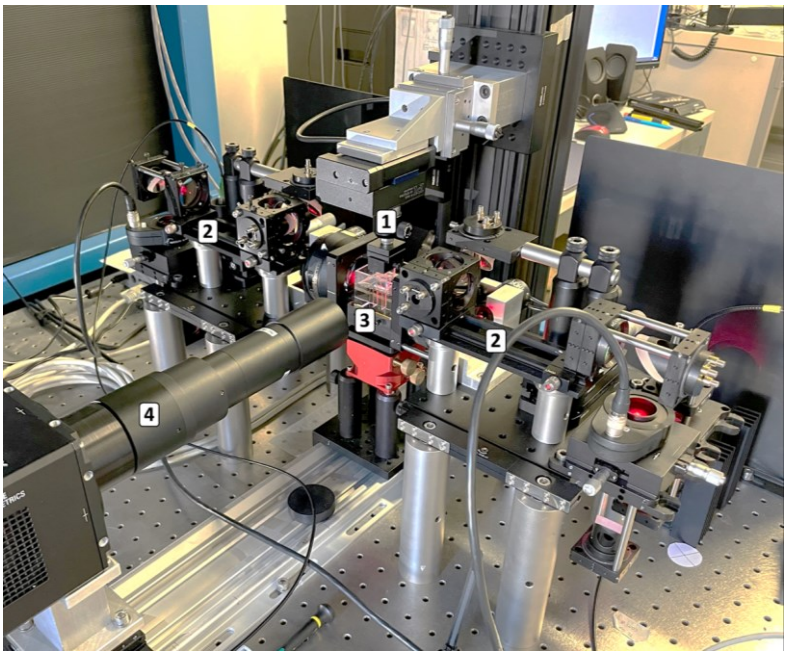

Figure 26: MesoSPIM setup. Numbers indicate the main components: **1)** holder for positioning the sample, inserted into the inner cuvette; **2)** excitation arms; **3)** outer cuvette; **4)** detection optics.

3.4 Two-photon fluorescence microscope

For the image acquisition of the cleared slices we used a custom-made two-photon fluorescence microscope (TPFM) equipped with a mode locked Chameleon titanium sapphire laser (120 fs pulse width, 80 MHz repetition rate; Coherent Inc.). The laser was operated at 780 nm and it was coupled with a custom-made scanning system supported with a pair of galvanometric mirrors (LSKGG4/M; Thorlabs, Newton, NJ, USA). A closed-loop xy stage (U-780 PILine xy Stage System; Physik Instrumente, Karlsruhe, Germany) allowed radial displacement of the specimens and a closed-loop piezoelectric stage (ND72Z2LAQ PIFOC objective scanning system, 2 mm travel range; Physik Instrumente) allowed shifting the objective along the Z-axis. Three independent GaAsP photomultiplier modules (H7422; Hamamatsu Photonics, Bridgewater Township, NJ, USA) acquired the fluorescent signal. The setup was equipped with dichroic mirrors with cut-off wavelengths of 705 nm, 552 nm and 484 nm. Band-pass emission filters centered at 530 ± 55 nm and 618 ± 50 nm were used, respectively, for Alexa-Fluor 488 and Alexa-Fluor 594 detection, and a filter centered at 390 ± 18 nm was used for second-harmonic generation (SHG) detection.

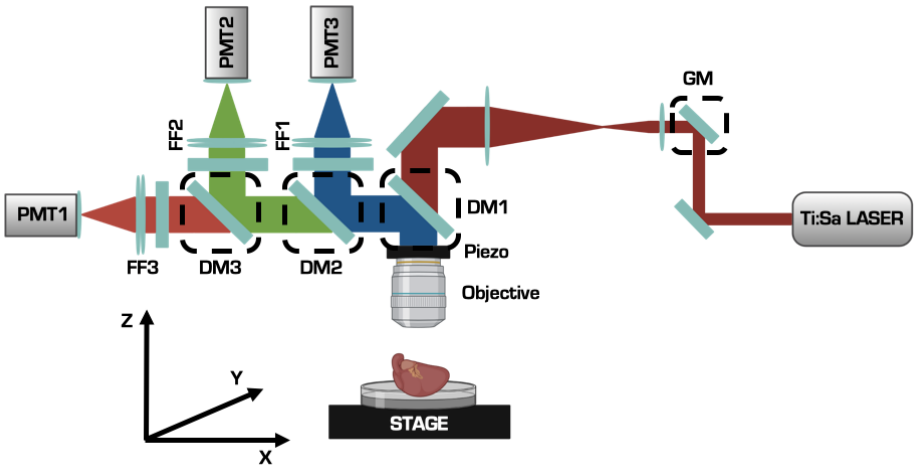

Figure 27: Schematic representation of the custom-made Two-Photon Fluorescent Microscope (TPFM). Objective; GM: galvanometric mirrors; DM: dichroic mirror; FF: fluorescence filters; PMT: photomultiplier; Piezo: piezo-electric; Stage: closed-loop stage.

3.4.1 Mouse ventricles acquisition

Cleared samples were carefully pinned on a Petri dish with a bottom layer of silicon, fulfilled with 68% TDE/PBS. For the mouse ventricles 3D reconstructions, single stack of 350 μm in depth were acquired both on the epicardial and the endocardial surfaces, using a refractive index tunable 25x objective lens (LD LCI Plan-Apochromat 25x/0.8 Imm Corr DIC M27; Carl Zeiss, Oberko- chen, Germany). The described system allowed the acquisition of stacks with a xy field of view (FoV) of 450 x 450 μm; sequential images have been acquired setting a Z-step of 2 μm.

3.4.2 Pig slices acquisition

The mounted sandwiches were placed and immobilized at the bottom of a Petri dish, subsequently filled with 91% Glycerol/water. The laser was focused on the specimens with a refractive index tunable 10 × objective (Nikon, CFI 10X G, Plan Apo A.N.0,5 WD 5,5mm, R.I. 1,33-1,51). The described system allowed the mosaic acquisition of the entire surface and thickness of the slices. Each acquired stack has a xy FoV of 1.2 × 1.2 mm and was acquired setting a Z-step of 5 μm. For the subsequent mosaic reconstruction, the serial Z-stacks of adjacent regions were acquired with a lateral overlap of 120 μm.

3.5 Image analyses

3.5.1 Image preprocessing

Vignetting is the reduction in brightness towards the image edges which is typically encountered in all optical systems, including two-photon fluorescence microscopes. Specifically, vignetting may lead to pronounced stitching artifacts when generating microscopy tiled reconstructions through the alignment of separately acquired adjacent z-stacks.

Vignetting correction methods generally stem from the assumption that the intensity of the single 2D slices composing z-stacks can be modeled via the following linear model: $I0(x,y) = I(x,y)v(x,y) + z(x,y)$, where $I0(x,y)$ represents the intensity of the acquired image; $v(x,y)$ and $z(x,y)$ respectively denote the spatial gain and additive terms of the imaging system; and $I(x,y)$ is the true fluorescence intensity to be retrieved. Since the $v(x,y)$ and $z(x,y)$ functions are wavelength-dependent, the illumination correction procedure must be individually applied to each color channel. Here, the vignetting correction was performed using the retrospective CIDRE (Corrected Intensity Distributions using Regularized Energy minimization) algorithm, which estimates the $v(x,y)$ and $z(x,y)$ terms at each wavelength of interest using a reference dataset of 2D single-channel images [125].

In the present work, a custom software was developed for generating wavelength-specific images from a set of high-quality multi-channel 3D stacks and, then, for applying the three sets of identified spatial models of intensity gain and offset to the three channels of the raw stacks to be corrected, iterating over their z-axis.

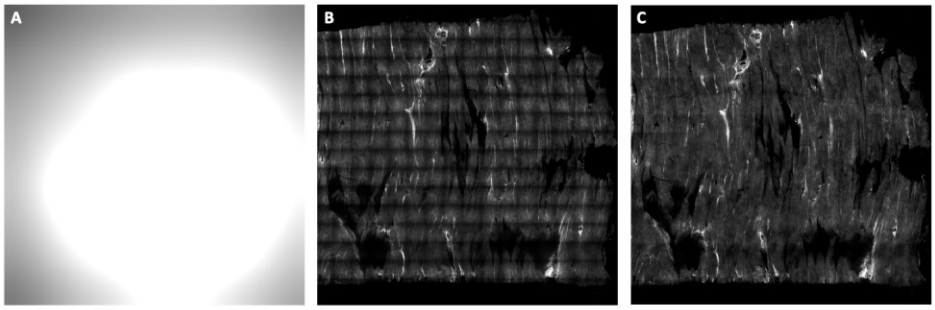

Figure 28: Application of CIDRE for vignetting correction. A) Spatial gain model v(x,y). **B)** Portion of a stitched mosaic of a remote site without the application of CIDRE. **C)** The same portion of mosaic stitched after the application of CIDRE.

The single-channel corrected z-stacks were then fused together to generate mosaic reconstructions using the Fusion plugin of the commercial Huygens software ([21.10.0p2 64b] (Scientific Volume Imaging, The Netherlands, http://svi.nl).

3.5.2 Estimation of the CLARITY-related samples swelling in XY

For each sample, we evaluated the CLARITY-related tissue swelling in the two dimensions (x,y) both in the myocardial region and in the scar region. To do that, we photographed the sample before and after the clearing procedure on a 1-mm graph paper sheet. For each sample, we estimated the expansion in X and Y by carefully measuring the length of the myocardial and the scar regions several times in different positions of the sample, before and after the clearing procedure. Since the lengths were found to be consistent among the measurements within the same axis, we calculated the average expansion coefficient both in X and Y, both in the myocardial and scar regions, in each sample. The corresponding X and Y expansion coefficients were applied to resize the mosaic reconstructions to their original dimensions before performing further analyses.

3.5.3 Estimation of myocardium and collagen percentage

To estimate the volume of myocardial and fibrotic tissue in the slices, we involved muscle autofluorescence and collagen channels, respectively. We first downsampled the resized mosaics to a pixel size of 280 μm in xy. For each frame, we applied Contrast Limited Adaptive Histogram Equalization (CLAHE) to equalize the contrast of the image and applied threshold-based segmentation using the AutoThreshold plugin of Fiji software [126], using the "mean" method to automatically estimate the threshold frame by frame. We calculated the volume of myocardium, fibrosis, and overlapping area (defined as the overlapping area between the two segmentations) by multiplying the number of voxels for the volume of each voxel (0.000392 mm^3). Finally, volume of myocardium, scar, and overlapping areas is re-scaled accordingly with the expansion factor previously estimated. The percentage of collagen is then calculated for each reconstruction as follow:

Collagen (%)= 100* Collagen Vol / (Collagen Vol + Myocardial Vol - overlap)

3.5.4 Cellular orientation analysis

To quantify the degree of cellular disarray in the myocardium, we developed an automatic software tool to estimate the 3D orientation of the WGA-labeled cardiomyocytes [127]. First, the WGA channel of each reconstruction is scaled in xy accordingly with the expansion factor of the myocardium. The software virtually sectioned the volume into 70-μm side portions and, in these subvolumes, applied a Structure Tensor Analysis (STA) to extract the main direction of the cells, storing all these orientations to generate a virtual cytoarchitecture of the entire slice represented as a map of versors. Then, the software estimated multiple local disarrays dividing the virtual architecture in macrovoxel of 210 μm (3x3x3 subvolumes), 280 μm (4x4x4) and 350 μm (5x5x5). Local disarray is defined as (1-Alignment) in percentage, where Alignment is the module of the average vector of local orientation versors inside the macrovoxel. Figure 31 shows the schematic representation of the software pipeline. Finally, three-dimensional local disarray maps were generated for each spatial resolution (210 μm, 280 μm, and 350 μm).

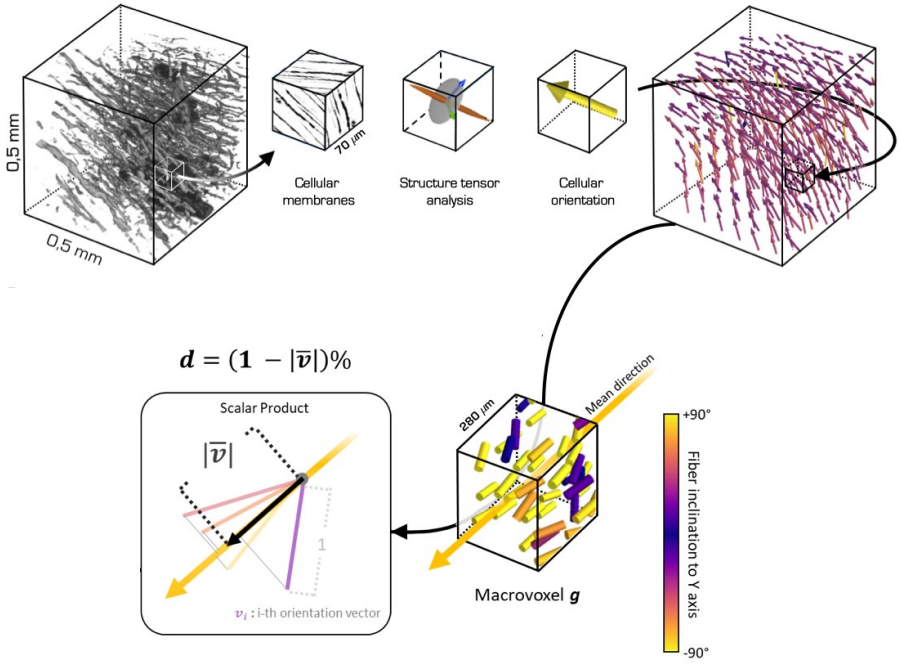

Figure 29: Representation of the software workflow in the cytoarchitecture reconstruction and disarray mapping. The volume is virtually dissected in subvolumes of 70 × 70 × 70 µm. The local fiber orientation is extracted for each portion using the FFT-based analysis. A vector space is used to collect and depict the whole cytoarchitecture. The color of a vector indicates how closely it is aligned with the primary axis of force production (Y). The findings are then smoothed and a 3D map of the cell misalignment is produced. Next, local cellular disarray is evaluated with a pre-defined resolution (in this case, 280 x 280 x 280 µm). Image modified from [127].

To ensure that the statistical analysis of cell orientation was confined only to the myocardial tissue and not in the scar area, overcoming the problem of collagen labeling by WGA, we masked cellular disarray maps using myocardial segmentation previously generated by muscle autofluorescence, rescaled to match the resolution of the disarray analysis (*Figure 30B*). The distribution of the disarray values in the masked maps were analyzed and plotted using Origin Pro. Moreover, the average variation coefficient (CV) of the two remote sites, three PVC and three NO-PVC sites at the three spatial resolution was evaluated.

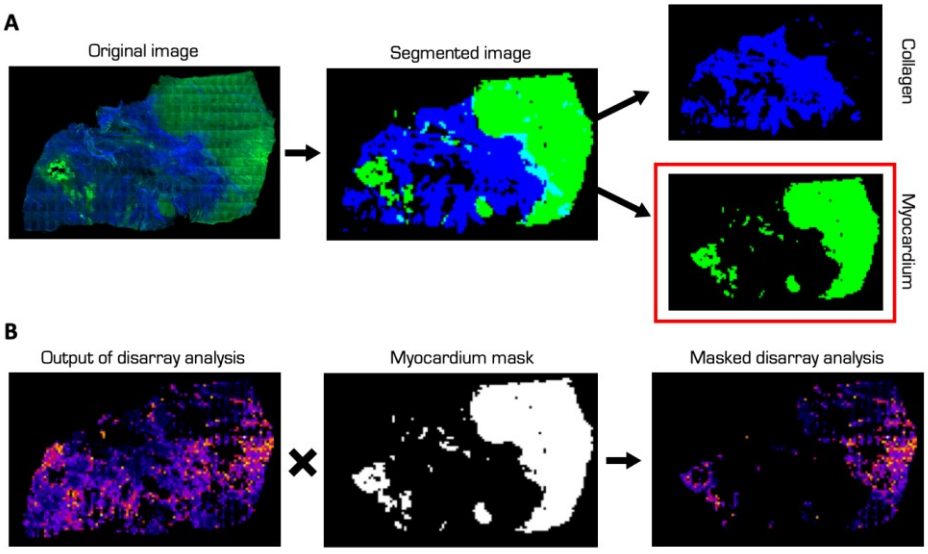

Figure 30: Autofluorescence masking of cellular disarray analysis. A) From the left, the original 3D reconstruction was projected in a single plane (MIP) and segmented to create masks of the collagen and the myocardium (for the latter, the autofluorescence signal of the tissue was used). **B)** The cellular disarray map, where the analyzed WGA signal comes both from the cellular membrane and from the collagen, was masked using the autofluorescence segmentation, in order to maintain only the values coming from the myocardium and discard the ones coming from the collagen-binded WGA. On the right, the result of the myocardium-masked analysis.

3.5.5 Analysis of the sympathetic innervation

The sympathetic innervation was analyzed in terms of density of neuronal processes and local coherency of their orientations. In detail, we developed an automatic pipeline to detect neuronal filaments in the high resolution tiles, measure local density and coherency (defined as the degree of local co-alignment) and to reconstruct the 3D map of these structural parameters of the entire slices. In order to better estimate the separation between myocardium and scar regions, we divided each mosaic reconstruction into 4 different z-sections of 150 μm each. For each tile, Anti-TOH channel was extracted and the background signal was removed by applying to each frame the "*Subtract background"* plugin of Fiji, implementing a rolling-ball filter with $\sigma = 10$ pixel. Noise was removed by applying two 3D filters, a median and a gaussian blur, both with a small kernel of $\sigma = 1$ pixel to prevent the loss of thin filaments. For each sub-slice, we squeezed the signal by means of a maximum Intensity profile (MIP) along the z-axis to identify neuronal filaments through an optimized 2D segmentation procedure based on a neural network. Then, we used the Trainable Weka Segmentation plugin available in Fiji. At first, we manually segmented all neurofilaments from the background in 30 representative MIPs, randomly selected at different depths from all the reconstructed pig cardiac slices. Later, a FastRandomForest model was trained on the resulting training set, thus generating a "cross-slices" model able to assign to each pixel of the MIP a probability $p \in [0, 1]$ to be classified as neurofilaments. The classification model was applied to all the MIPs previously generated for each tile, generating a reliable map of neurofilaments in each subvolume of the sample. Figure 33 summarizes the automatic detection software of neurofilaments.

Neuronal density was calculated by averaging the probability value in each tile. We then exploited the estimated expansion coefficients of each sample to scale the results accordingly. Neuronal coherency was calculated by applying the plugin "OrientationJ Measure" of Fiji, that performs a structure tensor analysis of the image and evaluates the coherency of the neurofilaments organization around their mean direction (coherency ranges from zero to one with random or perfectly aligned filament organization, respectively).

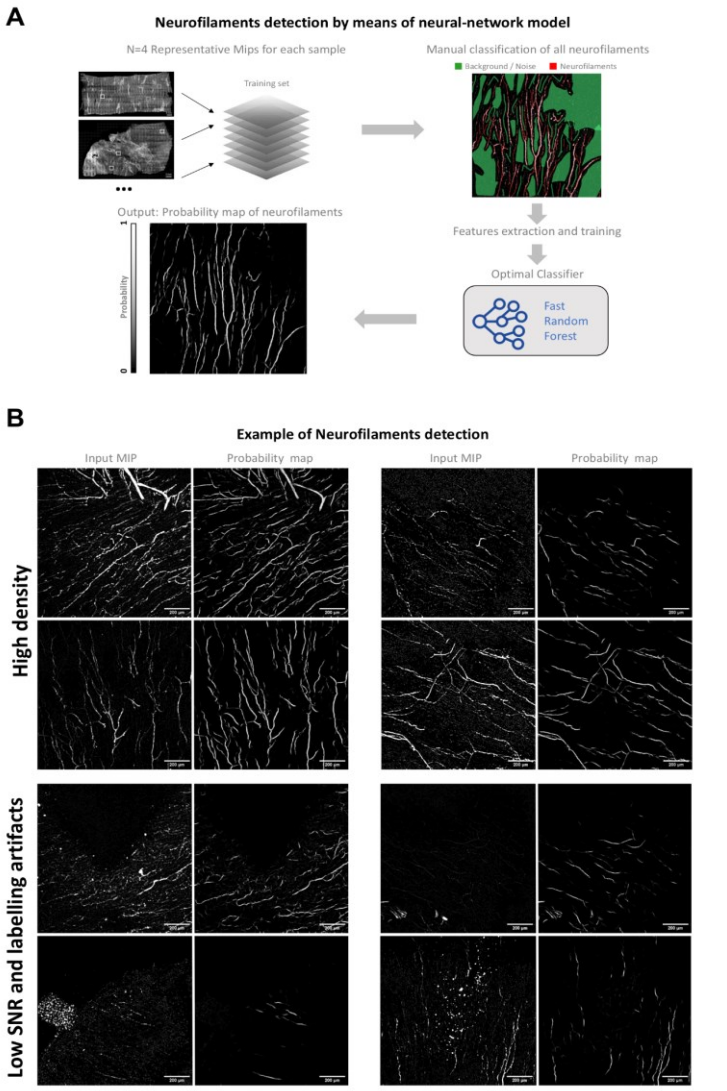

Figure 31: Neurofilament detection software tool. A) Thirty tiles were randomly selected among all the reconstructions and used as a training set. Neurofilaments and background were manually classified and exploited to train the software in discriminating the neuronal network and discarding the background noise. **B)** Examples of neurofilament detection using the developed software tool. The software is able to detect the neurofilaments both in tiles with a high density and in tiles with a poor signal-to-noise ratio (SNR), as well as in those presenting artifacts.

The resulting probability and coherency values were remapped into matrices, where each element spatially correlated to the corresponding tile of the mosaic. In order to avoid artifacts, we manually checked all the generated MIPs and those where the machine-learning based software had enhanced the noisy background signal were discarded from the analyses. The tiles corresponding to the borders of the sample were discarded as well to maintain only those in which the sample was included in the whole FoV.
To discriminate between myocardial and scar innervation, once again we exploited the autofluorescence and collagen masks. The masks were downsampled into 4 z-frames, each one of those corresponding to one of the 4 sub-sections that the reconstructions were divided into. The matrices masked with both the autofluorescence and collagen segmentations, to separate the density and coherency values corresponding to the myocardial innervation and the scar innervation.
The generated matrices were then converted into colorimetric maps via a Matlab script. The neuronal density and coherency values of the myocardial and scar regions of each tile were plotted using Origin Pro. We calculated the mean innervation density values of the myocardial and scar regions in each sample. In order to balance the impact of the actual amount of neurofilaments in the local coherency estimation, we calculated the average value of density-weighted neuronal coherency and its density-weighted standard deviation.

3.5.6 Statistical analysis

To perform the statistical analysis, we performed the Paired-t-test using the Prism GraphPad software.

4. RESULTS

4.1 Optimization of a protocol for the clearing of cardiac tissue

In order to perform massive 3D reconstructions of centimeter-sized slices, first of all we had to optimize a suitable clearing protocol for cardiac tissues. Indeed, all the tissue clearing protocols described above have been initially developed and applied in neuroscience, to successfully image and study the brain [48]. Heart tissue, however, differs from cerebral tissue in a number of ways, such as the large content of myoglobin that considerably intensifies tissue pigmentation and optical absorption in the visible wavelength range [128]. Therefore, the application of the original protocols does not perform as efficiently on cardiac tissue as on the brain; for this reason, up to date they have been mainly used for 3D investigations of small portions of the heart [129,130].

At this first stage of methodological optimization, we exploited the use of mouse hearts as an animal model. Since our goal was to obtain massive volumetric reconstructions, we mainly focused our attention on the two tissue transformation based methodologies (CLARITY [131] and SHIELD [132]) due to their performances in obtaining a high level of transparency, while comparing them to uDISCO [133] one of the most effective organic solvent-based techniques. We compared the methodologies mainly in terms of tissue features preservation, transparency and compatibility with a homogeneous staining across the sample [120].

4.1.1 Preservation of tissue features after clearing protocols

First of all, we assessed the performances of the three tissue clearing protocols in preserving the integrity of the tissue, maintaining its structure and conferring a high level of transparency to entire hearts. Figure 32A displays the degree of tissue preservation and transparency of the cleared hearts subjected to the three different protocols.

The highest level of transparency was obtained in CLARITY- and SHIELD-treated hearts while uDISCO conferred a medium-high level of transparency [120].

We also analyzed the changes in the volume of the organs before and after the application of the protocols. The final volume of the heart differed depending on the protocol used: uDISCO protocol reduced the volume of the heart due to the first step of tissue dehydration, whereas CLARITY expanded the tissue by

transforming the heart into a hydrogel-hybridized form. However, the subsequent incubation of CLARITY-cleared hearts in TDE for the RI matching led to the tissue shrinkage over time, to a size even smaller than the original one. On the other hand, the SHIELD technique did not alter the original size of the organ since it is not based neither on tissue dehydration nor hydrogel-hybridization.

We then evaluated the different timings that are required for the clearing of the whole organ using the different protocols, which are shown in Figure 32B. By using uDISCO protocol, only 5 days were necessary for obtaining an entire mouse heart transparent; this short timing is the most useful advantage of the protocol in respect to tissue transformation ones, which overall required between 3 (SHIELD) and 5 months (CLARITY).

With the uDISCO protocol, the transparency of the sample was achieved after a few hours of immersion in BABB-D, the same solution used as imaging medium, which presents a RI of 1.52. When using the CLARITY methodology, the transparency was obtained during the incubation in the clearing solution; therefore, the sample has to be maintained in this solution as long as it appears completely transparent. The following incubation in the refractive index medium (TDE 68% in PBS, RI= 1.46) enhanced even more the level of transparency of the sample. On the other hand, SHIELD-cleared hearts must be removed from the clearing solution before the achievement of total transparency, when the incubation in the solution does not confer any further improvement in tissue delipidation. Indeed, the ultimate transparency will be achieved by incubating the sample in the RI matching medium (EasyIndex, RI= 1.46).

Furthermore, the uDISCO methodology resulted in fiber delamination in the cardiac tissue (*Figure 33*), thus altering the tissue structure. On the contrary, the tissue structure in CLARITY- and SHIELD-cleared hearts was completely maintained and optimally preserved. However, it is noteworthy that CLARITY-cleared hearts became gelatinous and, as a result, handling the specimen was more challenging and required increased care. On the contrary, SHIELD-cleared hearts kept their consistency without any tissue alteration.

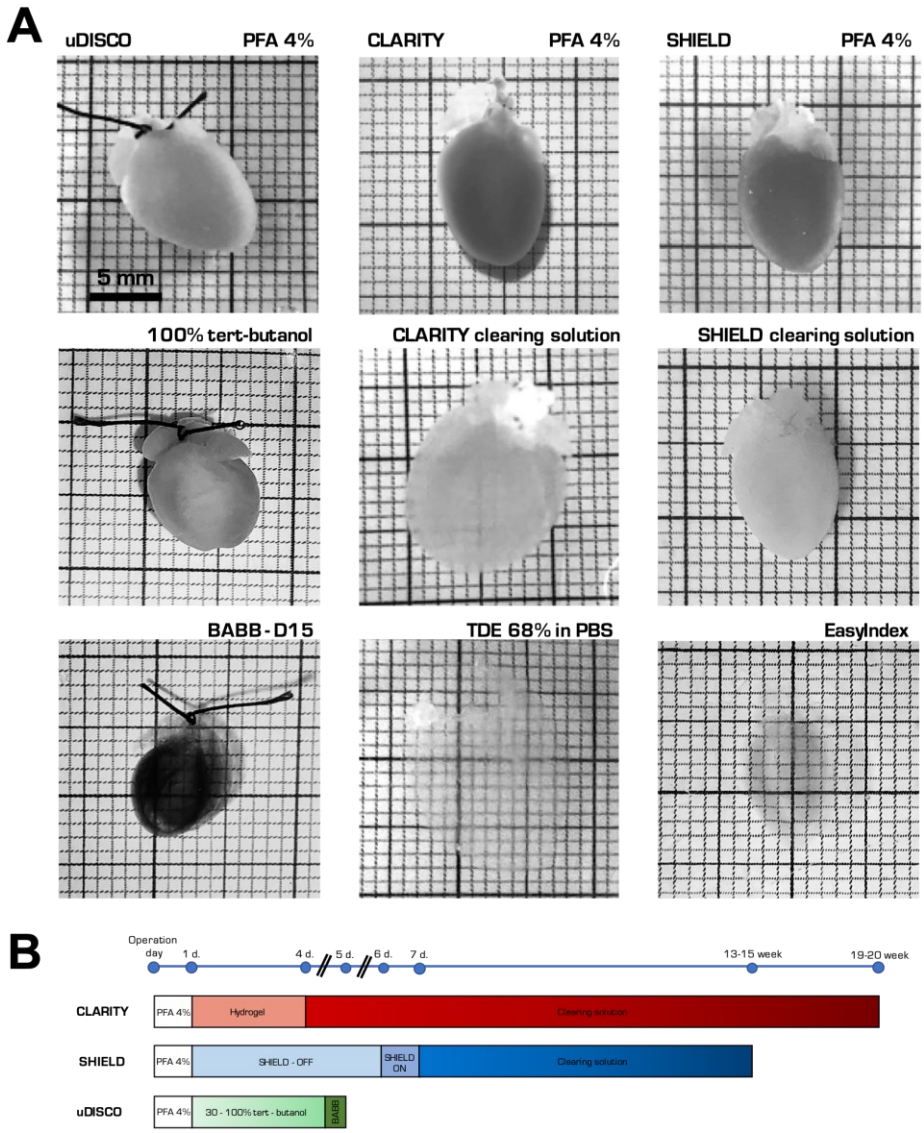

Figure 32: Results of the three clearing procedures performed on isolated mouse hearts. A) Transparency levels achieved after implementing the three different protocols. **B)** Required timings for the clearing of a heart exploiting the three methodologies (5 days. 3 months and 5 months for uDISCO, CLARITY and SHIELD, respectively) [120].

Then, we assessed the preservation of the tissue over time. We found out that the heart can be kept in BABB-D solution using the uDISCO technique for several weeks without affecting the organ preservation. CLARITY-cleared hearts can be maintained in clearing solution for months or stored in PBS after the clearing without losing their features but, once incubated in TDE, the imaging has to be performed as soon as possible before they begin to shrink. When placed in clearing solution for an excessive amount of time, SHIELD-cleared hearts suffer slight deterioration; nevertheless, when removed from the clearing solution at a proper time, they can be maintained in EasyIndex for several months without experiencing any structural change or harm.

Due to crucial procedures (e.g. the de-gassing step) that determine the quality of the outcome, the CLARITY protocol is the most difficult to be performed for the operator; in contrast, uDISCO and SHIELD resulted to be rather simple.

SHIELD is considerably expensive (about €1100 to clear 10 hearts), while the costs for the use of the CLARITY protocol are lower (about €650 to clear 10 hearts). Finally, uDISCO is the cheapest approach, costing only about €200 for the clearing of 10 hearts.

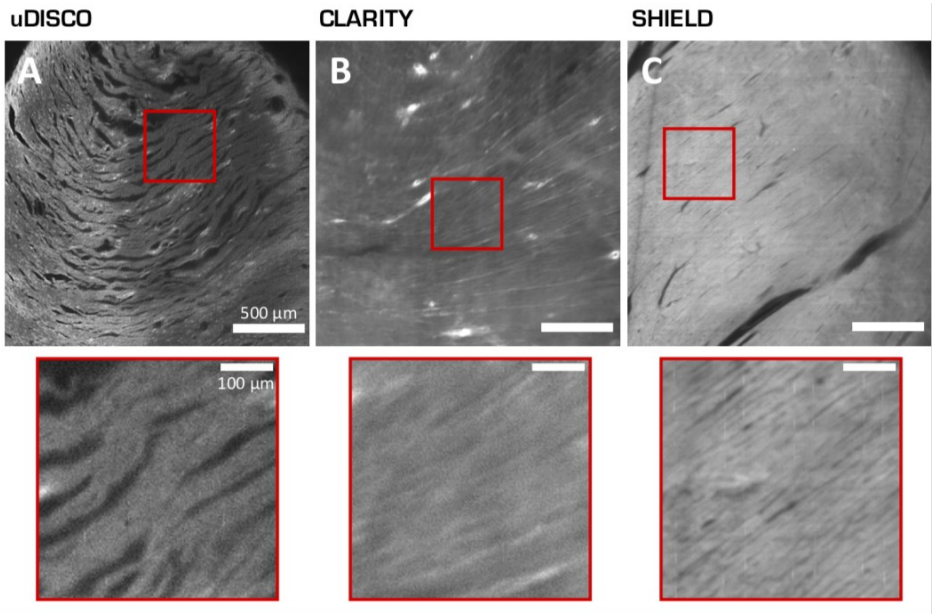

Figure 33: Tissue preservation and integrity of the hearts after the clearing protocols. Autofluorescence images performed with LSFM of the hearts cleared with uDISCO (**A**) CLARITY (**B**) and SHIELD (**C**) protocols. The scale bar represents 500 µm in the panels above and 100 µm in the ones below [120].

A summary of the key features of the tissue following the three treatments are listed in Table 1.

	uDISCO	CLARITY	SHIELD
Volume variation	Reduction	Expansion	None
Transparency	Medium - high	High	High
Tissue preservation	Low	Medium	High
Integrity over time	High	Medium	High
Clearing timing	5 days	5 months	2–3 months
Convenience	High	Medium - Low	High
Cost	Low	Medium	High

Table 1: Overview of the main tissue features of uDISCO-, CLARITY- and SHIELD-cleared hearts

4.1.2 Tissue labeling

We assumed that, due to the observed fiber delamination occurring in uDISCO-cleared hearts, tissue labeling would be misleading and not informative in any case. For this reason, we did not perform any staining protocol on these hearts.

Instead, we worked on the optimization of a staining approach to label cellular membranes in the hearts undergoing CLARITY and SHIELD clearing methodologies.

As a first test, we employed a small lectin with an extremely low molecular weight called Wheat-Germ Agglutinin (WGA), conjugated to a fluorescent dye (Alexa-Fluor 633), which labels cellular membranes.

Due to the advantages that the SHIELD procedure has demonstrated in maintaining the tissue features and due to the shorter clearing timings with respect to the CLARITY protocol, we started to optimize a staining procedure for SHIELD-cleared hearts, in order to achieve whole-organ uniform labeling.

At first, we tried a standard staining protocol, incubating the organ in 1:100 WGA - Alexa Fluor 633 in PBS-T 1x at RT in shaking for 5 days. By using these incubation parameters, the labeling of the organ did not succeed. Figure 34 shows an image of the SHIELD-treated heart acquired with our MesoSPIM setup; it can be appreciated that the penetration of the WGA is very poor and that the dye has remained stuck on the surface layers.

Thus, we tested several optimizations of the staining protocol in SHIELD-cleared hearts.

In particular, we tried to increase the staining timings up to 10 days (Figure 35A) while maintaining the same buffer solution (PBS-T 1x) and temperature conditions (RT). However, this optimization did not provide any improvement in the staining outcome.

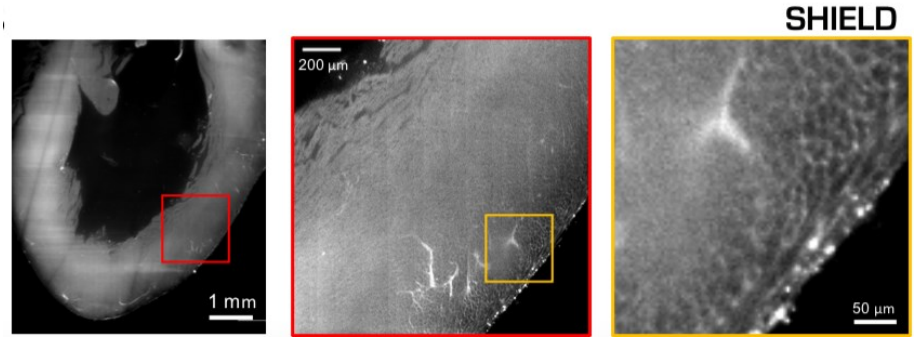

Figure 34: Light-sheet images of a SHIELD-cleared WGA-stained heart. A frame of a SHIELD-cleared heart, labeled with WGA- Alexa Fluor 633 and acquired with a custom-made LSFM with excitation light at 638 nm and a pixel size of 3.5 µm. Scale bars represent 1 mm (left), 200 µm (middle) and 50 µm (right).

We then tried to combine the increase of the incubation timing (10 days) with an increase of the temperature, maintaining the hearts at 37°C instead of 21°C. Despite a slight increase in the dye penetration, the result was still considerably inadequate, as we can see in Figure 35B.

As a further test, we decided to cannulate the heart from the aorta again after the clearing step and perfuse the heart with 1.5 mL of 1:100 WGA in PBS-T 1x. After the perfusion, we decannulated the heart and it was incubated for an additional 7 days in the same solution containing the dye at 37°C. Figure 35C shows the result of this test, with the WGA still remaining stuck in the surface layers of the organ.

At this point, we started to employ different buffers that present different chemical properties. Due to its extensive use in staining protocols, we exploited the incubation of the sample in 1:100 WGA in Hepes 1x for 7 days at 37°C. One more time, the dye penetration was extremely poor, as shown in Figure 35D.

Finally, as a last test, we decided to try the addition of 500 mM of NaCl to the buffer solution, since in literature it has shown to increase the penetration of the dyes [134]. The heart was incubated in 1:100 of WGA in 500 mM NaCl in ddH2O for 7 days at 37°C. Among all the tested approaches, this last one showed the best result in terms of the dye penetration in depth, as we can see in figure 35E.

Nonetheless, the staining effectiveness was not enough for providing a homogenous labeling of the whole volume of the organ.

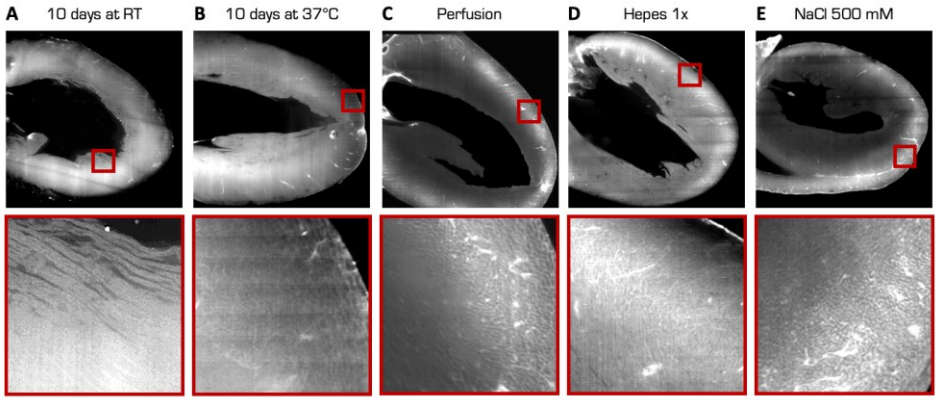

Figure 35: SHIELD-cleared hearts stained with WGA in different incubation conditions. A) SHIELD-cleared heart incubated in 1:100 WGA in PBS-T 1x at RT for 10 days. **B)** SHIELD-cleared heart incubated in 1:100 WGA in PBS-T 1x at 37°C for 10 days. **C)** SHIELD-cleared heart perfused with 1.5 mL of 1:100 WGA in PBS-T 1x from aorta and incubated in the same solution at 37°C for 7 days. **D)** SHIELD-cleared heart incubated in 1:100 WGA in Hepes 1x for 7 days at 37°C. **E)** SHIELD-cleared heart incubated in 1:100 of WGA in 500 mM NaCl in ddH2O for 7 days at 37°C. Images were acquired with a custom-made LSFM with excitation light at 638 nm and a pixel size of 3.5 µm.

Thus, we moved on and we tried to optimize a staining procedure for CLARITY-cleared hearts. This time, by simply incubating the organ in 1:100 WGA - Alexa Fluor 633 in PBS-T 1x at RT in shaking for 5 days we were able to homogeneously stain the cellular membranes across the entire heart volume, as it can be appreciated in Figure 36.

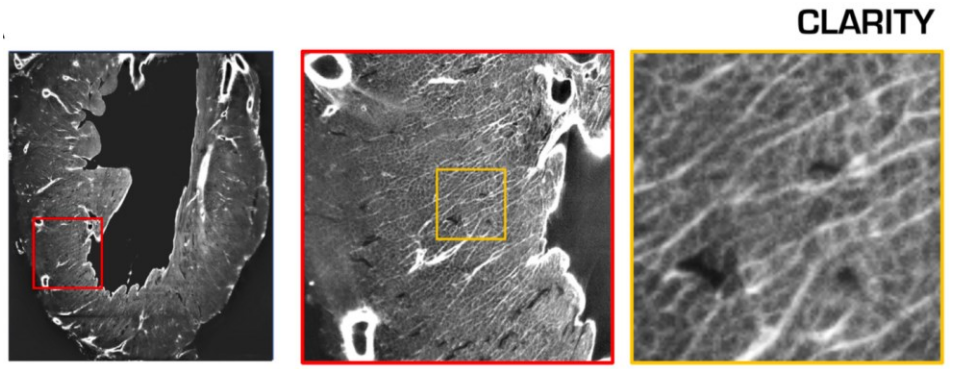

Figure 36: Light-sheet images of a CLARITY-cleared WGA-stained heart. A frame of a CLARITY-cleared heart, labeled with WGA- Alexa Fluor 633 and acquired with a custom-made LSFM with excitation light at 638 nm and a pixel size of 3.5 µm. Scale bars represent 1 mm (left), 200 µm (middle) and 50 µm (right).

Based on the results obtained testing the clearing protocols, we decided to employ the CLARITY methodology for the next steps of the study, to optically clear swine cardiac samples. Indeed, both CLARITY and SHIELD showed the ability to confer an optimal level of transparency and tissue features preservation to the hearts; however, when coming to the staining step, despite testing several optimizations of the protocol, the penetration of the small WGA dye remained poor in SHIELD-cleared hearts, thus leading to the conclusion that immunohistochemistry protocols are not feasible to any extent after the SHIELD protocol, due to the significantly higher molecular weight of the probes. On the other hand, CLARITY-cleared hearts were homogeneously labeled across the whole volume of the organ.

4.2 Optimization of a protocol for the staining of SNS, cellular membranes and collagen

Before performing the protocol on pig slices, we encountered the necessity of optimizing an immuno-staining protocol to fluorescently label the SNS and obtain CLARITY-cleared specimens homogeneously labeled across the entire volume. Due to the long clearing times that are proportionally dependent on the surface and the volume of the samples, we decided to limit the study to the left ventricles of control mice, thus also reducing the amount of antibodies needed while maintaining the entire thickness of the tissue required to properly assess the protocol performance in terms of staining capabilities in depth.

At this point, our goal was to obtain a uniform staining of the SNS in our specimens, but, in order to better comprehend their anatomical structure, we decided to integrate it in a triple staining procedure, entailing the already optimized protocol for the labeling of cellular membranes in CLARITY-cleared samples (using WGA) and the collagen detection.

The optimization of the staining procedure required to test several parameters, e.g. different anti-tyrosine hydroxylase antibodies, different concentrations (from 1:100 to 1:1000 antibody:buffer), different buffers (PBS, PBS-T 0.1x, PBS-T 1x, NaCl 500 mM, Hepes 1x), different temperatures (4°C, 21°C and 37°C) and different incubation timings (from 24 hours to 5 days), both for primary and secondary antibodies. We also tested the possibility of incubating the WGA together with the primary or secondary antibody, in order to reduce the timings of the protocol. To increase the image resolution we exploited our custom-made two-photon fluorescent microscope (TPFM), thus also enabling us to detect the collagen through the second-harmonic generation (SHG) signal without requiring the use of a fluorescent probe.

After several tests, we found the most effective parameters to obtain a homogeneous labeling across the thickness of the samples. The protocol is extensively described in the methodological section 3.1.8.

Figure 37 shows three-colors images of the acquired mouse left ventricles exploiting the optimized protocol and our custom-made TPFM. Explicative 2D

images have been selected at different depths and they show that the labeling of the tissue components is homogenous throughout the whole thickness of the sample.

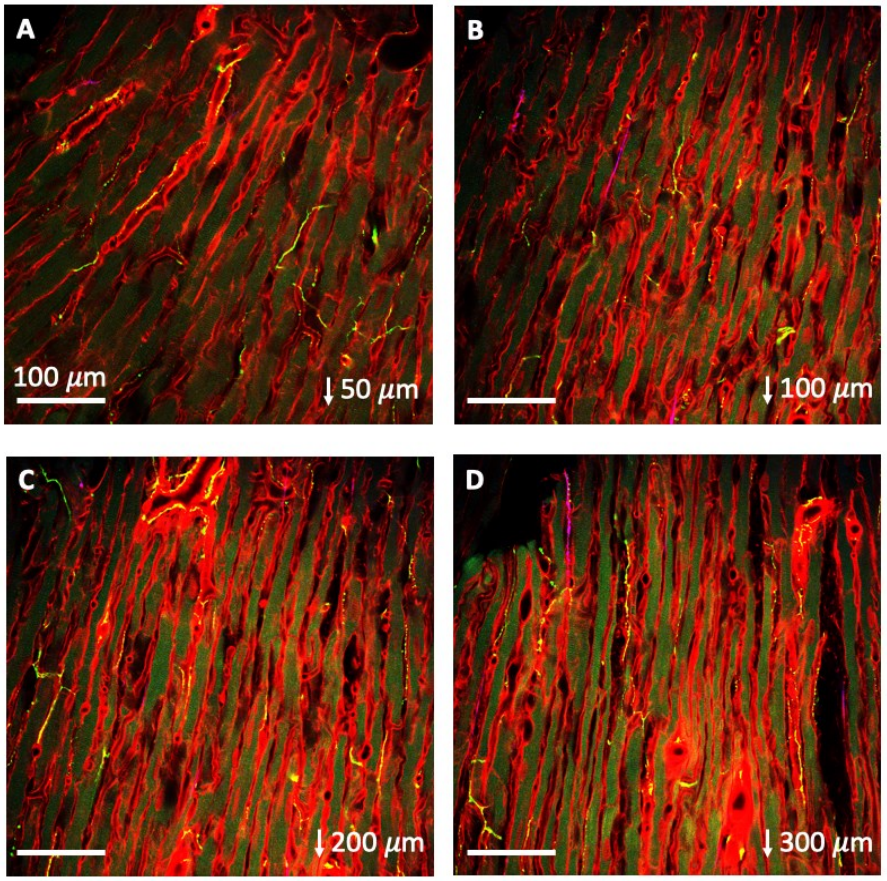

Figure 37: Sympathetic nervous system detection in CLARITY-cleared mouse ventricles. 2D frames of a CLARITY-cleared mouse ventricle at 50, 100, 200 and 300 µm in depth (**A**, **B**, **C** and **D**, respectively) labeled with WGA-Alexa Fluor 594 (red) and anti-TOH (green). The imaging was performed by using a custom-made TPFM with an excitation light at 780 nm and a pixel size of 0,439 µm. Collagen was detected by SHG (in blue, surrounding the endothelium of a few vessels).

Figure 38 (Panels A, B and C) shows maximum intensity projections (MIPs) of 50 micrometers of the SNS component at different depths, while Figure 38D

shows the MIP resulting from the projection of the entire volume on a single plane. Figure 38E shows a 3D rendering of the sympathetic neuronal network of the entire 350 micrometers-thick stack.

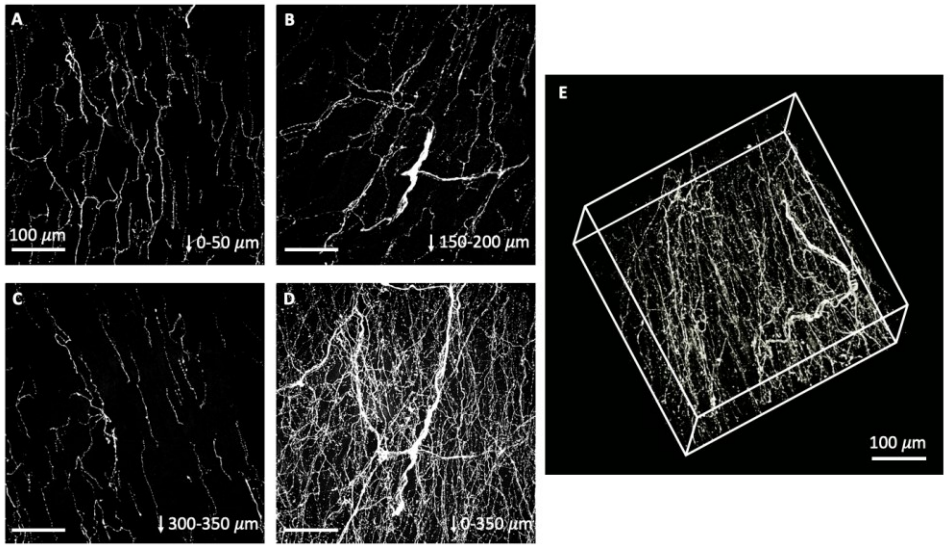

Figure 38: 3D reconstruction of sympathetic nervous system in mouse ventricle. 50 µm -thick maximum intensity projections (MIPs) of the anti-TOH detection channel at different depths (**A**, **B** and **C**). **D)** MIP of the entire 350 µm-thick stack. **E)** 3D rendering of the sympathetic fibers of an entire 350 µm-thick stack.

After several protocol optimizations, the clearing and staining results in large-size specimens appeared to be promising. At this point, we were confident in the robustness of the developed methodological framework. Thus, we moved on to the application of the protocol on pig heart slices isolated from remote, PVC and NO-PVC border zone sites.

4.3 Three-dimensional reconstruction of post-MI sympathetic nervous system remodeling in PVC and NO-PVC sites

The *ex vivo* identification of the precise sites where arrhythmias initiate *in vivo* has always been challenging. Even though some recently developed imaging systems allow the localization of these sites across the heart during *in vivo* investigations, tracking down these locations in the heart upon sacrifice is tough and predisposes to errors.

In Prof. Karin Sipido's laboratory in Leuven, Matthew Amoni and co-workers developed a useful pipeline to allow the precise identification and *ex vivo* sampling of discrete sites around the infarction BZ, which have been identified to be both arrhythmias initiating and not initiating sites (PVC and NO-PVC, respectively) (*Figure 39*).

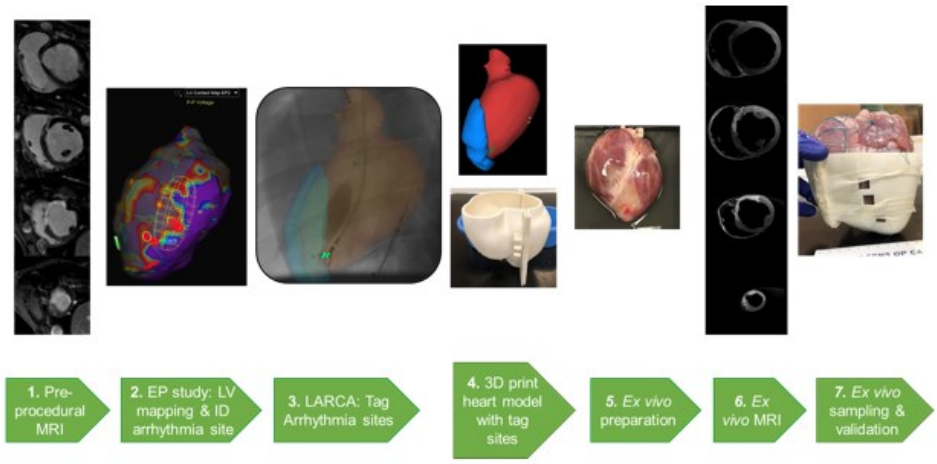

Figure 39. Pipeline of in vivo defined site-directed sampling. 1) A pre-procedural MRI is segmented and models of the LV endocardium, infarct and heart surface are generated. **2)** An electrophysiology mapping study is performed to identify arrhythmia critical regions/sites in the LV. **3)** The regions/sites are tagged on the pre-procedural CMR-derived models using an augmented reality angiography system. **4)** 3D casts of the models with slits for sampling are printed. **5)** The animal is sacrificed and the heart prepared by filling the LV and RV to *in vivo* volumes, and the cast slits are used to mark the arrhythmia critical sites **6)** An *ex vivo* CMR can be performed to have high resolution detail of the myocardium at arrhythmia critical sites. 7) The arrhythmia critical sites are sampled for histology, molecular or functional studies.

The steps of the pipeline are extensively described in the methodological section 3.2.2. This result is not published yet but it led to an interesting collaboration meant to structurally investigate the pathological remodeling occurring around the infarct BZ in massive pig cardiac slices isolated from both PVC and NO-PVC sites, comparing them to remote sites isolated from the healthy distal tissue.

4.3.1 CLARITY-related tissue expansion in myocardial and scar regions

The developed protocol concerning the tissue clearing through the CLARITY methodology and the tissue staining for cellular membranes and sympathetic innervation, together with the SHG detection of collagen by using our custom-made two-photon setup, had shown the capability of providing massive high-resolution reconstructions of the specimens.

However, by applying the CLARITY protocol on mouse hearts, we noticed that the methodology led to a certain degree of tissue swelling that must be taken into account in order to perform reliable structural analyses.
First of all, in order to confine the tissue expansion only to the on-plane section, we developed a custom-made chamber device to perform the clearing and imaging steps (*Figure 40*) which succeeded in preventing anisotropic distortion on the z-axis, ultimately maintaining the planeness of the samples. Moreover, by photographing the samples before and after the clearing protocol on 1-mm graph paper, we were able to estimate the on-plane expansion coefficients in the two dimensions by multiple measurements of the sample length in the X and Y axes. We noticed that, in the slices isolated from the infarct border-zone, the expansion seemed to occur discordantly in the myocardial region with respect to the scar region. Accordingly, we refined our estimation and we calculated the expansion coefficients of both the myocardium and the infarct regions in the two dimensions in each sample. Figure 40 depicts a representative remote and PVC site, where we highlighted the borders of the cleared sample together with its original dimension. In the PVC site we can appreciate the region-specific tissue expansion. The table shows the estimated expansion coefficients in the myocardial and scar regions in each sample in the two dimensions. By calculating these values, we were able to restore our mosaic reconstructions to the original dimension and shape of the samples, in order to perform accurate structural analyses of the tissue features.

A

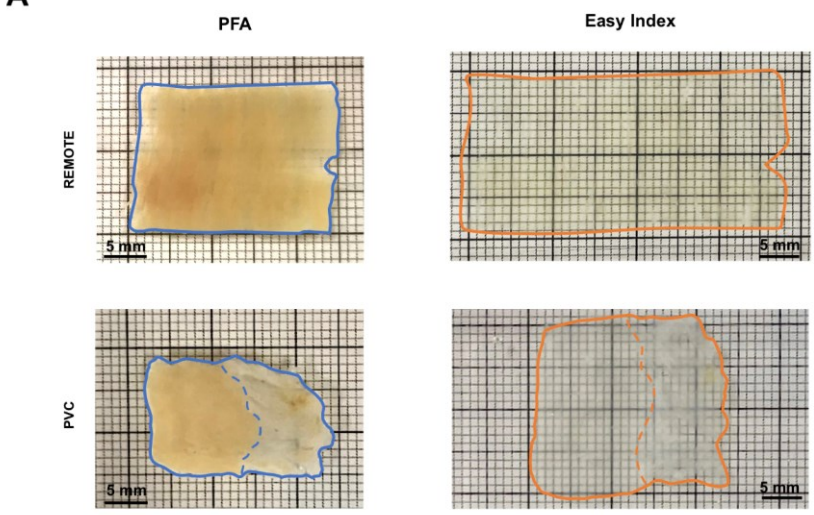

B

Sample	Expansion Factor					
	Myocardium			Collagen		
	X	Y	Area	X	Y	Area
H1 REMOTE	1,561	1,059	1,611	-	-	-
H2 REMOTE	1,587	1,040	1,703	-	-	-
H1 NO-PVC	1,267	1,554	2,395	1,039	1,346	1,679
H2 NO-PVC	1,407	1,587	1,963	1,015	1,113	0,997
H3 NO-PVC	1,682	1,166	2,007	1,138	1,166	1,261
H1 PVC	1,416	1,598	2,073	1,151	1,262	1,611
H2 PVC	1,402	1,287	1,735	1,095	1,084	1,147
H3 PVC	1,341	1,323	1,602	1,173	1,054	1,566
AVG	1,458	1,327	1,886	1,102	1,171	1,377
SD	0,139	0,231	0,274	0,064	0,113	0,280

Figure 40: Estimation of the CLARITY-related expansion coefficients. A) A representative remote and PVC site, both before and after the clearing protocol. The outer borders of the slices have been highlighted in blue (before the clearing) and orange (after the clearing) whereas the dashed line highlights the border between the myocardial and scar regions. **B)** Expansion coefficients of the myocardial and scar regions calculated for each sample in the XY axes and in the surface area. Last rows indicated the average (AVG) and standard deviation (SD) over all samples.

4.3.2 Three-dimensional imaging of the clarified pig heart slices

Figure 41 shows the results of the methodological optimizations and their application on the swine samples. Panel A shows the developed chamber approach, extensively described in the methodological section 3.2.3, used to restrain the freedom of the hydrogel-hybridized molecules to swell anisotropically along the z-axis, thus preventing out-of-plane torsions and deformations of the specimens. On the left, a representative remote sample is shown, both before and after the CLARITY protocol. The slice has achieved an optimal level of transparency and, even though a slight lateral swelling of the tissue is discernible, it is noteworthy that the overall shape and structure of the specimens did not suffer any significant distortion.
Panel B displays the maximum intensity projection (MIP) of 50 μm of two representative 3D reconstructions of a remote and a PVC site (Heart1, H1). The use of a vignetting correction software (CIDRE) for homogenizing the intensity of the signal within the single tiles and the use of a stitching software for the tiles alignment allowed the visualization of mosaic reconstructions of the entire, centimeters-sized pig slices.
As a result of the staining protocol optimizations and the two-photon setup performances, a very high resolution of the images was achieved, thus enabling the detection and identification of single cell membranes and sympathetic neurofilaments (*Figure 41, insets*). Indeed, in the insets the cellular organization (in red) and the sympathetic neuronal network (in green) can be appreciated. The use of the two-photon setup not only provided a higher penetration of the laser beam into the specimen and a higher spatial resolution, but also allowed the label-free detection of the collagen molecules through the SHG signal (in blue) (*see appendix*). The pie charts represent the volumetric percentage of the myocardial tissue (green), scar tissue (dark blue) and of the overlapping region (light blue), over the total volume of the sample, properly corrected for the estimated expansion coefficients.

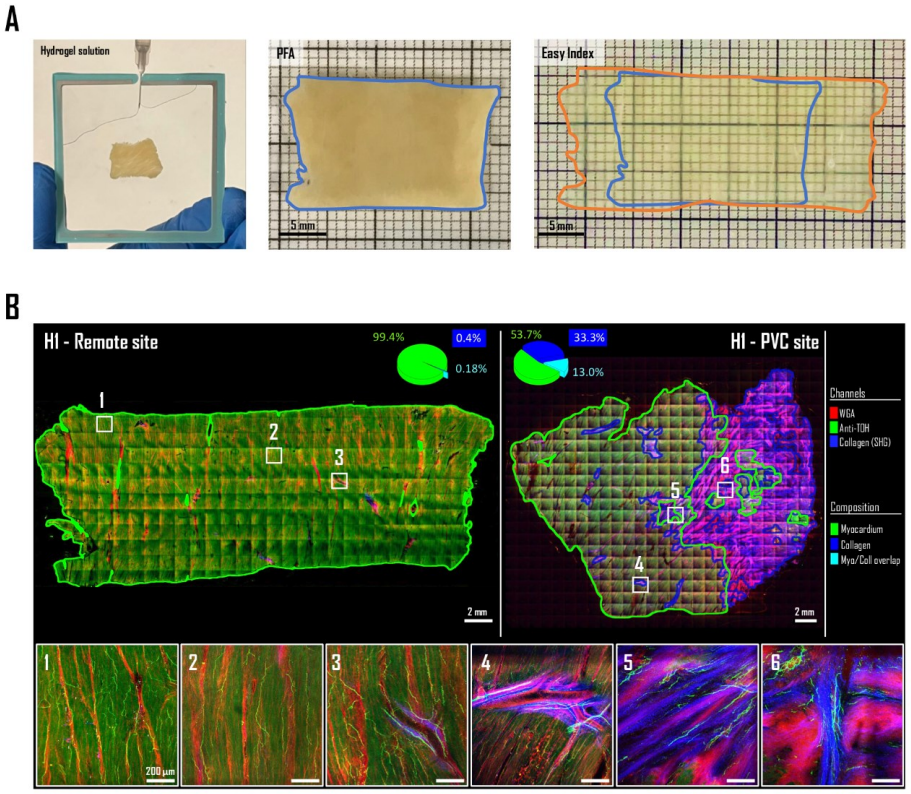

Figure 41: Large-area 3D imaging of CLARITY-cleared pig heart slices. A) On the left, the custom-made chamber developed to prevent anisotropic out-of-plane distortions of the samples during CLARITY-base tissue transformation. On the right, a remote site section before (in PFA) and after the CLARITY (in EasyIndex). Borders, before and after clearing, are highlighted in blue and orange respectively. **B)** Maximum intensity projections (MIPs) of 50 mm of a remote and a PVC site (H1): Wheat-Germ Agglutinin (WGA) in red, Anti-tyrosine Hydroxylase (TOH) in green and collagen (by Second-Harmonic Generation; SHG) in blue. Three representative tiles for each of the two mosaics are shown in the insets below at full resolution. The volumetric percentages of the myocardial, scar and overlap regions are shown in the pie charts respectively in light green, dark blue and light blue.

4.3.3 Quantification of the three-dimensional cellular disarray

After having restored the original dimensions of the samples by exploiting the calculated xy expansion coefficients, we investigated the degree of alignment or misalignment of the cardiomyocytes in the reconstructed slices, since the homogeneous orientation of the cells is crucial for the correct propagation of the AP wavefront.
To examine this tissue feature, we developed and employed a software which allowed us to estimate the 3D orientation of the WGA-labeled cardiomyocytes[127]. The software essentially divided the volume into portions of 70 μm, extracted the principal direction of the cells in each sub-volume and estimated the local disarray through the extracted versors.
We tested three different subvolumes on which estimating the local disarray: 210 μm (3x3x3 subvolumes of 70 μm), 280 μm (4x4x4) and 350 μm (5x5x5). Figure 42A shows the WGA-labeled cardiomyocytes signal of a representative remote site (H1) where the superimposed versors resulting from the analysis follow the main orientation of the cells (insets 1 and 2). The color of the versors represents the "out-of-plane" component (from +90° to -90°) whereas the vector length represents the "in-plane" component (xy plane). The green inset represents the dimensions of the 350 μm (5x5x5) subvolume where the local disarray was estimated, whereas the orange one represents the dimension of the 280 μm (4x4x4) subvolume; finally, the red square represents the subvolume corresponding to the 210 μm (3x3x3) analysis.

Figure 42B shows the resulting color map of the disarray analysis performed on the three experimental classes isolated from H1 (remote, NO-PVC and PVC sites). Here, the degree of cellular disarray is represented colorimetrically, with a white-to-red color bar corresponding to 0-40% of cellular disarray, respectively. Since the WGA also binds the collagen bundles, we exploited the autofluorescence signal of the tissue (coming from the myocardium but not from the fibrotic patches) as a mask to discard the disarray values corresponding to the collagen orientation. In figure 47B, the blue spots correspond to the collagen patches. The regions that were not analyzed, due to a poor contrast or an excessive uniformity of the signal, and the background are instead colored in black.
In panel C the cellular disarray quantification of all the reconstructed slices has been plotted. The colors represent the three different spatial resolutions where the local disarray was estimated (red: 210 μm; orange: 280 μm; green: 350 μm). As expected, the degree of cellular disarray increased by increasing the spatial

resolution in which it was estimated, (350 > 280 >210 μm) in all the samples. Moreover, we found high consistency in the disarray values between the two analyzed remote sites, thus supporting the reliability of the developed analysis tool. However, we did not find any difference in the cellular disarray across the experimental classes, as well as across samples.

Panel D shows the average variation coefficients of the cellular disarray in the three experimental classes, at the three spatial resolutions analyzed.

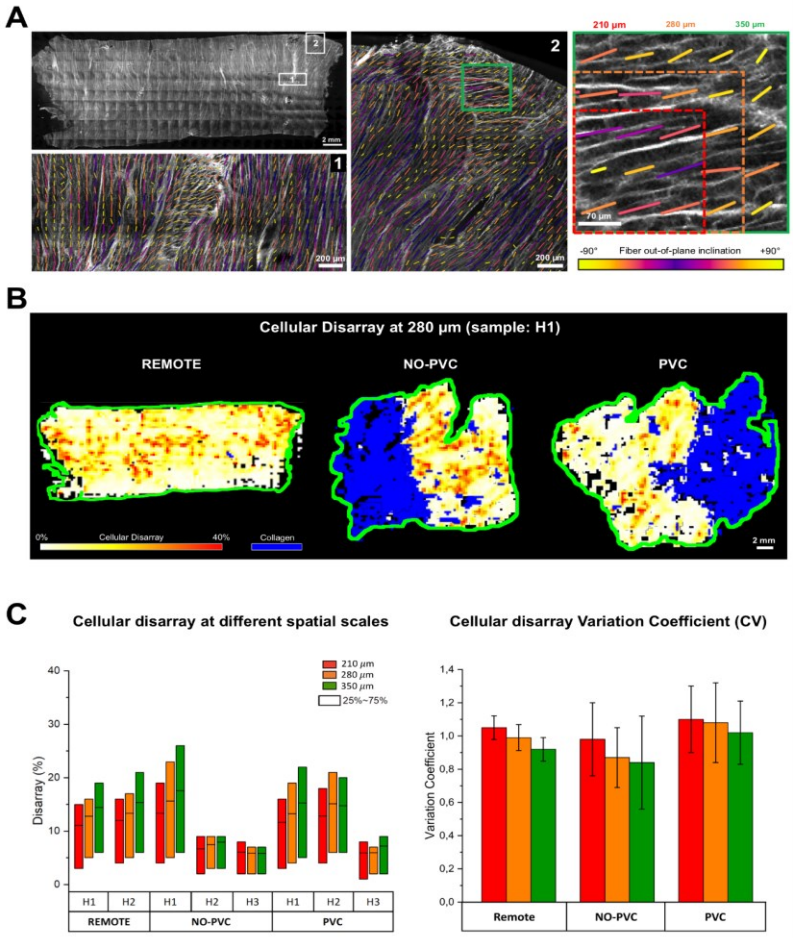

Figure 42: Three-dimensional quantification of cellular disarray. A) Representative result of three-dimensional cellular orientation analysis (colored vectors) superimposed on the WGA signal (in gray-scale) of a remote site (H1). 3D orientation vectors are represented in 2D where "out-of-plane" components (z-axis) are color-coded. On the left, the three different sub-volumes (210, 280 and 350 µm; red, orange and green, respectively) where the cellular disarray was evaluated. **B)** Representative cellular disarray color maps (white-to–red look-up-table; LUT) in the H1 remote, NO-PVC and PVC sites. The scar regions are represented in blue and the slice borders in green. **C)** On the left, the mean cellular disarray values at the three different spatial scales described in panel A. On the right, the average variation coefficients of the two remote sites, three PVC and three NO-PVC sites at the three different spatial scales.

4.3.4 Sympathetic nervous system morphometry

In order to investigate the remodeling occurring to the cardiac SNS in the infarct border-zone, we developed an automatic pipeline to detect neuronal filaments in the high resolution tiles, measure local density and coherency (defined as the degree of local co-alignment) and to reconstruct the 3D maps of these structural parameters of the entire slices.

Figure 43A shows a schematic representation of the developed pipeline. In order to better separate the myocardial and scar regions, we divided the entire volume of the slices in 4 subvolumes of 150 μm each. A maximum intensity projection (MIP) profile was generated for each subvolume, subsequently subjected to the FastRandom Forest tool in order to enhance the neurofilament signal and create probability maps. In those, the intensity value of each pixel corresponds to the probability of it to be a neurofilament, calculated by the machine-learning based software tool manually trained to discriminate between neuronal structures and background. The generated probability maps were exploited to calculate density and coherency values which were then remapped into matrices, where each element spatially correlates to the corresponding tile of the mosaic.

The neuronal density and coherency color maps of the three experimental classes of a representative heart (H1) are displayed in panel B. The tiles that were discarded from the analysis due to high noisy signals, as well as the ones corresponding to the background, are shown in black. To help the visualization, the borders of the myocardial and scar regions were superimposed on the maps in green and blue, respectively.

In the top row, in the remote site neuronal density appears to be consistent within the whole volume of the slice. On the other hand, in the border-zone samples we can appreciate the higher variability of neurofilament density, resulting in a reduced sympathetic innervation in the scar regions with respect to the myocardial regions. Moreover, it can be visually noticed an increased amount of neurofilaments in the region immediately proximal to the scar tissue in both the PVC and NO-PVC sites, even though more pronounced in the NO-PVC site.

In the bottom row, neurofilament alignment coherency appears to be uniform in the entire volume of the remote site; this uniformity is instead reduced in both the border-zone samples, even though no specific trend of local distribution can be perceived.

In panel C, the density values of each tile corresponding to the myocardial and scar regions were discriminated and plotted (in green and blue, respectively). Here, the box highlights the 25-75 percentile of values while the dashed line

represents the average density value of the two remote sites, highlighted as reference.

The density of neurofilaments appears to be consistent between the two remote sites; on the other hand, we found a high variability between the border-zone samples. However, a clear reduction in the density of sympathetic neurofilaments in the scar regions can be noticed across all the samples. By calculating the mean density values of myocardial and scar innervation in each sample, we found a highly significant difference between the two classes ($p= 0.005$), with the scar regions being considerably less innervated than the myocardium ($68\% \pm 15\%$) (panel C, on the right).

Panel D shows the neuronal coherency values estimated in each tile of the mosaics, again discriminating between myocardial and scar regions. The density-weighted mean coherency values are highlighted together with their standard deviation. Again, the dashed line represents the average coherency value of the two remote sites. As we can appreciate, in all the border-zone samples neuronal coherency appears to be decreased compared to this reference value, both in the myocardial and in the scar regions. Moreover, this reduction in the alignment coherency appears to be slightly more pronounced in the PVC sites with respect to the NO-PVC ones.

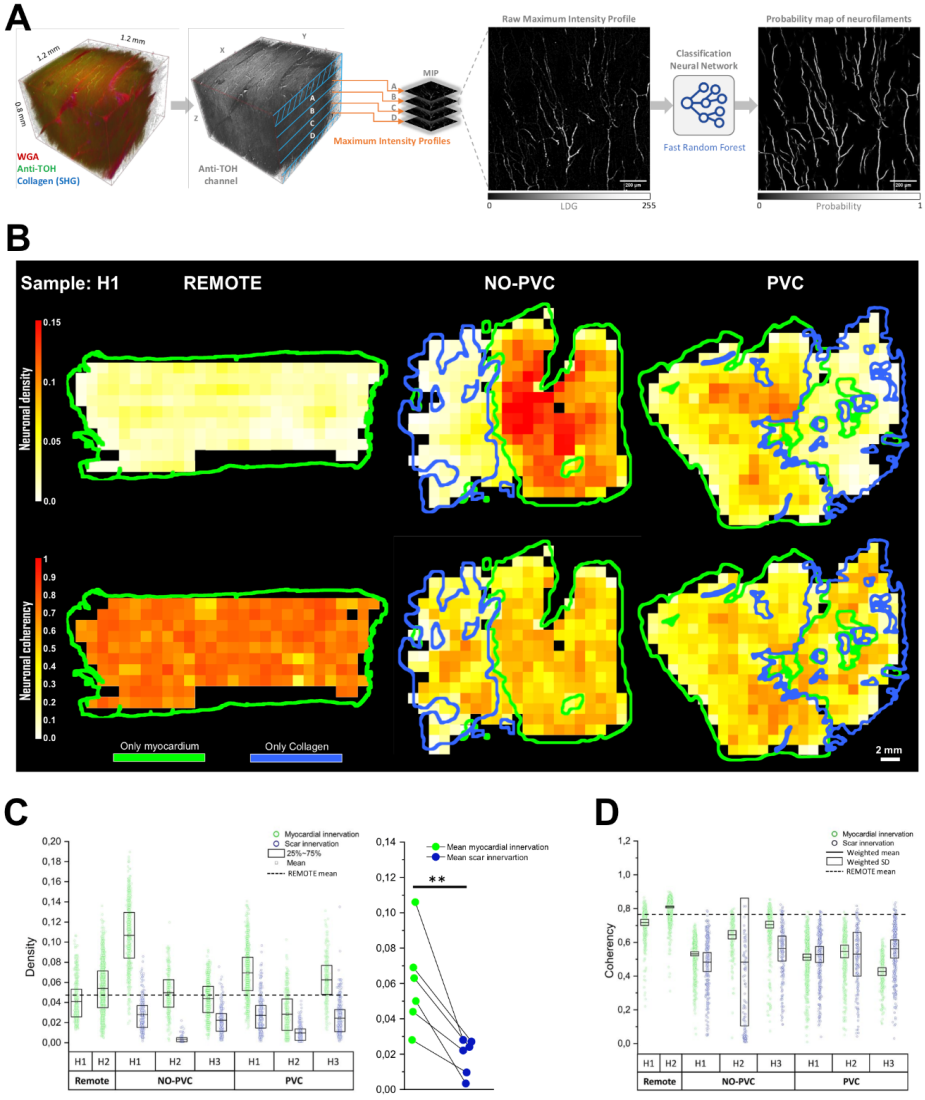

Figure 43: Sympathetic nervous system morphometry. A) Schematic representation of the neurofilament detection pipeline. From the left, a representative 3D reconstruction of a three-colors mosaic tile. For each tile, the anti-TOH detection channel was isolated and the 3D volume was projected in 4 maximum intensity projections (MIPs) profiles. Finally, a FastRandom Forest method was exploited to generate the neurofilament probability map. **B)** Neuronal density and coherency color maps. Myocardium and scar borders have been superimposed, respectively in green and blue. **C)** On the left, density values estimated in each tile of every slice corresponding to the myocardial (in green)

and scar regions (in blue). The dashed line represents the average density value of the two remote sites. On the right, mean density values corresponding to the myocardial and scar regions in NO-PVC and PVC slices. P-value (**$p < 0.01$) were calculated with paired-sample T-test. **D)** Neuronal coherency values estimated in each tile corresponding to the myocardial and scar regions. Average values were estimated by weighting the mean by the local density. The dashed line represents the average coherency value of the two remote sites.

5. CONCLUSIONS AND DISCUSSIONS

The structural remodeling occurring after a myocardial infarction is a leading factor for the development of malignant arrhythmias and sudden cardiac death. Together with the formation of non-conductive fibrotic patches and interstitial fibrosis, several studies have shown that also the remodeling of the SNS can be involved in the susceptibility to experience arrhythmias [90–93]. Among them, premature ventricular complexes (PVCs) have shown to be the most common arrhythmias in patients that have suffered a MI and to be correlated with adrenergic stimulation [82]. Previous studies have indeed identified discrete clusters of PVC sites within the infarct BZ in pigs, from where arrhythmias arise [89].

However, methodological restrictions have prevented the study of the SNS 3D organization in large-size heart samples, both in physiological and in pathological conditions. Thus, the aim of this PhD project was to develop a comprehensive framework for the three-dimensional investigation of the SNS remodeling that occurs in the infarct border-zone after an episode of MI. For the study, we employed a pig model due to its greater similarity to the human heart with respect to small animal models. Moreover, we implemented our structural investigation by performing 3D reconstructions both in arrhythmias initiating and non-initiating sites (PVC and NO-PVC sites, respectively).

We conducted a preliminary investigation in a small population of samples, aimed at pointing out structural differences in the remodeling process that PVC and NO-PVC sites undergo that could explain the susceptibility of PVC sites in triggering arrhythmias and that could be of interest to study in a larger population.

To this goal, first of all we had to face and solve the methodological issues that have limited previous investigations. In order to exploit optical microscopy for obtaining massive 3D reconstructions, we encountered the necessity of optimizing a clearing protocol to reduce the light scattering in large-size heart samples. Indeed, all the protocols that have been developed during the years have always been settled and applied in neuroscience, with the clearing of the brain as a target. However, the heart significantly differs from the cerebral tissue and, thus, the original methodologies are not as efficient in the clearing of the cardiac tissue as they are for the brain. Cerebral tissue has high fat content and relative lack of autofluorescence, unlike the heart tissue[135]. Moreover, the myocardium presents a high concentration of myoglobin that increases significantly tissue coloration and thus optical absorption in the range of visible wavelengths, together with a different texture and the presence of two large cavities. Additionally, it is protein-dense with an extensive network of extracellular connective tissue matrix [136]. For

these reasons, ever since the development of tissue clearing techniques has enabled neuroscientists to successfully image large-size 3D samples, cardiovascular scientists, on the opposite, have struggled in trying to translate these methodologies for imaging the cardiac muscle [135–137].

Even though an ideal methodology for the clearing of the heart is still missing, basing on our experimental necessities we tried to optimize a suitable protocol for the optical clearing and staining of the specimens. In this first step, we employed mouse hearts for their easier availability with respect to pig samples, and a light-sheet microscope to quickly image the entire cleared hearts. We tested one of the most successful organic solvent-based techniques (uDISCO) and two tissue transformation approaches (CLARITY and the most recent SHIELD).

The uDISCO methodology is based on a first step of tissue de-hydration followed by the homogenization of the RI within the tissue by simply incubating the sample in an organic-solvent based solution. It is undoubtedly the quickest and least expensive methodology for the clearing of the heart, but we found that it does not provide a complete transparency of the muscular tissue. Moreover, Lugo-Hernandez *et al*.[138] already stated that the methodology leads to a relevant reduction of the sample volume in the brain but we found that, in addition, in the cardiac tissue it also promotes significant fiber delamination of the muscle, probably due to the first step of tissue dehydration which renders the reconstructions unreliable for structural examinations of the organ. Thus, we did not test any staining protocol on these hearts since the result would anyway have been misleading. Noteworthy, some studies have shown that tissue clearing techniques based on hydrophobic solvents have been successful when applied on embryonic mouse hearts[139,140]. Recently, in 2022, a variation of the DISCO methodology was also successfully employed by Zhu *et al*.[43] in order to image entire adult mouse hearts; the methodology also showed to be compatible with a homogeneous immunostaining of the organs.

Both CLARITY and SHIELD methodologies, on the other hand, are based on tissue transformation protocols that are certainly slower and more complicate, but also more effective in achieving high transparency of the organs. Indeed, instead of simply homogenizing the RI within the specimens, these two methodologies operate by cross-linking the tissue proteins to a scaffolding matrix and by subsequently removing the highly scattering lipid molecules. Together with providing optimal transparency, they also remarkably preserve the organs structure. For these reasons, with the proper presented optimizations, both of

these two methodologies are suitable for the clearing of massive cardiac specimens in order to maintain their structural features.

Thus, we moved forward and we tested the compatibility of these two methodologies with a homogeneous staining of the sample. As a first test, we employed a small lectin that binds cellular membranes (WGA) as a dye. WGA is a plant lectin that is enriched in the seeds of *Triticum* V*ulgaris* and it is specific for terminal *N*-acetylneuraminic acid [141]. These molecules are widely expressed in membranes glycoconjugates [142]; therefore, WGA is able to bind and label cellular membranes. With respect to immunohistochemistry protocols that involve the use of one or two antibodies, with each of them having an average molecular weight of about 150 kDa, the molecular weight of WGA is only 38 kDa, thus facilitating its penetration across the tissue and rendering the staining protocol easier. For these reasons, we found WGA suitable for testing dyes penetration in the specimens subjected to the different clearing protocols.

Despite its very low molecular weight and despite we tested several optimizations of the staining protocol parameters, we did not achieve a sufficient penetration of the dye in SHIELD-cleared hearts, with the WGA remaining confined on the surface of the organ. This phenomenon is probably due to the high compactness of the tissue undergoing the SHIELD preservation protocol, since the polyepoxide matrix that binds the biomolecules is very dense and prevents the diffusion of the dye. On the other hand, staining the hearts before performing the clearing protocol is not useful since the chemicals used for the SHIELD tissue transformation protocol lead to the bleaching of fluorescent proteins.

On the contrary, CLARITY-cleared heart suffer a slight expansion during the clearing protocol, as already reported by Lagerwejic *et al*[143], due to the hybridization of the tissue to the acrylamide-based hydrogel. If, on the one hand, the swelling of the tissue may constitute a problem because it could lead to anisotropic distortions of the sample if not properly prevented, on the other hand this mild expansion facilitates the penetration of the dye within the heart, allowing the homogeneous staining of the entire volume. Thus, we were able to label cellular membranes in the whole CLARITY-cleared organ by using WGA. This first result has high relevance on its own, since it perhaps can lead to study the organization and alignment of cardiomyocytes throughout an entire heart, eventually enabling to compare this feature between control and pathological hearts.

Taking these results together, up to date we may state that the CLARITY procedure is the most comprehensive and conclusive clearing methodology to treat cardiac samples in order to homogenize the RI and obtain 3D reconstructions of fluorescently labeled large-size tissues.

The second step of the methodological procedure optimization was aimed at combining the developed cellular membrane staining, with a uniform labeling of the SNS as well as the collagen fibers in large-size CLARITY-cleared samples. For convenience, we decided to employ isolated mouse ventricles to fasten up the clearing timings, focusing on maintaining the entire thickness of the sample to properly evaluate the penetration of the dyes.

In order to have an increased resolution and greater penetration of the excitation light, we employed the use of a custom-made two-photon fluorescence microscope. Indeed, longer excitation wavelengths used in multi-photon systems enable a deeper penetration of the excitation light in the sample and optical sections are created through confinement of the multi-photon effect to a single focal plane. This method is particularly suitable for imaging large-size tissue samples where penetration depths of 100 μm or more are needed for macro-scale investigations[144]. Moreover, the use of a two-photon microscope allowed the detection of second harmonic generation (SHG) signal[180], thus enabling the label-free collagen detection (*see appendix*).

After several tests, we finally found the parameters required to obtain the best result in terms of labeling uniformity across the whole thickness of the specimens. We selected dyes with the potential to be excited by a common wavelength but exhibiting adequately separated emission spectra, in order to properly differentiate the detection of the three tissue components and prevent their overlapping. The signal to noise ratio between the stained nerves and the background, even if not optimal, was definitely enough to enable the differentiation of the neuronal component after the enhancement of the signal.

At this point, we were confident about the potentialities of the optimized protocol, thus we applied it on the pig slices isolated from remote, PVC and NO-PVC sites of three infarcted hearts to perform our proof-of-concept study.

However, in the previous steps of the project we found out that the CLARITY technique presents some drawbacks, with the most significant one in regard to

our 3D reconstructions being the expansion of the sample that inevitably happens when the hydrogel-hybridized tissue is kept free to swell anisotropically. This could have affected the reliability of the structural information that we obtained from the reconstructions. For this reason, a further optimization of the clearing step was required in order to prevent 3D distortions of the tissue. Due to the flat physiognomy of the slices, we designed a chamber device meant to maintain the planeness of the tissue and to avoid out-of-plane distortions that would have made impossible to reconstruct the original shape of the specimens. The same approach was then used to perform the imaging of the slices, and it succeeded in maintaining their planeness and avoiding Z-axial expansion and out-of-plane distortions. In the past few months, an alternative strategy was presented by Kim and coworkers[118] who faced the same problem when applying the CLARITY methodology on swine samples: they developed a similar approach by utilizing a permeable cotton-mesh pocket to encapsulate the sample during the clearing procedure, thus preventing the swelling of the specimens. We think that both ours and Kim's alternatives are suitable approaches in order to confine the anisotropic swelling of CLARITY-cleared samples and perform reliable structural investigations.

Due to the basic principle of the CLARITY technique, a hydrogel-related swelling was observed nonetheless, but this was confined to an on-plane expansion that we could measure and take into account for further structural analyses. Interestingly, we noticed that this expansion occurred in a region-specific manner in the border-zone samples, with the myocardial portion expanding considerably more than the scar region. We suppose that this phenomenon was related to the higher rigidity and compactness of the scar regions caused by the fibrotic collagen patches, which restrained the capability of the hydrogel matrix to swell. On the other hand, the flexible nature of the muscular tissue probably rendered it more susceptible to the expansion. We therefore carefully estimated the expansion coefficients of both the myocardial and scar regions in each sample which we employed to resize the mosaic reconstructions and to weight all the structural analyses that we performed. With this further improvement, we were confident in considering reliable the structural information that we got from the image analyses.

We obtained mosaic reconstructions of the entire volumes of the slices at high resolution (with a pixel size of 2.34 μm in xy and a Z-step of 5 μm) by acquiring separate tiles subsequently fused together. The high-resolution of the images, together with the reduced signal to noise ratio that we achieved, allowed us to

perform an accurate and high-fidelity image analysis to extrapolate the tissue features of interest.

In order to understand the structural outcomes of the remodeling process, we first of all evaluated the degree of alignment and misalignment of the cells within the tissue. Indeed, many heart disease lead to a remodeling in tissue architecture, including myocardial disarray[145,146]. The correct alignment of cardiomyocytes is fundamental for the action potential to propagate through a homogeneous wavefront across the entire organ; if the cardiomyocytes are not properly organized, with the terminal ends not communicating one with the other, the propagation wavefront of the impulse can result in being distorted, thus potentially leading to arrhythmias. Moreover, myocyte geometrical features are critical in defining the direction of force production[127]. Finding a higher degree of cellular disarray in the three PVC sites could therefore have represented a potential explanation of the arrhythmia-initiating nature of these sites.

To analyze the cellular membrane orientation we developed a software that, through a structure tensor analysis, extracts the main direction of the cells and estimates the local disarray in defined subvolumes (210, 180 and 350 μm). As expected, the degree of cellular disarray increased by increasing the analyzed spatial resolution in all the samples. We found a high consistency in the cellular disarray values between the two remote samples, thus validating the reliability of the approach. However, we did not find any difference in the cellular disarray across the different hearts as well as across the different experimental classes. This result suggests that the orientation of cardiomyocytes does not change dramatically within the infarct border-zone compared to the distal healthy myocardium, as well as between PVC and NO-PVC sites which seem to share the same overall degree of cellular alignment. This finding seems to be in contradiction with previous investigations performed on infarcted mouse hearts[147,148], which have highlight an increase in the fibers disarray in the proximity of the scar region. Due to the demonstrated reliability of the methodology and the consistency among the different spatial volumes tested, we think that this discordance could be due to the sampling nature of the specimens. Moreover, previous studies have been performed by calculating the degree of local alignment and misalignment at the fibers level. The analysis methodology that we propose, on the other hand, performs the disarray estimation at the cellular level. The difference in the volume on which the local disarray is estimated can therefore potentially explain the divergence of results.

We then developed and trained a machine-learning based software tool to detect the neurofilaments and discard the background signal in the full-resolution images. Thanks to the high image quality, the software was able to provide reliable probability maps where the intensity value of each pixel corresponds to the probability of it to be classified as a neurofilament. These maps were then exploited to extrapolate the density and alignment coherency of the nerves in each acquired tile of the mosaics.

The density analysis highlighted a solid consistency between the two remote samples isolated from the distal healthy tissue of the two different hearts, thus confirming the reliability of our analysis approach, while a strong variability between the border-zone samples. Anyway, even with the very small population of samples investigated, by comparing the innervation density of myocardial and scar regions we found a highly significant reduction of neurofilaments in the latter (68 ± 15%), suggesting a strong denervation process that occurs in the wound area during the remodeling. This finding is in line with previous studies performed both in 2D on human heart slices [97] and in 3D in mouse models of myocardial infarction [42,43], which have reported the degeneration and death of sympathetic fibers within the scar. However, previous investigation never discriminated between arrhythmia-initiating and not-initiating sites, due to the impossibility of precisely locating these regions *ex vivo*. Thanks to the developed pipeline, we were able to investigate if the differences in the density of myocardial and scar regions were discordant between PVC and NO-PVC sites, but no evident divergences were found between arrhythmia-initiating and not-initiating sites in this preliminary study.

However, by spatially mapping the neuronal density values of the mosaic tiles, we highlighted spots of increased neurofilament amount in the sites proximal to the scar regions that may suggest the occurrence of a sort of compensatory hyperinnervation effect in the proximity of the denervated wound area. Once again, this feature had already been highlighted in previous studies both in 2D investigations in human slices [106] and in 3D in a MI murine model [104]. We think that our investigation strengthens the reliability of these findings by showing the occurrence of the same neuronal sprouting process in the adjacency of the ischemic border-zone in 3D in a human-resembling animal model.

We found this process to happen in both PVC and NO-PVC sites, even though it seems to be more pronounced in the latter. If this result will be confirmed in further studies, it could provide a possible explanation of the pro-arrhythmic nature of PVC sites compared with NO-PVC sites. Indeed, it could suggest that

the extent of neuronal sprouting in the ischemic border-zone that occurs in NO-PVC sites after a MI could be sufficient to compensate the nerve degeneration and death taking place in the adjacent collagen patches, while deficiently in arrhythmia-initiating sites. Moreover, in the past year Zhu *et al*.[43] also accounted for the dimension of the sympathetic fibers that sprout at the ischemic border-zone in a mouse model of MI, showing a significant increase in small-fiber prevalence, as well as a decrease in medium-fiber prevalence. The evidence of the small-size fibers being the ones which increase in the border-zone in mice is of particular interest, as these are both closest to, and include, the neuroeffector varicosities that interface with myocytes to control cardiac function[44]. We think that, in order to extend our comprehension of the SNS remodeling that follows a MI in human-like animal model, this feature is of special interest for further analyses on our pig model.

A strong consistency between the remote samples was found also in terms of neuronal alignment coherency. Moreover, the analysis suggested an overall reduction of the neuronal coherency in all the border-zone samples with respect to the healthy distal tissue, with no differences between myocardial and scar regions. This reduction seems to be more conspicuous in PVC sites than in NO-PVC ones. However, further studies are required to properly assess whether the degree of sympathetic nerves alignment could really be a factor involved in determining whether arrhythmias will arise or not.

In conclusion, in this PhD project we have presented a comprehensive methodological infrastructure able to three-dimensionally reconstruct large-scale cardiac samples and to provide reliable information regarding the anatomical features of the infarct border-zone. We think that, due to the high relevance of three–dimensional information achieved on a human-resembling animal model, we have provided a clearer and more reliable view of the cardiac sympathetic network remodeling that occurs after an episode of myocardial infarction. We are confident that the presented pipeline can be exploited to further investigate the structural features that may explain the differences between arrhythmia-initiating and non-initiating sites within the infarct border-zone.

Together with expanding the study to a larger cohort of samples, we think that examining other tissue features could be beneficial. In particular, we would like to expand the investigation to analyzing the distribution of connexin-43, which are essential gap-junction proteins involved in the homogeneous propagation of the action potential. An alteration of their expression or allocation in response to an ischemic insult could predispose the heart to a distortion of the action potential

propagation wavefront, thus potentially leading to arrhythmias. In addition, molecular and functional studies are also fundamental to be performed in order to understand if the rising of arrhythmias could rely on defects in the tyramine uptake pathway, in the alteration of the adrenergic receptors or, eventually, in the neurotransmitter release functions. Moreover, recent studies have also shown a developmental transition from production of NE to acetylcholine (ACh) (sympathetic versus parasympathetic trans-differentiation) after a myocardial infarction[149], suggesting that sympathetic co-release of NE and ACh may increase arrhythmia susceptibility; therefore, functionally and structurally investigating this aspect could be highly beneficial in further studies.

In conclusion, we believe that the conceived protocol can be employed to study different cardiac conditions that may rely on structural abnormalities, thus broadening the comprehension of the disease progression.

6. APPENDIX

6.1 Optical clearing and fluorescent staining

All the organs and tissues of our body are composed of different cell types, which are interconnected and cooperate all together to ensure the specific function of each tissue. In the cardiac tissue we can find not only cardiomyocytes, which are arranged in a precise organizational pattern, but also fibroblasts, endothelial cells and neurons. The interplay of the different cell types is what enables the heart to properly contract and maintain a synchronized rhythm.

Therefore, in order to perform reliable and faultless structural analyses of the cardiac tissue, it is fundamental to study the tissue in its three-dimensionality.

However, high-resolution optical imaging in large-scale specimens is extremely difficult to perform, since it is limited by the phenomenon of light scattering, related to the refractive index (RI) mismatch of the biomolecules [45,46], thus limiting the penetration of the light in depth.

To date, histological methodologies have been able to overcome this limitation by mechanically cutting the sample into sections, employing the use of a tool called microtome. Using the microtome, it is feasible to obtain very thin tissue slices, even in the order of 1 micron, to enable their observation under the microscope. However, the mechanical sectioning can harm or distort the tissues, and reconstructing the 3D structure of the sample by lining up and reassembling the images obtained from each slice is a process that necessitates intricate, expensive and time-consuming procedures.

Recently, a number of novel methodologies, called “optical clearing methodologies” have been developed in order to overcome the restrictions imposed both by classical histology and by the inherent nature of biological tissues.

Tissue clearing is the process of changing the optical properties of a tissue to enhance light propagation through it, thus increasing the penetration depth for imaging [150].

The German anatomist Walter Spalteholz wrote the first study on tissue clearing of opaque biological samples in 1911. In order to investigate the circulatory

system in human hearts, he tried to render them transparent by homogenizing the RI among the biomolecules of the sample [151] (*Figure 4*). This way, he was able to observe macroscopic features for the first time in transparent samples by using hydrophobic tissue-clearing agents, such as methyl salicylate and benzyl benzoate, on dehydrated specimens [45].

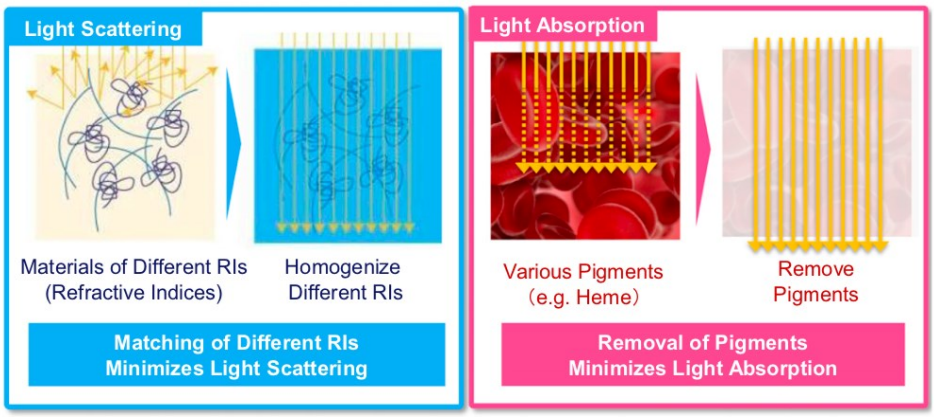

Figure 44: Physical and chemical principles of tissue clearing. Classical physical principles of tissue clearing proposed in 1911 by Spalteholz. While light absorption can be reduced by eliminating pigments, light scattering can be reduced by homogenizing the RIs of the materials [45].

This idea paved the way for the development of several tissue clearing methodologies, in order to obtain optically transparent tissues. Despite this basic idea, designing a tissue clearing project can be difficult and require the optimization of numerous variables. In particular, the aspects that must be taken into account are the need to preserve specific molecules during the processing (like proteins and DNA), maintaining the sample's structural integrity, protecting endogenously expressed fluorescent proteins from structural changes, enhancing porosity to allow for the diffusion of small molecules or immunoglobulin labels, and preserving the structure of pertinent epitopes for the staining [49].

Modern clearing protocols can be classified according to how they homogenize the RI and modify the tissue properties. While all treatments promote transparency to some extent, the degree of transparency and how the protocols affect tissue structure differ, since each protocol is based on the use of a certain

set of chemicals which confers wide-ranging effects on several tissue features, from tissue size to epitope fidelity, to autofluorescence.

- **Organic solvent (hydrophobic) clearing protocols:**

The method that was initially described by Spalteholz [151] involved replacing water with a solution of benzyl benzoate and methyl salicylate, which had a RI of roughly 1.55. Dodt *et al*.[152] revised the methodology by introducing an intermediate dehydration step based on ethanol to remove water molecules from the samples (that present the lowest RI) and exploiting a mixture of benzyl alcohol and benzyl benzoate (BABB, RI= 1.55) to match the RI. The same team looked into alternative dehydration and clearing agents because the original BABB protocol quickly quenches the emission of fluorescent proteins. They discovered that tetrahydrofuran (THF) and dibenzyl ether (DBE) provided the best results for fluorescence preservation and sample transparency (3DISCO) [46,152–154]. In the last years, numerous additional hydrophobic tissue-clearing reagents with various properties have been developed to support a variety of applications, including ultimate DISCO (uDISCO)[155], immunolabeling-enabled DISCO (iDISCO)[53], iDISCO+[156], FluoClearBABB[157], polyethylene glycol (PEG)- associated solvent system (PEGASOS)[158] and stabilized DISCO (sDISCO) [159].

- **Hydrophilic tissue-clearing methods**

The fluorescence of fluorescent proteins is better preserved when the sample is cleared using water-soluble chemicals, which are also less hazardous than methods that employ organic reagents. Tuchin and colleagues were the first to conduct a groundbreaking research on hydrophilic tissue-clearing techniques [160], finding that aqueous solutions of various hydrophilic chemicals had high RI. Chiang and coworkers utilized a different mix of solutions called FocusClear, which contains a detergent (Tween 20) and a X-ray contrast agent (diatrizoate acid) to perform the imaging of a thick sample [161]. Ueda and colleagues developed an efficient hydrophilic tissue-clearing method that they named CUBIC [50] by using a systematic chemical screening strategy. Subsequently, other hydrophilic tissue-clearing reagents have been independently developed: SeeDB [162]; *ClearT,* based on the use of formamide [163]; Sca*l*eS [164]; ClearSee [165]; FRUIT, made of

fructose and urea [166]; urea-based amino-sugar mixture (UBasM)[167]; clearing-enhanced 3D [168]; LUCID [169] and many others.

- **Tissue transformation methods**

The pioneer of this third typology of tissue clearing methodologies is the CLARITY protocol, developed by Chung et al. in 2013 [131]. The main difference with respect to the other two categories is that in tissue transformation protocols some cellular components are removed, while the structural integrity of the sample is maintained by crosslinking the biomolecules to a matrix. Indeed, proteins and nucleic acids are stabilized to a polymerized acrylamide gel thanks to their amine group, while lipids that do not present amine groups are removed during the following incubation in sodium dodecyl sulfate (SDS), a strong detergent. The protocol also allows the visualization of endogenous fluorescent proteins and to label epitopes with fluorescent antibodies. The year after, Raju Tomer and colleagues modified the protocol by reducing the gel density in order to improve tissue permeability and probe penetration (PACT) [170]. Variations of hydrogel-based tissue-clearing reagents have been created for various applications, including optimized CLARITY [171], CLARITY-TDE [121], simplified CLARITY [172] and active clarity technique-pressure related efficient and stable transfer [173]. In order to preserve proteins in the expanded brain, after the development of the CLARITY protocol, Kwanghun Chung and colleagues also developed a protocol to perform magnified analysis of proteome (MAP), a hydrogen-based expansion microscopy method [174]. More recently, the same group introduced the SHIELD methodology [132], in which the acrylamide gel has been replaced by the use of polyepoxy chemicals. With respect to the CLARITY methodology, the SHIELD protocol shows a higher capability of maintaining the structure unaltered and preserving fluorescence, antigenicity, transcripts, and proteins.

With the aid of the methods known as immunofluorescence (IF) and immunohistochemistry (IHC), specific components of a specific tissue or cell type can be seen in optically cleared organs. This broad capability is achieved through combinations of specific antibodies tagged with colored chromogens (IHC), subsequently visualized with a brightfield microscope, or with colored

fluorophores (IF), detected with a fluorescence microscope [175]. As a result, there are many potential uses of IF and IHC in both research and medical treatment.

There are two IF techniques that can be used: the direct (primary) IF or the indirect (secondary) IF. In primary IF, the main antibody that interacts with the target epitope is directly labeled with a fluorophore, while in the indirect technique the target epitope is first bound by a primary antibody, followed by recognition of the primary antibody by a secondary antibody that has been labeled with a fluorophore. The secondary antibody is specific for the host species of the primary one. The direct IF is more rapid and allows the use of multiple antibodies from the same host species; however, the main disadvantage is that the signal can result to be too weak to be properly detected. For this reason, the indirect method is more popular due to its high sensitivity, signal amplification and capacity to detect several targets in the same sample, despite being more time-consuming than the direct IF.

Method	Direct	Indirect	Combined
Advantages	• Rapid single-step staining • Can use multiple antibodies from same host	• Secondary amplifies signal • A few labeled secondaries can detect many primaries	• Amplify signal for weaker targets with secondaries • Stain with multiple primaries from same species
Disadvantages	• No signal amplification from secondary • Each primary must be labeled individually	• Two-step staining • Requires antibodies from different hosts	• Multi-step staining

Figure 45: Schematic representation of direct and indirect IF. The main advantages and disadvantages of the different techniques are summarized in the table [176].

When performing an IF protocol, various factors must be taken into account to be certain of obtaining a selective staining of the specific tissue components. The secondary antibody is directed against the host species of the primary antibody

[177]; consequently, the primary antibody should be produced in a different species than the tissue sample, in order to avoid the secondary antibody reacting with endogenous immunoglobulins in the specimen [175]. Polyclonal primary antibodies, which can bind a variety of epitopes, are typically more sensitive than monoclonal antibodies, which target a single epitope [178].

Multiple secondary antibody modifications and conjugations are possible for the aim of signal amplification and visualization. In order to amplify the signal, polyclonal secondary antibodies can be used [175]. Indeed, multiple epitopes can be recognized by polyclonal secondary antibodies for each primary antibody, increasing binding and signal levels.

The best fluorophore for a certain experiment can be chosen based on a number of variables [179]. First of all, it is necessary to choose fluorophores that can be optimally excited and detected by the available light source, depending on the excitation wavelengths and the detection system of the microscope. Moreover, the ideal fluorophore should have high quantum yields and extinction coefficients, otherwise the signal will result to be dim. Photobleaching can also affect fluorophores, thus rendering the fluorophore no longer excitable; for this reason, it is better to choose photostable fluorophores and decrease both the excitation time and intensity, while choosing antifade mounting chemicals to reduce photobleaching [175].

Additional problems occur when numerous fluorophores are used, due to the possible spectral overlaps, thus requiring a precise examination of the spectra of the selected fluorophores. For a better result, brighter fluorophores should be utilized to detect sparse antigens and dimmer fluorophores should be used to detect abundant antigens when there are differing expression levels of the various components of interest.

Thus, when performing IF staining protocols, in order to obtain optimal and reliable results, several parameters need to be optimized basing on the desired target or targets that have to be analyzed, the species of the specimen, the clearing methodology that has been chosen, the thickness of the sample and the specifics of the microscope that will be used for the imaging.

6.2 Non-linear fluorescence microscopy

Fluorescence microscopy is called linear as it uses a photon to induce the phenomenon of fluorescence in the target molecule, while it is called non-linear when more photons are used for that purpose.

The most common non-linear technique in biology is the Two-Photon Fluorescence Microscopy (TPFM).

The physical principle underlying its functioning is represented in Figure 46.

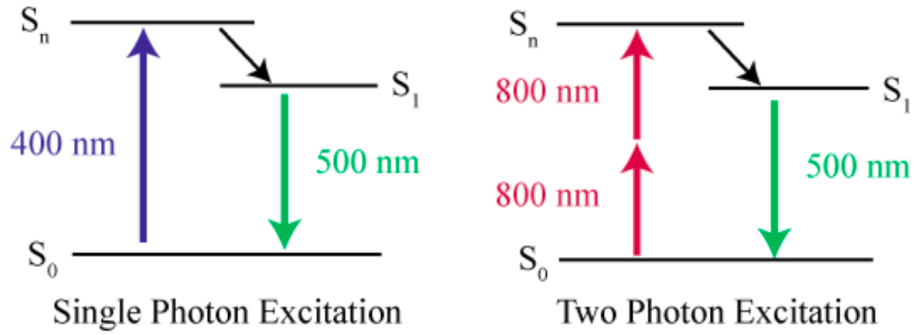

Figure 46: Jablonski energy diagrams for single-photon and two-photon excitation. On the left, a single 400 nm photon is sufficient to cause fluorescence. On the right, two 800 nm photons are required to cause fluorescence. Image from [180].

In a single-photon excitation system, the energy necessary for the fluorophore to move from the ground state S0 to the excited state S1 is absorbed by the photon incident on the fluorescent molecule. In two-photon excitation, on the other hand, this energy is supplied by a pair of lower-energy photons, as long as their interaction with the fluorophore occurs within a quantum of time, that is within a temporal window of the order of 10^{-16} s. This means that, according to the treatment of quantum mechanics, the two events are quantized as a single temporal event. This allows the otherwise physically impossible transition, explained by the creation of an intermediate virtual energy state between S0 and S1: this state is reached thanks to the first photon and from there S1 is reached thanks to the second photon.

From the equation $E= hc/\lambda$ it can be observed that the energy of the photon is inversely proportional to its wavelength. Therefore, two-photon excitation systems allow the use of photons with λ that is double the one used in linear

microscopy systems, that is closer to the infrared. This leads to a first advantage: the reduction of diffusion. Indeed, the cross section of the elastic scattering depends, as a first approximation, in an extremely non-linear manner on the wavelength ($\propto 1 / \lambda^4$); this means that a two-fold increase in the excitation wavelength leads to a 16-fold reduction in the scattering phenomenon.

Moreover, there are further advantages to this technique. In general, if a fluorophore must simultaneously receive n photons to be correctly excited, the excitation probability depends non-linearly on the photon density per cm^2 in the units of time. This implies the need for the flow to have sufficient intensity so that the probability of excitation is different from zero in the target volume. For this purpose, specific lasers are used in TPE which emit very short pulses of radiation (typically radiations of 100 fs with a frequency of 80 - 100 MHz).

The two main consequences deriving from these considerations are:

1. By concentrating the beam on the acquisition volume, the probability will be sufficiently high only in the exact point of interest, while it will decay quickly on different optical sectioning planes. Outside the excitation volume, indeed, the probability will be too low to trigger excitatory phenomena. This involves an almost perfect selection of the excitation volume, which remains constant even in highly scattering tissues, solving the problem of excitation of the tissue areas adjacent to the volume of interest.

2. If the only fluorophores that have sufficient probability of being excited are at the ones of interest, even if the fluorescence signal they emit is affected by scattering, it can still be acquired without signal loss or need for spatial filtering. In fact, all the fluorescence photons emitted by the excited volume, even if deflected, can be acquired by the system because they come from the region of interest of the volume, thus not causing noise in the formation of the image.

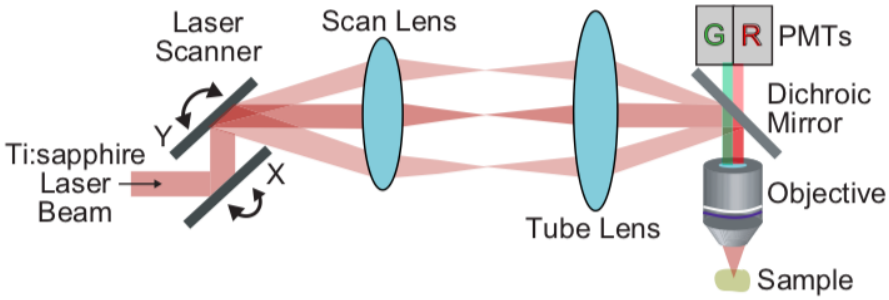

Figure 47: Schematic representation of the typical components in a two-photon microscope. A pair of X/Y scanning mirrors receive an ultra-fast pulsed near-infrared laser beam, which they deflect in two dimensions based on the voltage given to their galvanometric elements. The scan and tube lenses are then used to focus the beam. Two key aspects of scanning microscopy are controlled by the lens combination: the expansion of the beam entering the objective lens, which regulates the size of the beam focus, and the scan angle of the laser beam into the objective, which affects the size of the field of view (FoV). The laser beam is then focused into the objective via a dichroic mirror that passes visible light while reflecting near-infrared light. The objective lens focuses the short laser pulses into a tiny spot at the sample, resulting in multiphoton excitation of fluorescent indicator molecules. The photons are split into two channels (in this image, red and green) and pass via the dichroic mirror before being detected by two specialized photomultiplier tubes (PMTs) [181].

According to the functioning of the two-photon excitation mechanism, a radiation source is needed that must be capable of providing a lot of intensity without damaging the investigated tissue. For this purpose, in the two-photon excitation setup there is a laser (generally a Titanium-Sapphire laser, Ti:Sa LASER) which emits a pulsed light, with frequencies of the order of 106 Hertz and pulses of durations of the order of femto-seconds. Through galvanometric mirrors (GM), the exciting beam (the one emitted by the laser) is catalyzed through the objective lens (Obj) towards the sample mounted on the stage ((Stage xy), which allows displacements in the image plane (xy), so that the excitation beam can reach all the parts of interest. The GM deflects the laser beam with micro-metric precision, allowing it to scan the entire field of view (FoV) of the objective. The Piezoelectric (PIEZO) has the function of moving the objective in z, allowing the selection of different focal planes within the sample.

The light emitted by the sample is collected by the objective and reaches the dichroic mirror (DM). The DM has the purpose of filtering the light signal based on the wavelength: the fluorescence signal emitted by the fluorophores will have a longer wavelength than the excitation signal. The signal is sent to the photomultiplier (PMT) to be acquired and quantized, while all the other components (at a lower wavelength) must be reflected.

The beam arriving at the PMTs is composed of photons coming from the excitation volume. For the generation of the intensity level of each pixel of the image, a certain time (of the order of 5 μs) is required, called dwell time. Within this temporal window, the PMT uses a photocathode which, through the photoelectric effect, allows the generation of electrons from the incoming photons. The relationship between the number of incoming electrons and the number of outgoing photons is called Quantum Efficiency, and depends on the material used.

The released electron is accelerated inside an electric field until it reaches the extraction energy of other electrons. In this process, each electron releases another 5-6 electrons. By repeating this process about 10 times, we obtain the generation of a current consisting of about 105 electrons for each acquired photon. Therefore, for each acquired photon, a peak in the current signal is observed: by counting the peaks in current, it is possible to count the acquired photons. The number of photons acquired is important because it will be proportional to the intensity level assigned to each pixel.

The use of a non-linear microscope also permits the label-free detection of anisotropic molecules (e.g. collagen), through the second harmonic generation (SHG) phenomenon. SHG is a non-linear coherent process that results from the non-linear interaction of electromagnetic waves with matter. It produces secondary electromagnetic waves with a frequency that is twice as high and a wavelength that is twice as short [182] (*Figure 48*). This is a scattering process (no energy is lost) and it is a property exclusively of molecules with no center of symmetry.

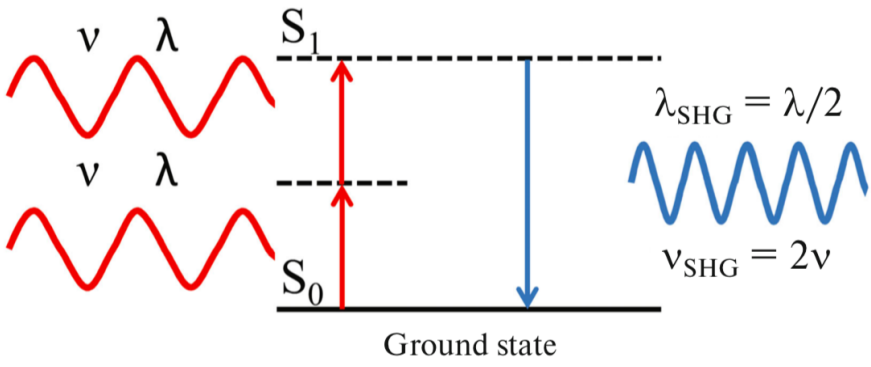

Figure 48: The principle of second harmonic wave generation in non-linear optical medium. ν, incident wave frequency; λ, incident wave wavelength; νSHG, frequency of the formed SHG wave; λSHG, SHG wavelength [182].

Collagen is one of the endogenous anisotropic molecules that we can find in most of the tissues, since it is the most important extracellular structural protein of the animal body [183].

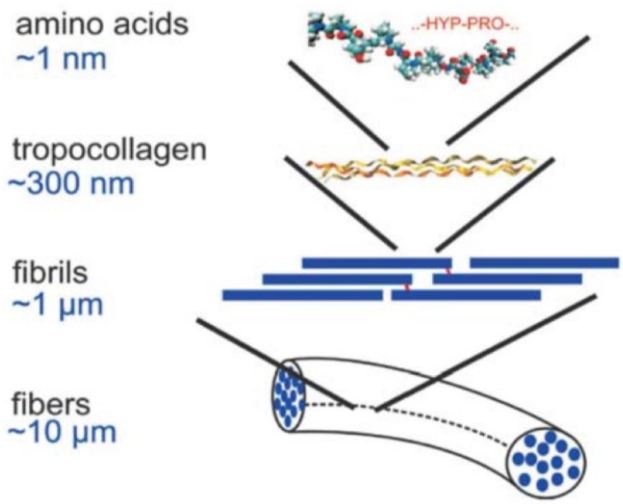

Figure 49: Schematic view of the hierarchical structure of collagen. Representation of the collagen ranging from the amino-acid sequence at a nanoscale level, through the molecular level, up to the scale of collagen fiber bundles with lengths on the order of 10 µm. Modified from [184].

To observe SHG, the electric field of the exciting light must be strong enough to modify the charge distribution in the molecule, which means that very intense light, typically a multi-photon femtosecond pulse laser, is required. When imaging the SHG of fibrillar collagen an excitation of about 800 nm is used, the light path passes through a linear or circular polarizer, and an objective and reaches the specimen [185]. The complete signal is collected using a non-descanned mode; photons travel via a long-wavelength dichroic mirror and the SHG filter (about 400-410 nm). The SHG signals are then collected using high gain photomultiplier tubes in both the forward and reverse orientations.

Non-linear SHG microscopy is a useful method for assessing the condition of collagen in tissues. It is considered an alternative to the traditional diagnostic techniques like histology, histochemistry and immunohistochemistry because it does not require any staining (it is label-free).

7. BIBLIOGRAPHY

1. Prabhu, V., P.G., K., Appathurai, K. & Sucharitha, M. A novel approach for non-invasive measurement of mean arterial pressure using pulse transit time. *Multimed. Tools Appl.* **79**, (2020).

2. Anastasi G., C. S. *Trattao di anatomia umana*. (Edi Ermes).

3. Paul A. Iaizzo. *Handbook of cardiac anatomy, physiology and devices*. (2015).

4. Netter FHBAM. *Atlante di anatomia umana*.

5. Joseph Feher. *Quantitative human physiology*. (2012).

6. Katz AM. *Physiology of the heart*. (2006).

7. https://mdmedicine.wordpress.com/2011/04/24/heart-conduction-system. No Title.

8. Fedele, M. *et al.* A comprehensive and biophysically detailed computational model of the whole human heart electromechanics. **l**, (2022).

9. D'Angelo E., P. A. *Fisiologia*.

10. Silverthorn D.U. *Human physiology: an integrated approach*. (2010).

11. J. Gordon Betts. *Anatomy & Physiology*. (2013).

12. Berridge, M. J., Lipp, P. & Bootman, M. D. the Versatility and Signalling. **1**, (2000).

13. Soeller, C. & Baddeley, D. Super-resolution imaging of EC coupling protein distribution in the heart. *J. Mol. Cell. Cardiol.* **58**, 32–40 (2013).

14. Bers, D. M. Cardiac excitation-contraction coupling. *Nature* **415**, 198–205 (2002).

15. Gregorio, C. C. & Antin, P. B. To the heart of myofibril assembly. *Trends Cell Biol.* **10**, 355–362 (2000).

16. HUXLEY, H. E. The double array of filaments in cross-striated muscle. *J. Biophys. Biochem. Cytol.* **3**, 631–648 (1957).

17. Erenler, T. & Serinagaoglu Dogrusoz, Y. ML and MAP estimation of parameters for the Kalman filter and smoother applied to electrocardiographic imaging. *Med. Biol. Eng. Comput.* **57**, 2093–2113 (2019).

18. A. Despopoulos and S. Silbernagl. *Color atlas of physiology*. (2003).

19. Giudicessi, J. R. & Ackerman, M. J. Determinants of incomplete penetrance and variable expressivity in heritable cardiac arrhythmia syndromes. *Transl. Res.* **161**, 1–14 (2013).

20. Chen, P.-S., Chen, L. S., Fishbein, M. C., Lin, S.-F. & Nattel, S. Role of the autonomic nervous system in atrial fibrillation: pathophysiology and therapy. *Circ. Res.* **114**, 1500–1515 (2014).

21. Jamali, H. K., Waqar, F. & Gerson, M. C. Cardiac autonomic innervation. *J. Nucl. Cardiol.* **24**, 1558–1570 (2017).

22. Armour, J. A. Functional anatomy of intrathoracic neurons innervating the atria and ventricles. *Hear. Rhythm* **7**, 994–996 (2010).

23. Shen, M. J. & Zipes, D. P. Role of the autonomic nervous system in modulating cardiac arrhythmias. *Circ. Res.* **114**, 1004–1021 (2014).

24. Gordan, R., Gwathmey, J. K. & Xie, L.-H. Autonomic and endocrine control of cardiovascular function. *World J. Cardiol.* **7**, 204–214 (2015).

25. Ieda, M. *et al.* Sema3a maintains normal heart rhythm through sympathetic innervation patterning. *Nat. Med.* **13**, 604–612 (2007).

26. Kimura, K., Ieda, M. & Fukuda, K. Development, maturation, and transdifferentiation of cardiac sympathetic nerves. *Circ. Res.* **110**, 325–336 (2012).

27. Kawashima, T. The autonomic nervous system of the human heart with special reference to its origin, course, and peripheral distribution. *Anat. Embryol. (Berl).* **209**, 425–438 (2005).

28. Li, D. & Paterson, D. J. Pre-synaptic sympathetic calcium channels, cyclic nucleotide-coupled phosphodiesterases and cardiac excitability. *Semin. Cell Dev. Biol.* **94**, 20–27 (2019).

29. Opthof, T. *et al.* Dispersion of refractoriness in canine ventricular myocardium: Effects of sympathetic stimulation. *Circ. Res.* **68**, 1204–1215 (1991).

30. Opthof, T. *et al.* Interaction of sympathetic and parasympathetic nervous system on ventricular refractoriness assessed by local fibrillation intervals in the canine heart. *Cardiovasc. Res.* **27**, 753–759 (1993).

31. Li, C. Y. & Li, Y. G. Cardiac Sympathetic Nerve Sprouting and Susceptibility to Ventricular Arrhythmias after Myocardial Infarction. *Cardiol. Res. Pract.* **2015**, (2015).

32. Miller M.R., K. M. Studies on the nerve endings in the heart. *Am. J.*

Anat. **115**, 217–233 (1964).

33. Woollard H.H. The innervation of the heart. *J. Anat.* **60**, 345–373 (1926).

34. Barbosa, P. & Peters, T. M. The effects of vital dyes on living organisms with special reference to Methylene Blue and Neutral Red. *Histochem. J.* **3**, 71–93 (1971).

35. Wainwright, M. The use of dyes in modern biomedicine. *Biotech. Histochem.* **78**, 147–155 (2003).

36. De Biasi, S., Vitellaro-Zuccarello, L. & Blum, I. Histochemical and ultrastructural study on the innervation of human and porcine atrio-ventricular valves. *Anat. Embryol. (Berl).* **169**, 159–165 (1984).

37. Forsgren, S. & Söderberg, L. Immunohistochemical procedures for the demonstration of peptide- and tyrosine hydroxylase-containing nerve fibers in cryostat sections of unfixed rapidly frozen tissue stored for long periods of time - A study on heart tissue. *Histochemistry* **87**, 561–568 (1987).

38. Di Bona, A., Vita, V., Costantini, I. & Zaglia, T. Towards a clearer view of sympathetic innervation of cardiac and skeletal muscles. *Prog. Biophys. Mol. Biol.* **154**, 80–93 (2020).

39. Thaemert J.C. Ultrastructure of cardiac muscle and nerve contiguities. *J. Cell Biol.* **29**, 156–162 (1966).

40. Kimura, K. *et al.* Norepinephrine-induced nerve growth factor depletion causes cardiac sympathetic denervation in severe heart failure. *Auton. Neurosci. Basic Clin.* **156**, 27–35 (2010).

41. Freeman, K., Tao, W., Sun, H., Soonpaa, M. H. & Rubart, M. In situ three-dimensional reconstruction of mouse heart sympathetic innervation by two-photon excitation fluorescence imaging. *J. Neurosci. Methods* **221**, 48–61 (2014).

42. Yokoyama, T. *et al.* Quantification of sympathetic hyperinnervation and denervation aftefile:///C:/Users/redfi/Desktop/UCLA/Research_about_TRPV1/Pathology of SG after MI/Cardiac sympathetic afferent reflex in dogs with congestive heart failure.pdfr myocardial infarction by th. *PLoS One* **12**, 1–13 (2017).

43. Zhu, C. *et al.* High-resolution structure-function mapping of intact hearts reveals altered sympathetic control of infarct border zones. *JCI insight*

7, (2022).

44. Chiba, T. & Yamauchi, A. On the fine structure of the nerve terminals in the human myocardium. *Zeitschrift für Zellforsch. und Mikroskopische Anat.* **108**, 324–338 (1970).

45. Ueda, H. R. *et al.* Whole-Brain Profiling of Cells and Circuits in Mammals by Tissue Clearing and Light-Sheet Microscopy. *Neuron* **106**, 369–387 (2020).

46. Richardson, D. S. & Lichtman, J. W. Clarifying Tissue Clearing. *Cell* **162**, 246–257 (2015).

47. Franceschini, A., Costantini, I., Pavone, F. S. & Silvestri, L. Dissecting Neuronal Activation on a Brain-Wide Scale With Immediate Early Genes. *Front. Neurosci.* **14**, 1–17 (2020).

48. Silvestri, L., Costantini, I., Sacconi, L. & Pavone, F. S. Clearing of fixed tissue: a review from a microscopist's perspective. *J. Biomed. Opt.* **21**, 081205 (2016).

49. Richardson, D. S. *et al.* TISSUE CLEARING. *Nat. Rev. Methods Prim.* **1**, (2021).

50. Susaki, E. A. *et al.* Whole-brain imaging with single-cell resolution using chemical cocktails and computational analysis. *Cell* vol. 157 726–739 (2014).

51. Rajendran, P. S. *et al.* Identification of peripheral neural circuits that regulate heart rate using optogenetic and viral vector strategies. *Nat. Commun.* **10**, 1–13 (2019).

52. Pianca, N. *et al.* Cardiac sympathetic innervation network shapes the myocardium by locally controlling cardiomyocyte size through the cellular proteolytic machinery. *J. Physiol.* **597**, 3639–3656 (2019).

53. Renier, N. *et al.* iDISCO: a simple, rapid method to immunolabel large tissue samples for volume imaging. *Cell* **159**, 896–910 (2014).

54. Sattler, S. M. *et al.* Ventricular Arrhythmias in First Acute Myocardial Infarction: Epidemiology, Mechanisms, and Interventions in Large Animal Models. *Front. Cardiovasc. Med.* **6**, (2019).

55. Thygesen, K., Alpert, J. S. & White, H. D. Universal definition of myocardial infarction. *Circulation* **116**, 2634–2653 (2007).

56. Prabhu, S. D. Post-infarction ventricular remodeling: An array of molecular events. *J. Mol. Cell. Cardiol.* **38**, 547–550 (2005).

57. St. John Sutton, M. G. & Sharpe, N. Left ventricular remodeling after myocardial infarction: Pathophysiology and therapy. *Circulation* **101**, 2981–2988 (2000).

58. Curley, D., Lavin Plaza, B., Shah, A. M. & Botnar, R. M. Molecular imaging of cardiac remodelling after myocardial infarction. *Basic Res. Cardiol.* **113**, 1–18 (2018).

59. Prabhu, S. D. & Frangogiannis, N. G. The Biological Basis for Cardiac Repair After Myocardial Infarction: From Inflammation to Fibrosis. *Circ. Res.* **119**, 91–112 (2016).

60. Frangogiannis, N. G. Regulation of the inflammatory response in cardiac repair. *Circ. Res.* **110**, 159–173 (2012).

61. Nahrendorf, M., Pittet, M. J. & Swirski, F. K. Monocytes: protagonists of infarct inflammation and repair. *Circulation* **121**, 2437–2445 (2011).

62. Talman, V. & Ruskoaho, H. Cardiac fibrosis in myocardial infarction—from repair and remodeling to regeneration. *Cell Tissue Res.* **365**, 563–581 (2016).

63. Kain, V., Prabhu, S. D. & Halade, G. V. Inflammation revisited: inflammation versus resolution of inflammation following myocardial infarction. *Basic Res. Cardiol.* **109**, (2014).

64. Panizzi, P. *et al.* Impaired infarct healing in atherosclerotic ... *J Am Coll Cardiol* **55**, 1629–1638 (2010).

65. Van Den Borne, S. W. M. *et al.* Myocardial remodeling after infarction: The role of myofibroblasts. *Nat. Rev. Cardiol.* **7**, 30–37 (2010).

66. Shinde, A. V & Frangogiannis, N. G. Fibroblasts in myocardial infarction: a role in inflammation and repair. *J. Mol. Cell. Cardiol.* **70**, 74–82 (2014).

67. Stuart, S. D. F., Jesus, N. M. De, Lindsey, M. L. & Crystal, M. Following Myocardial Infarction. 114–122 (2017) doi:10.1016/j.yjmcc.2015.12.024.The.

68. Carmeliet, E. Cardiac ionic currents and acute ischemia: From channels to arrhythmias. *Physiol. Rev.* **79**, 917–1017 (1999).

69. Koester, C., Ibrahim, A. M., Cancel, M. & Labedi, M. R. The Ubiquitous Premature Ventricular Complex. *Cureus* **12**, 1–10 (2020).

70. Al-Khatib, S. M. *et al.* 2017 AHA/ACC/HRS Guideline for Management of Patients With Ventricular Arrhythmias and the Prevention of Sudden

Cardiac Death: Executive Summary: A Report of the American College of Cardiology/American Heart Association Task Force on Clinical Practice Gu. *Circulation* **138**, e210–e271 (2018).

71. Cherry, E. M., Fenton, F. H. & Gilmour, R. F. Mechanisms of ventricular arrhythmias: A dynamical systems-based perspective. *American Journal of Physiology - Heart and Circulatory Physiology* vol. 302 (2012).

72. Li, W., Ripplinger, C. M., Lou, Q. & Efimov, I. R. Multiple monophasic shocks improve electrotherapy of ventricular tachycardia in a rabbit model of chronic infarction. *Hear. Rhythm* **6**, 1020–1027 (2009).

73. Hall, G. E., Stewart, C. B. & Manning, G. W. The Electrocardiographic Records of 2,000 R.C.A.F. Aircrew. *Can. Med. Assoc. J.* **46**, 226–230 (1942).

74. Clarke, J. M., Hamer, J., Shelton, J. R., Taylor, S. & Venning, G. R. The rhythm of the normal human heart. *Lancet (London, England)* **1**, 508–512 (1976).

75. Hoogendijk, M. G., Géczy, T., Yap, S. C. & Szili-Torok, T. Pathophysiological Mechanisms of Premature Ventricular Complexes. *Front. Physiol.* **11**, 1–8 (2020).

76. Niwano, S. *et al.* Prognostic significance of frequent premature ventricular contractions originating from the ventricular outflow tract in patients with normal left ventricular function. *Heart* **95**, 1230–1237 (2009).

77. Baman, T. S. *et al.* Relationship between burden of premature ventricular complexes and left ventricular function. *Hear. Rhythm* **7**, 865–869 (2010).

78. Akdemir, B., Yarmohammadi, H., Chadi Alraies, M. & Adkisson, W. O. Premature ventricular contractions: Reassure or refer? *Cleveland Clinic Journal of Medicine* vol. 83 (2016).

79. Bonow R., Mann D., T. G. *Braunwald's Heart Disease: A textbook of cardiovascular medicine.* (2018).

80. Lin, C.-Y. *et al.* Long-term outcome of multiform premature ventricular complexes in structurally normal heart. *Int. J. Cardiol.* **180**, 80–85 (2015).

81. Saeed, M., Wendland, M. F., Watzinger, N., Akbari, H. & Higgins, C. B. MR contrast media for myocardial viability, microvascular integrity and

perfusion. *Eur. J. Radiol.* **34**, 179–195 (2000).

82. Dries, E. *et al.* Altered adrenergic response in myocytes bordering a chronic myocardial infarction underlies in vivo triggered activity and repolarization instability. *J. Physiol.* **598**, 2875–2895 (2020).

83. Doytchinova, A. *et al.* Subcutaneous nerve activity and spontaneous ventricular arrhythmias in ambulatory dogs. *Hear. Rhythm* **12**, 612–620 (2015).

84. Belevych, A. E. *et al.* Shortened Ca2+ signaling refractoriness underlies cellular arrhythmogenesis in a postinfarction model of sudden cardiac death. *Circ. Res.* **110**, 569–577 (2012).

85. Hegyi, B. *et al.* Complex electrophysiological remodeling in postinfarction ischemic heart failure. *Proc. Natl. Acad. Sci. U. S. A.* **115**, E3036–E3044 (2018).

86. Priori, S. G., Mantica, M. & Schwartz, P. J. Delayed afterdepolarizations elicited in vivo by left stellate ganglion stimulation. *Circulation* **78**, 178–185 (1988).

87. Marrouche, N. F. *et al.* Mode of initiation and ablation of ventricular fibrillation storms in patients with ischemic cardiomyopathy. *J. Am. Coll. Cardiol.* **43**, 1715–1720 (2004).

88. Bogun, F. *et al.* Relationship of frequent postinfarction premature ventricular complexes to the reentry circuit of scar-related ventricular tachycardia. *Hear. Rhythm* **5**, 367–374 (2008).

89. Amoni, M. *et al.* Discrete sites of frequent premature ventricular complexes cluster within the infarct border zone and coincide with high frequency of delayed afterdepolarizations under adrenergic stimulation. *Hear. Rhythm* **18**, 1976–1987 (2021).

90. Nademanee, K., Taylor, R., Bailey, W. E., Rieders, D. E. & Kosar, E. M. Treating Electrical Storm. *Circulation* **102**, 742–747 (2000).

91. Basu, S. *et al.* Beneficial effects of intravenous and oral carvedilol treatment in acute myocardial infarction. A placebo-controlled, randomized trial. *Circulation* **96**, 183–191 (1997).

92. Billman, G. E., Castillo, L. C., Hensley, J., Hohl, C. M. & Altschuld, R. A. Beta2-adrenergic receptor antagonists protect against ventricular fibrillation: in vivo and in vitro evidence for enhanced sensitivity to beta2-adrenergic stimulation in animals susceptible to sudden death. *Circulation* **96**, 1914–1922 (1997).

93. Exner, D. V. *et al.* Beta-blocker use and survival in patients with ventricular fibrillation or symptomatic ventricular tachycardia: The antiarrhythmics versus implantable defibrillators (AVID) trial. *J. Am. Coll. Cardiol.* **34**, 325–333 (1999).

94. Lorentz, C. U. *et al.* Heterogeneous ventricular sympathetic innervation, altered beta-adrenergic receptor expression, and rhythm instability in mice lacking the p75 neurotrophin receptor. *Am. J. Physiol. Heart Circ. Physiol.* **298**, H1652-60 (2010).

95. Gardner, R. T. *et al.* Targeting protein tyrosine phosphatase σ after myocardial infarction restores cardiac sympathetic innervation and prevents arrhythmias. *Nat. Commun.* **6**, 1–9 (2015).

96. Barber, M. J., Mueller, T. M., Henry, D. P., Felten, S. Y. & Zipes, D. P. Transmural myocardial infarction in the dog produces sympathectomy in noninfarcted myocardium. *Circulation* **67**, 787–796 (1983).

97. Zipes, D. P. Influence of myocardial ischemia and infarction on autonomic innervation of heart. *Circulation* **82**, 1095–1105 (1990).

98. Boogers, M. J. *et al.* Cardiac Sympathetic Denervation Assessed With 123-Iodine Metaiodobenzylguanidine Imaging Predicts Ventricular Arrhythmias in Implantable Cardioverter-Defibrillator Patients. *J. Am. Coll. Cardiol.* **55**, 2769–2777 (2010).

99. Nishisato, K. *et al.* Impaired cardiac sympathetic innervation and myocardial perfusion are related to lethal arrhythmia: Quantification of cardiac tracers in patients with ICDs. *J. Nucl. Med.* **51**, 1241–1249 (2010).

100. Fallavollita. Regional myocardial sympthe. **63**, 141–149 (2014).

101. Sepe, J. J. *et al.* Therapeutics That Promote Sympathetic Reinnervation Modulate the Inflammatory Response After Myocardial Infarction. *JACC. Basic to Transl. Sci.* **7**, 915–930 (2022).

102. Inoue, H. & Zipes, D. P. Results of sympathetic denervation in the canine heart: Supersensitivity that may be arrhythmogenic. *Circulation* **75**, 877–887 (1987).

103. Dae, M. W. *et al.* Scintigraphic assessment of sympathetic innervation after transmural versus nontransmural myocardial infarction. *J. Am. Coll. Cardiol.* **17**, 1416–1423 (1991).

104. Li, W., Knowlton, D., Van Winkle, D. M. & Habecker, B. A. Infarction alters both the distribution and noradrenergic properties of cardiac

sympathetic neurons. *Am. J. Physiol. Heart Circ. Physiol.* **286**, H2229-36 (2004).

105. Vracko, R., Thorning, D. & Frederickson, R. G. Fate of nerve fibers in necrotic, healing, and healed rat myocardium. *Lab. Invest.* **63**, 490–501 (1990).

106. Vracko, R., Thorning, D. & Frederickson, R. G. Nerve fibers in human myocardial scars. *Hum. Pathol.* **22**, 138–146 (1991).

107. Cao, J. M. *et al.* Relationship between regional cardiac hyperinnervation and ventricular arrhythmia. *Circulation* **101**, 1960–1969 (2000).

108. Cao, J. M. *et al.* Nerve sprouting and sudden cardiac death. *Circ. Res.* **86**, 816–821 (2000).

109. Rubart, M. & Zipes, D. P. Mechanisms of sudden cardiac death. *J. Clin. Invest.* **115**, 2305–2315 (2005).

110. Zhou, S. *et al.* Mechanisms of cardiac nerve sprouting after myocardial infarction in dogs. *Circ. Res.* **95**, 76–83 (2004).

111. Hasan, W. *et al.* Synthesis Following Myocardial Infarction in Rats. **1124**, 142–154 (2007).

112. Oh, Y. S. *et al.* Spatial distribution of nerve sprouting after myocardial infarction in mice. *Hear. Rhythm* **3**, 728–736 (2006).

113. Yokoyama, T. *et al.* Quantification of sympathetic hyperinnervation and denervation after myocardial infarction by three-dimensional assessment of the cardiac sympathetic network in cleared transparent murine hearts. *PLoS One* **12**, 1–13 (2017).

114. El-Helou, V. *et al.* Dexamethasone treatment of post-MI rats attenuates sympathetic innervation of the infarct region. *J. Appl. Physiol.* **104**, 150–156 (2008).

115. Ajijola, O. A. *et al.* Focal myocardial infarction induces global remodeling of cardiac sympathetic innervation: Neural remodeling in a spatial context. *Am. J. Physiol. - Hear. Circ. Physiol.* **305**, 1031–1040 (2013).

116. Cao, J. *et al.* and Ventricular Arrhythmia. 1960–1969 (2000).

117. Vaseghi, M., Lux, R. L., Mahajan, A. & Shivkumar, K. Sympathetic stimulation increases dispersion of repolarization in humans with myocardial infarction. *Am. J. Physiol. - Hear. Circ. Physiol.* **302**, 1838–1846 (2012).

118. Kim, J. J. H. *et al.* Pocket CLARITY enables distortion-mitigated cardiac microstructural tissue characterization of large-scale specimens. *Front. Cardiovasc. Med.* **9**, 1–11 (2022).

119. Crick, S. J., Sheppard, M. N., Ho, S. Y., Gebstein, L. & Anderson, R. H. Anatomy of the pig heart: Comparisons with normal human cardiac structure. *J. Anat.* **193**, 105–119 (1998).

120. Olianti, C. *et al.* Optical clearing in cardiac imaging: A comparative study. *Prog. Biophys. Mol. Biol.* **168**, 10–17 (2022).

121. Costantini, I. *et al.* A versatile clearing agent for multi-modal brain imaging. *Sci. Rep.* **5**, (2015).

122. De Buck, S. *et al.* An augmented reality system for patient-specific guidance of cardiac catheter ablation procedures. *IEEE Trans. Med. Imaging* **24**, 1512–1524 (2005).

123. Giardini, F. *et al.* Mesoscopic Optical Imaging of Whole Mouse Heart. *J. Vis. Exp.* (2021) doi:10.3791/62795.

124. Voigt, F. F., Kirschenbaum, D., Platonova, E. & Pagès, S. Europe PMC Funders Group The mesoSPIM initiative – open-source light-sheet microscopes for imaging cleared tissue. **16**, 1105–1108 (2020).

125. Smith, K. *et al.* CIDRE: An illumination-correction method for optical microscopy. *Nat. Methods* **12**, 404–406 (2015).

126. Schindelin, J. *et al.* Fiji: an open-source platform for biological-image analysis. *Nat. Methods* **9**, 676–682 (2012).

127. Giardini, F. *et al.* Quantification of Myocyte Disarray in Human Cardiac Tissue. *Front. Physiol.* **12**, 1–14 (2021).

128. Di Bona, A., Vita, V., Costantini, I. & Zaglia, T. Towards a clearer view of sympathetic innervation of cardiac and skeletal muscles. *Prog. Biophys. Mol. Biol.* **154**, 80–93 (2020).

129. Pianca, N. *et al.* Cardiac sympathetic innervation network shapes the myocardium by locally controlling cardiomyocyte size through the cellular proteolytic machinery. *J. Physiol.* **597**, 3639–3656 (2019).

130. Olianti, C. *et al.* 3D imaging and morphometry of the heart capillary system in spontaneously hypertensive rats and normotensive controls. *Sci. Rep.* **10**, 1–9 (2020).

131. Chung, K. *et al.* Structural and molecular interrogation of intact biological systems. *Nature* **497**, 332–337 (2013).

132. Park, Y. G. *et al.* Protection of tissue physicochemical properties using polyfunctional crosslinkers. *Nat. Biotechnol.* **37**, 73 (2019).

133. Erturk, A., Pan, C., Cai, R., Quacquarelli, F. & Gasemigharagoz, A. Whole organ and organism tissue clearing by uDISCO. *Protoc. Exch.* (2016) doi:10.1038/protex.2016.055.

134. Susaki, E. A. *et al.* Versatile whole-organ/body staining and imaging based on electrolyte-gel properties of biological tissues. *Nat. Commun.* **11**, (2020).

135. Kolesová, H., Olejníčková, V., Kvasilová, A., Gregorovičová, M. & Sedmera, D. Tissue clearing and imaging methods for cardiovascular development. *iScience* **24**, 102387 (2021).

136. Sands, G. B. *et al.* It's clearly the heart! Optical transparency, cardiac tissue imaging, and computer modelling. *Prog. Biophys. Mol. Biol.* **168**, 18–32 (2022).

137. Kolesová, H., Čapek, M., Radochová, B., Janáček, J. & Sedmera, D. Comparison of different tissue clearing methods and 3D imaging techniques for visualization of GFP-expressing mouse embryos and embryonic hearts. *Histochem. Cell Biol.* **146**, 141–152 (2016).

138. Lugo-Hernandez, E. *et al.* 3D visualization and quantification of microvessels in the whole ischemic mouse brain using solvent-based clearing and light sheet microscopy. *J. Cereb. blood flow Metab. Off. J. Int. Soc. Cereb. Blood Flow Metab.* **37**, 3355–3367 (2017).

139. Miller, C. E. *et al.* Confocal imaging of the embryonic heart: how deep? *Microsc. Microanal. Off. J. Microsc. Soc. Am. Microbeam Anal. Soc. Microsc. Soc. Canada* **11**, 216–223 (2005).

140. Belle, M. *et al.* Tridimensional Visualization and Analysis of Early Human Development. *Cell* **169**, 161-173.e12 (2017).

141. Schwefel, D. *et al.* Structural basis of multivalent binding to wheat germ agglutinin. *J. Am. Chem. Soc.* **132**, 8704–8719 (2010).

142. MONSIGNY, M., ROCHE, A. -C, SENE, C., MAGET-DANA, R. & DELMOTTE, F. Sugar-Lectin Interactions: How Does Wheat-Germ Agglutinin Bind Sialoglycoconjugates? *Eur. J. Biochem.* **104**, 147–153 (1980).

143. Lagerweij, T. *et al.* Optical clearing and fluorescence deep-tissue imaging for 3D quantitative analysis of the brain tumor microenvironment. *Angiogenesis* **20**, 533–546 (2017).

144. Hickey, S. M. *et al.* Fluorescence microscopy—an outline of hardware, biological handling, and fluorophore considerations. *Cells* **11**, (2022).

145. Spinale, F. G. & Zile, M. R. Integrating the myocardial matrix into heart failure recognition and management. *Circ. Res.* **113**, 725–738 (2013).

146. Ariga, R. *et al.* Identification of Myocardial Disarray in Patients With Hypertrophic Cardiomyopathy and Ventricular Arrhythmias. *J. Am. Coll. Cardiol.* **73**, 2493–2502 (2019).

147. Strijkers, G. J. *et al.* Diffusion tensor imaging of left ventricular remodeling in response to myocardial infarction in the mouse. *NMR Biomed.* **22**, 182–190 (2009).

148. Chen, J. *et al.* Remodeling of cardiac fiber structure after infarction in rats quantified with diffusion tensor MRI. *Am. J. Physiol. Heart Circ. Physiol.* **285**, H946-54 (2003).

149. Olivas, A. *et al.* Myocardial Infarction Causes Transient Cholinergic Transdifferentiation of Cardiac Sympathetic Nerves via gp130. *J. Neurosci. Off. J. Soc. Neurosci.* **36**, 479–488 (2016).

150. Weiss, K. R., Voigt, F. F., Shepherd, D. P. & Huisken, J. Tutorial: practical considerations for tissue clearing and imaging. *Nature Protocols* vol. 16 2732–2748 (2021).

151. Hahn, S. [Not Available]. *NTM* **7**, 105–117 (1999).

152. Dodt, H. U. *et al.* Ultramicroscopy: Three-dimensional visualization of neuronal networks in the whole mouse brain. *Nat. Methods* **4**, 331–336 (2007).

153. Becker, K., Jährling, N., Saghafi, S., Weiler, R. & Dodt, H. U. Chemical clearing and dehydration of GFP expressing mouse brains. *PLoS One* **7**, 1–6 (2012).

154. Ertürk, A. *et al.* Three-dimensional imaging of solvent-cleared organs using 3DISCO. *Nature Protocols* vol. 7 1983–1995 (2012).

155. Pan, C. *et al.* Shrinkage-mediated imaging of entire organs and organisms using uDISCO. *Nature Methods* vol. 13 859–867 (2016).

156. Liebmann, T. *et al.* Three-Dimensional Study of Alzheimer's Disease Hallmarks Using the iDISCO Clearing Method. *Cell Rep.* **16**, 1138–1152 (2016).

157. Schwarz, M. K. *et al.* Fluorescent-protein stabilization and high-resolution imaging of cleared, intact mouse brains. *PLoS One* **10**, 1–26

(2015).

158. Jing, D. *et al.* Tissue clearing of both hard and soft tissue organs with the pegasos method. *Cell Res.* **28**, 803–818 (2018).

159. Hahn, C. *et al.* High-resolution imaging of fluorescent whole mouse brains using stabilised organic media (sDISCO). *J. Biophotonics* **12**, 1–10 (2019).

160. Tuchin, V. V, Wang, R. K. & Yeh, A. T. Optical clearing of tissues and cells. *Journal of biomedical optics* vol. 13 21101 (2008).

161. Liu, Y.-C. & Chiang, A.-S. High-resolution confocal imaging and three-dimensional rendering. *Methods* **30**, 86–93 (2003).

162. Ke, M. T., Fujimoto, S. & Imai, T. SeeDB: A simple and morphology-preserving optical clearing agent for neuronal circuit reconstruction. *Nat. Neurosci.* **16**, 1154–1161 (2013).

163. Kuwajima, T. *et al.* ClearT: A detergent- and solvent-free clearing method for neuronal and non-neuronal tissue. *Development (Cambridge)* vol. 140 1364–1368 (2013).

164. Hama, H. *et al.* ScaleS: An optical clearing palette for biological imaging. *Nat. Neurosci.* **18**, 1518–1529 (2015).

165. Kurihara, D., Mizuta, Y., Sato, Y. & Higashiyama, T. ClearSee: A rapid optical clearing reagent for whole-plant fluorescence imaging. *Development (Cambridge)* vol. 142 4168–4179 (2015).

166. Hou, B. *et al.* Scalable and DiI-compatible optical clearance of the mammalian brain. *Front. Neuroanat.* **9**, 1–11 (2015).

167. Chen, L. *et al.* UbasM: An effective balanced optical clearing method for intact biomedical imaging. *Sci. Rep.* **7**, 1–11 (2017).

168. Li, W., Germain, R. N. & Gerner, M. Y. Multiplex, quantitative cellular analysis in large tissue volumes with clearing-enhanced 3D microscopy (Ce3D). *Proc. Natl. Acad. Sci. U. S. A.* **114**, E7321–E7330 (2017).

169. Mizutani, H. *et al.* Transparency-enhancing technology allows three-dimensional assessment of gastrointestinal mucosa: A porcine model. *Pathol. Int.* **68**, 102–108 (2018).

170. Tomer, R., Ye, L., Hsueh, B. & Deisseroth, K. Advanced CLARITY for rapid and high-resolution imaging of intact tissues. *Nat. Protoc.* **9**, 1682–1697 (2014).

171. Lee, H., Park, J. H., Seo, I., Park, S. H. & Kim, S. Improved application of the electrophoretic tissue clearing technology, CLARITY, to intact solid organs including brain, pancreas, liver, kidney, lung, and intestine. *BMC Dev. Biol.* **14**, 1–7 (2014).

172. Lai, H. M. *et al.* Rationalisation and validation of an acrylamide-free procedure in three-dimensional histological imaging. *PLoS One* **11**, 1–14 (2016).

173. Li, Y., Xu, J., Wan, P., Yu, T. & Zhu, D. Optimization of GFP Fluorescence Preservation by a Modified uDISCO Clearing Protocol. *Front. Neuroanat.* **12**, 1–10 (2018).

174. Ku, T. *et al.* Multiplexed and scalable super-resolution imaging of three-dimensional protein localization in size-adjustable tissues. *Nat. Biotechnol.* **34**, 973–981 (2016).

175. Im, K., Mareninov, S., Diaz, M. F. P. & Yong, W. H. An Introduction to Performing Immunofluorescence Staining. *Methods Mol. Biol.* **1897**, 299–311 (2019).

176. Biotium. https://biotium.com/tech-tips/tech-tip-combined-direct-and-indirect-immunofluorescence-using-primary-antibodies-from-the-same-host/.

177. Carpenter B. Secondary antibody selection guide. http://www.abcam.com/secondary-antibodies/secondary-antibody-selection-guide.

178. Taylor CR, Shi SR, B. N. *Techniques of immunohistochemistry: principles, pitfalls and standardization*. (2010).

179. Brelje, T. C., Wessendorf, M. W. & Sorenson, R. L. Multicolor laser scanning confocal immunofluorescence microscopy: practical application and limitations. *Methods Cell Biol.* **38**, 97–181 (1993).

180. Paul Margaretha, K. S. *Fotochimica*.

181. Lecoq, J., Orlova, N. & Grewe, B. F. Wide. Fast. Deep: Recent Advances in Multiphoton Microscopy of In Vivo Neuronal Activity. *J. Neurosci. Off. J. Soc. Neurosci.* **39**, 9042–9052 (2019).

182. Dudenkova, V. V. *et al.* Examination of Collagen Structure and State by the Second Harmonic Generation Microscopy. *Biochem.* **84**, 89–107 (2019).

183. Cox, G. Biological applications of second harmonic imaging. *Biophys. Rev.* **3**, 131–141 (2011).

184. Cicchi, R. *et al.* From molecular structure to tissue architecture: Collagen organization probed by SHG microscopy. *J. Biophotonics* **6**, 129–142 (2013).

185. Mostaço-Guidolin, L., Rosin, N. L. & Hackett, T. L. Imaging collagen in scar tissue: Developments in second harmonic generation microscopy for biomedical applications. *Int. J. Mol. Sci.* **18**, (2017).

AKNOWLEDGEMENTS

Firstly, I would like to express my deepest gratitude to my supervisors, Dr. Leonardo Sacconi and Prof. Elisabetta Cerbai, for always guiding and advising me throughout my PhD, as well as for their availability and expertise, without which the final outcome and completion of this work would have not been possible.

I would also like to thank Prof. Karin Sipido and Prof. Piet Claus for the very stimulating collaboration that led to this interesting project. Again, a special thank from the bottom of my heart goes to Matthew, that significantly contributed to the design and execution of the project. I wish he could be here to see the great results that came out of the project, I am sure he would be very happy of what we achieved.

Moreover, I would like to thank Prof. Peter Kohl for hosting me at the Institute for Experimental Cardiovascular Medicine during my PhD period abroad, where I spent an incredible experience that really helped me in improving my work skills.